

Computational Fluid Dynamics and 3D Printing towards Nanoscale Thickness Gradients and Scale-up of a Spatial Atomic Layer Deposition System

by

Jhi Yong Loke

A thesis
presented to the University of Waterloo
in fulfillment of the
thesis requirement for the degree of
Master of Applied Science
in
Mechanical and Mechatronics Engineering

Waterloo, Ontario, Canada, 2020

© Jhi Yong Loke 2020

Author's Declaration

This thesis consists of material all of which I authored or co-authored: see Statement of Contributions included in the thesis. This is a true copy of the thesis, including any required final revisions, as accepted by my examiners.

I understand that my thesis may be made electronically available to the public.

Statement of Contributions

Sections 2.1, 3.1 and 3.2 of Chapter 3 of this thesis consist of portions of a manuscript written for publication, which was co-authored by myself, my supervisor, Abdullah H. Alshehri, Viet Huong Nguyen, Alexander Jones, Hatameh Asgarimoghaddam, Ahmed Shahin, Khaled H. Ibrahim, Kissan Mistry, Professor Mustafa Yavus and Professor David Muñoz-Rojas. I performed the Computational Fluid Dynamics (CFD) simulation work, designed and 3D printed the customized reactor head, deposited thickness gradient zinc oxide films and drafted the customized reactor sections in the manuscript. Kissan Mistry helped perform reflectance spectroscopy characterization of the zinc oxide film thickness. This research was conducted under the supervision of Professor Kevin Musselman and Professor Mustafa Yavus at the University of Waterloo, and Professor David Muñoz-Rojas at Grenoble INP.

Section 2.2 of Chapter 4 of this thesis consists of detailed design of a heated substrate stage design for a pilot-scale Atmospheric Pressure Spatial Atomic Layer Deposition (AP-SALD) system that is part of an international patent application, (United States Provisional Patent Application No. 62/949,798), for which the co-inventors include myself, my supervisor, Chee Hau Teoh and Manfred Kao. All co-inventors contributed equally to the invention of the pilot-scale spatial atomic layer deposition and chemical vapor deposition system for thin film deposition in atmospheric condition. The patent was filed by Jeffrey Wong, a patent attorney, with the support from University of Waterloo Commercialization Office (WatCo) and Gary Brock, the director of strategic initiatives at WatCo.

Abstract

Nanoscale functional thin films are integral part of all modern devices. As these devices continue to miniaturize in feature size, better control of film thickness and quality is needed. Atomic Layer Deposition (ALD) is becoming the best option for such devices as it produces high quality ultrathin films that are pinhole-free and conformal by growing the film one atomic layer at a time. However, it remains a slow, expensive and challenging to scale process due to its vacuum chamber requirement. Furthermore, its disadvantages make it inefficient for device prototyping and optimization. Atmospheric Pressure Spatial ALD (AP-SALD) is a novel technique that produces ultrathin films with quality identical to conventional ALD, but at a speed up to 100x faster in open-air without the need of a vacuum chamber, and is scalable to high throughput manufacturing such as roll-to-roll processes.

In this work, a customized lab-scale AP-SALD reactor that can deposit thin films with thickness gradients for high throughput combinatorial synthesis and studies is designed, 3D printed and tested. The design of the reactor is guided by Computational Fluid Dynamics (CFD) and design guidelines of Stereolithography (SLA) 3D printing. The reactor was designed with a multimodal feature whereby it can be used to deposit either uniformly thick or graded thin films. It was tested to deposit a uniformly thick zinc oxide film that is 178 nm thick on borosilicate glass with a uniformity of $\pm 5\%$, growth per cycle (GPC) of 1.19 nm/cycle and growth rate of 0.66 nm/s. The same reactor was also used to deposit a zinc oxide film with a thickness gradient of 70 nm (from 150 to 80 nm) with GPC of 0.30 nm/cycle (0.33 nm/s) on the thicker side and GPC of 0.17 nm/cycle (0.19 nm/s) on the thinner side.

To validate the scalability of the AP-SALD technique, a heated translating stage that can hold multiple industrial-size substrates (9x larger than lab-scale substrates in area) all at once for high throughput deposition, and a unique reactor for large-area deposition were design and constructed for a pilot-scale AP-SALD system. The heated stage is designed to

heat the substrates from room temperature to 300 °C, which is within the ALD window of some common technologically relevant materials such as zinc oxide and aluminum oxide for initial testing. The unique reactor was 3D printed and tested to produce zinc oxide and aluminum oxide films on industrial-size borosilicate glass with thicknesses of 63 nm (uniformity $\pm 7\%$) and 108 nm (uniformity $\pm 6\%$) respectively.

Acknowledgements

Foremost, I would like to express my most profound gratitude to Dr. Kevin Musselman for his continuous support throughout my study and research. He has always been supportive, patient and approachable attending to all the questions and concerns I have. His understanding has given me the freedom to express myself through the work I produce, while making sure that I do not go off track with my ideas. His encouragement never ceases to motivate me to produce with the best of my abilities. Working with Dr. Kevin Musselman has been one of the greatest experiences I have had.

To the best colleagues I can ever ask for, Chee Hau and Manfred Kao (both of which are past MASC students of Dr. Kevin Musselman), I will always be grateful. I worked closely with Chee Hau on the mechanical design and construction of the pilot-scale Atmospheric Pressure Spatial Atomic Layer Deposition system. Manfred has been more than helpful to us, going above and beyond time after time to help with electrical design, programming, and system design of the very sophisticated system. I enjoy the time we had challenging each other the past 2 years.

I would like to thank Richard Forgett and Mark Kuntz, manager and lead hand respectively at the University's Engineering Machine Shop, for attending to the countless needs I had and providing me with great life and engineering advice. Their expertise with anything mechanical were critical in the development of the system. I would also like to thank Phil Laycock, Fred Bakker, Rob Kraemer, and Jorge Cruz, technicians at the University's Engineering Machine Shop for their assistance with fabricating all the mechanical parts which made the project possible.

I would like to thank Neil Griffett, the electronics technician, of the Mechanical and Mechatronics Engineering Department at the University of Waterloo. His expertise and

assistance with all things related to electronics were unparalleled. He is efficient and always willing to help with the requests I had, no matter how big or small. I would also like to thank James Merli and Andy Barber, electronic technologists of the Mechanical and Mechatronics Engineering Department at the University of Waterloo, for making sure the system meets the safety requirement and for offering the insights on electrical standards and practices from their many years of experience.

A very special thanks to my best friends and house mates to whom I owe everything - Chee and Candice for making sure I am keeping my sanity, always cooking and baking the best foods, brewing and mixing fun concoctions to try, challenging me through tough conversations, pushing me beyond the potential I see in myself, dragging me to yoga, workouts and the outside for runs, bringing me to see and explore new places, watching TV together, and always being there creating the fondest memories for ourselves. None of this would be possible without their constant support, patience and care.

Last but not least, I must thank my friends, and family for their unconditional love and support throughout my academic journey. I would not be in the position I am today if it weren't for them.

Table of Contents

Author's Declaration	ii
Statement of Contributions	iii
Abstract	iv
Acknowledgements	vi
List of Figures	xi
List of Tables	xvi
1 Introduction	1
1.1 Atomic Layer Deposition and its Applications	2
1.2 Atmospheric Pressure Spatial Atomic Layer Deposition (AP-SALD)	5
1.3 Thickness gradient films and applications	12
1.4 Thesis overview	14
2 Literature Review	15

2.1	Previous methods for making thickness gradient films	16
2.2	Previous CFD modelling of AP-SALD reactors	18
2.3	Previous 3D printing of AP-SALD reactors	23
2.4	Design of AP-SALD systems	26
3	Gradient AP-SALD reactors	30
3.1	Chapter overview	31
3.2	Experimental Design	34
3.3	Results and Discussion	57
3.4	Conclusion	65
4	Heated stage and 3D printed reactor for pilot-scale AP-SALD	66
4.1	Chapter overview	67
4.2	Experimental Design	68
4.3	Results and Discussion	86
4.4	Conclusion	90
5	Conclusion and Future works	91
	References	94
	APPENDICES	100

A	Thickness gradient film with a lab-scale AP-SALD reactor	101
A.1	Film mapping code	102
B	Scale-up of a heated substrate stage for pilot-scale AP-SALD system	103
B.1	Heating Power Budgeting Tool	104
B.2	Iterative Solver	109

List of Figures

1.1	A representation of one ALD cycle showing two self-limiting surface reactions	3
1.2	A diagram showing the difference between ALD and AP-SALD. (a) In ALD, different precursor gases are exposed one at a time. (b) In SALD, different precursor gases are exposed simultaneously but separated in space.	5
1.3	Schematic illustrations of spatial atomic layer deposition techniques based on (a) circulating flexible substrates, (b) rotating substrate cylinders, and (c) linear “zone-separated” precursor regions. All approaches spatially isolate precursor gases A and B from one another. Adapted with permission from [1]. Copyright 2016 American Chemical Society.	6
1.4	A photo of Dr. Kevin Musselman’s lab-scale AP-SALD at the University of Waterloo. Obtained with permission from Chee Hau Teoh.	10
1.5	A schematic of Dr. Kevin Musselman’s lab-scale AP-SALD at the University of Waterloo. Adapted with permission from Chee Hau Teoh.	10
1.6	Photo of the pilot-scale AP-SALD system in Dr. Kevin Musselman’s lab at the University of Waterloo. Obtained with permission from Chee Hau Teoh.	11
1.7	A representation of the concept of film with thickness gradient	13

2.1	Example of a mesh for CFD analysis	19
2.2	Most common element types for CFD mesh definition	20
2.3	SALD floating substrate concept	22
2.4	SALD round reactor concept	27
2.5	SALD for roll-to-roll process	29
3.1	Concept of tilted reactor for depositing films with thickness gradient where d1 exhibits a larger gap spacing than d2. Obtained with permission from Abdullah Alshehri	31
3.2	Concept of customized reactor for depositing films with thickness gradient .	32
3.3	Structured mesh of the uniform channel	35
3.4	Difference in flow estimation between triangular and square cells	35
3.5	CFD analysis of the reactor channel with (a) 0.25 mm width, and (b) 0.75 mm width	36
3.6	CFD analysis of the proposed 0.75 mm to determine height to achieve fully development	37
3.7	Comparison of flow profile at outlet between 0.75 mm and 1.4 mm channels (30 mm channel height)	37
3.8	Optimized channel geometry for graded flow rates at outlet	38
3.9	Flow velocity contour inside and at the outlet of the gradient channel	39

3.10	Turbulent inner layers of a flow	40
3.11	First layer height requirement of (a) high-Re and (b) low-Re turbulence models	40
3.12	Structured mesh of the gradient channel with y^+ value of 1	41
3.13	Flow velocity contour inside and at the outlet of the gradient channel, simulated (a) with the SST turbulence model and (b) without any turbulence model	42
3.14	Vertical velocity profile at the outlet of the gradient channel based on (a) SST and (b) no turbulence model simulations	43
3.15	Velocity contour of the flow outwards from the gradient channel with a substrate placed 100 μm under	44
3.16	Plot of velocity components on different locations across the substrate surface	45
3.17	Example of a part being printed (a) at an angle and (b) flat	48
3.18	Support structures of an identical part being printed (a) at an angle and (b) flat	49
3.19	A sectioned print layer of the rectangular part oriented at an angle	50
3.20	Example of a gradient film mapped using the film mapping code	55
3.21	Film mapping rig	56
3.22	A 3D printed reactor installed into Dr. Musselman's lab-scale AP-SALD system	58
3.23	Internal network of gas distribution channels in the customized reactor design	60

3.24	Custom reactor design	61
3.25	Preparation of customized reactor design using Formlabs' PreForm slicer software and photo of the 3D printed reactor	62
3.26	Uniform film produced via the printed reactor using the uniform channel	63
3.27	Gradient film produced via the printed reactor using the gradient channel	64
4.1	ALD window	68
4.2	Cross section of the substrate stage design	72
4.3	Photo of the physical substrate stage installed into the pilot-scale AP-SALD system. Adapted with permission from Chee Hau Teoh.	72
4.4	Heating element design for the top assembly	73
4.5	Photo of the physical heating element being fitted into the top assembly	73
4.6	Heating modes of the top assembly during idle	76
4.7	Thermal simulation of the top assembly	78
4.8	Simulated buckling due to thermal effects of the top assembly	79
4.9	suction chuck concept to hold substrates	80
4.10	Free body diagram of the substrate during stage acceleration or deceleration	80
4.11	Motion profile of the stage	81
4.12	Design of the pilot-scale reactor and photo of the 3D printed reactor	85

4.13	Zinc oxide film produced using the 3D printed pilot-scale reactor	88
4.14	Aluminum oxide film produced using the 3D printed pilot-scale reactor . . .	89
A.1	Film mapping code using the Delaunay triangulation method of interpolation	102
B.1	Sheet 1: Geometry definition of the stage top assembly	104
B.2	Sheet 2: Material Properties of the stage top assembly	105
B.3	Sheet 3: Interpolator to determine the thermophysical properties at a user defined temperature based on established data set [2]	105
B.4	Sheet 4: Iterative solver to estimate the side temperatures of the stage . . .	106
B.5	Sheet 5a: Calculation of the total heat loss from the stage top assembly to bottom assembly and environment during idle	106
B.6	Sheet 5b: Continuation of Sheet 5a	107
B.7	Sheet 6: Calculation of the total heat loss from the stage top assembly when it is oscillating	107
B.8	Sheet 7: Calculation of the total heating power needed to heat stage to and maintain at user defined temperature during idle and operation	108
B.9	Cross sections of the top assembly sides as well as heating element and side temperatures	109

List of Tables

2.1 Existing methods that can produce thickness gradient films	17
--	----

Chapter 1

Introduction

1.1 Atomic Layer Deposition and its Applications

Nanoscale functional thin films are integral part of all modern devices. As these devices continue to miniaturize in feature size, better control of film thickness and quality is needed. Conventional thin film manufacturing techniques that are widely used in the industry, for instance Chemical Vapor Deposition (CVD) and Physical Vapor Deposition (PVD) are slowly becoming inadequate to meet those requirements. Currently, Atomic Layer Deposition (ALD) is one of the best techniques to satisfy those demands because it can create high quality ultra-thin film with atomic-level control.

Unlike conventional methods that normally create films by directly depositing the compound onto a substrate, ALD films are produced typically through binary self-limiting surface half-reactions, sequentially creating one monolayer at a time [3]. Since there is a finite number of surface sites available for the half-surface reaction to occur, the films produced are often superior in quality such that they are highly uniform, pin-hole free and conformal. These characteristics of ALD provides excellent step-coverage capability that is needed to make next-generation devices.

ALD has been used to create various types of films such as oxides, nitrides, sulfides, elemental and other compounds [4]. Commonly, ALD is used to produce metal oxide films which usually involves a metal source and an oxygen source that are vaporized from their respective precursors. The deposition is usually carried out in a vacuum chamber where the substrate is placed and heated for the surface reaction to occur. The ALD process consists of four steps: 1) precursor exposure, 2) evacuation or purging of the precursors and byproducts from the chamber, 3) exposure of the reactant species, such as oxidants or reagents, and 4) evacuation or purging of the reactants and byproduct from the chamber. The four-step process which correspond to one ALD cycle [5] is shown in Figure 1.1. The

cycle is repeated until a desired thickness is achieved.

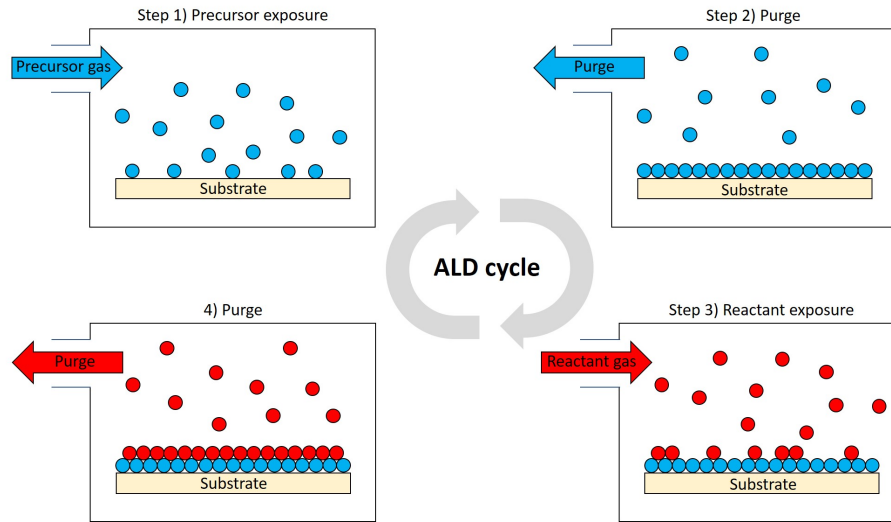


Figure 1.1 A representation of one ALD cycle showing two self-limiting surface reactions

Because of the superior film quality and excellent thickness control, ALD has been proven to be an important and necessary tool for many applications. One such application of ALD can be found in the deposition of high-k dielectrics such as HfO_2 which was used to replace the thermally-grown SiO_2 as the gate material in metal oxide semiconductor field effect transistors, or MOSFETs, found in the vast majority of integrated circuits [6]. ALD can also be used to add a protective coating directly on Lithium ion battery cathodes which drastically improves the battery capacity and charge-discharge cycles [7]. A fine balance in terms of coating thickness is required since too thick of a coating would negatively affect the electrode properties, while too thin would not provide sufficient protection. Apart from cathode coating, ALD is currently one of the few techniques that can be used for the research and development of 3D all-solid-state batteries. These batteries consist of 3D structures such as deep trenches that require excellent step coverage, uniformity, conformality and thickness control. Moreover, the films must have the highest quality because a single pinhole will short-circuit the battery, making it useless [8]. ALD has also been found useful particularly for creating the thin film encapsulation layers that protect air and moisture

sensitive devices such as organic light emitting diode displays and perovskite solar cells from degradation [9, 10], improving their stability and reliability. Furthermore, ALD is also found in medical applications, for example it is capable of improving implantable sensors and water purification membranes by modifying the pores of nanoporous alumina used [11].

Despite the numerous advantages of ALD, it has its own set of drawbacks. The major weakness with ALD is that it is a slow process and it needs a vacuum chamber, limiting its throughput and scalability respectively. While one can argue that larger chambers can be used for scaling, it still remains a slow batch process. This is not necessarily an issue for some industries that process the Si in batches of wafers, such as photovoltaics and integrated circuits. However ALD is not compatible with other high throughput applications which often require roll-to-roll manufacturing.

1.2 Atmospheric Pressure Spatial Atomic Layer Deposition (AP-SALD)

In conventional ALD, the two precursor gases are introduced into a vacuum chamber with purge steps in between to remove the by-products and excess precursor gas. A monolayer of film is formed after each ALD cycle, and the cycle is repeated until a film with desired thickness is achieved. Hence, conventional ALD separates the precursors in time by alternating the precursor exposure and purging cycles [1]. Instead, spatial atomic layer deposition (SALD) separates the two precursors in space by moving substrate back and forth between the two precursor gases, which are supplied constantly, to replicate the sequential exposure cycles. This approach eliminates the purge steps that make conventional ALD slow. Figure 1.2 shows the difference between ALD and SALD.

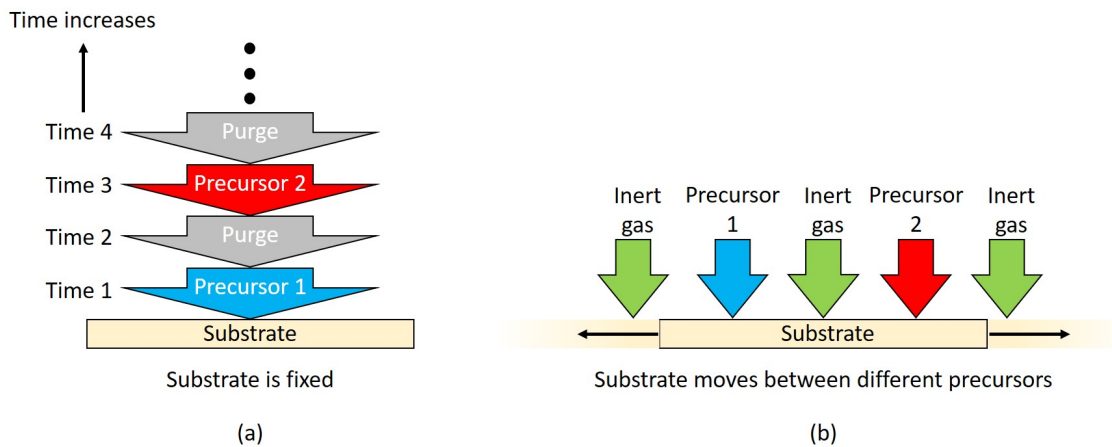


Figure 1.2 A diagram showing the difference between ALD and AP-SALD. (a) In ALD, different precursor gases are exposed one at a time. (b) In SALD, different precursor gases are exposed simultaneously but separated in space.

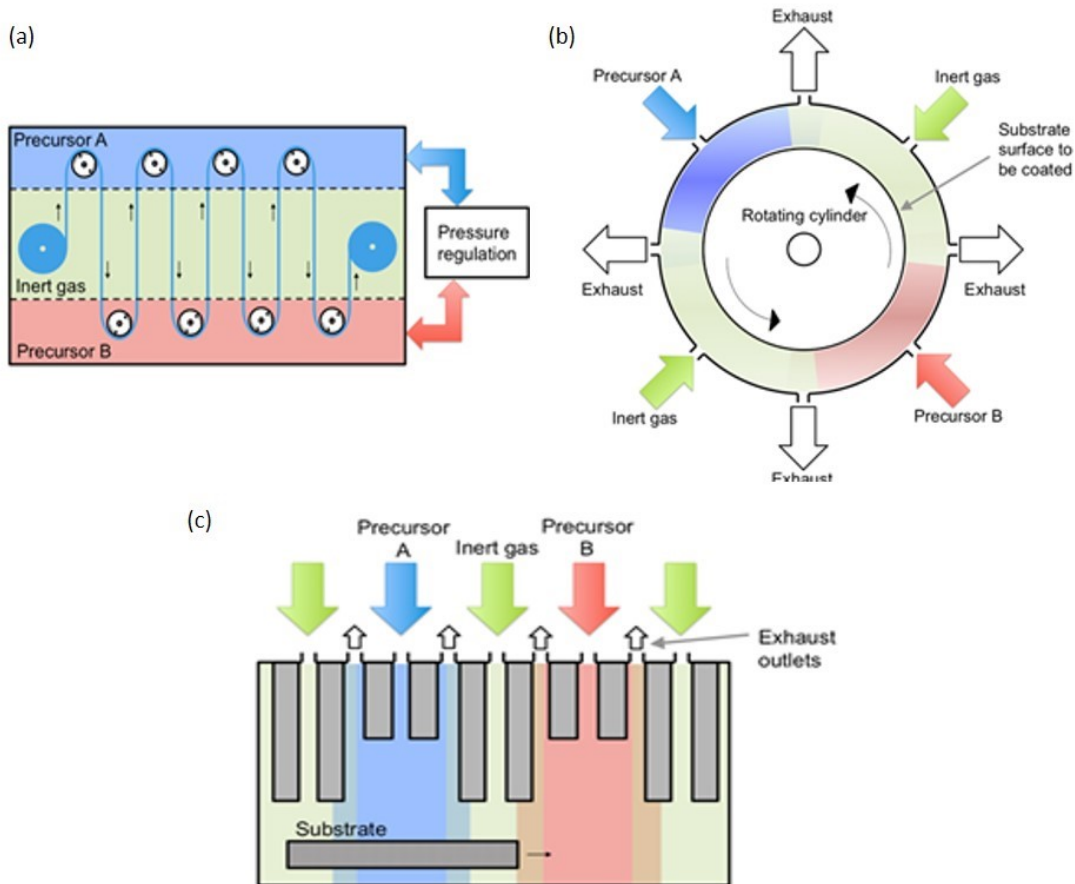


Figure 1.3 Schematic illustrations of spatial atomic layer deposition techniques based on (a) circulating flexible substrates, (b) rotating substrate cylinders, and (c) linear “zone-separated” precursor regions. All approaches spatially isolate precursor gases A and B from one another. Adapted with permission from [1]. Copyright 2016 American Chemical Society.

SALD has been achieved via various systems such as circulating flexible substrates, rotating substrate cylinders, and linear "zone-separated" gaseous precursor regions, as shown in Figure 1.3 [1].

More recently, a variant of SALD called Atmospheric Pressure Spatial ALD (AP-SALD) that operates in open-air has been introduced [12]. In this method, the substrate is placed in close-proximity (~100 micrometers gap spacing) underneath a reactor head with thin parallel slits that are narrowly separated (~few millimeters) from each other. The precursors and inert gases are flowed through the reactor head and out from the slits impinging on the

substrate surface, similar to that of Figure 1.3c. As the substrate passes through precursor A, adsorption occurs creating a layer of the precursor on the substrate surface. Then the substrate passes through the inert gas zone before passing through precursor B which reacts with the adsorbed precursor layer on the surface to produce one monolayer of film. Again, the substrate is oscillated back and forth until a desired film thickness is achieved. The small gap spacing, narrow slit separation, and inert gas curtains act to keep the precursor gases separated and isolated from the surrounding air, eliminating the need for vacuum equipment. The precursor gases are produced by bubbling the liquid precursor sources with inert carrier gas, which are then delivered to the reactor head.

A lab-scale AP-SALD system based on the close-proximity approach discussed was constructed at the University of Waterloo in Dr. Kevin Musselman's lab in 2018. Figure 1.4 shows the lab-scale AP-SALD system that was constructed by co-op and graduate students from the University of Waterloo. The manual micrometer adjustment knobs are used to adjust the reactor-substrate gap spacing. The substrate is held onto the heating stage and oscillated via the linear actuator during deposition. Figure 1.5 illustrates how the precursors are bubbled and carried, using the nitrogen source, to the reactor head for deposition. The system is designed for producing films up to 50 mm by 50 mm in area, suitable for small substrates up to 70 x 70 mm for research purposes.

The system has been used to demonstrate the efficacy of the open-air technique through multiple applications. One of the culminated works include the testimony in which clean room fabrication is no longer a requirement to produce metal-insulator-metal diodes that are better in performance than those produced using plasma-enhanced ALD [13]. Furthermore, the AP-SALD system was used to deposit zinc oxide films as an electron injection layer on the cathode side for light emitting devices [14].

While the lab-scale AP-SALD system works as a primary proof-of-concept, it must still

prove itself as a scalable technique for producing high-quality ultra-thin films at high throughput for industrial applications. While traditional vapor-based techniques such as CVD and PVD can produce films with satisfactory film quality and thickness control at fair speeds, they often compromise on scalability due to the need of vacuum chambers. Alternatively, there are other open-air thin film manufacturing techniques that can produce films at high throughput such as gravure printing, screen printing, knife-over-edge coating, slot-die coating, inkjet printing and spray deposition. However, they tend to produce films with poor quality and inferior thickness resolution [1].

Since AP-SALD separates the different precursor exposures in space rather than in time, it is 1-2 orders of magnitude faster than conventional ALD. More importantly, it leverages on the key benefits of ALD while offering speeds that are comparable to industrial thin film manufacturing systems. Furthermore, with the elimination of a vacuum chamber, the technique is not only easily scalable, but cost effective. The reactor head design which somewhat mimics that of a printer head also allows the technique to be compatible with high-throughput roll-to-roll manufacturing. AP-SALD has been demonstrated on several substrate materials such as glass, Si wafers, metal foils, polymers and fabrics [15–18]. With the combined advantages, AP-SALD is a promising technology to accelerate the research, development and commercialization of next-generation devices such as photovoltaics, solid-state batteries, smart windows, high-end logic chips and flexible electronics.

A pilot-scale system based on the lab-scale system was designed and constructed at the University of Waterloo in Dr. Kevin Musselman's lab in 2020. The system was developed to test and validate the scalability of the AP-SALD concept. The pilot-scale system was designed to deposit over large areas above 15 cm by 15 cm with high throughput above 3000 substrates per hour. The system was developed by Chee Hau Teoh, Manfred Kao and I, for which I assisted mostly with the mechanical design, fabrication and construction of the

system as well as took the lead in developing the custom-designed heating stage. Chee Hau and Manfred worked on the overall development of the system from the ground up which includes system conceptualization, selection of mechanical and electrical components, programming, automation, integration and everything else in between. The system was made possible with the tremendous support from Dr. Kevin Musselman, the engineering machine shop, the electronics technical staff, and the equipment suppliers. Figure 1.6 shows the main sections of the pilot-scale AP-SALD system which includes a Human-Machine Interface (HMI), a bubbling section and a deposition section. The details and discussion of the entire construction of the pilot-scale AP-SALD system are reported in the Master of Applied Science thesis by Chee Hau Teoh presented to the University of Waterloo in 2020.

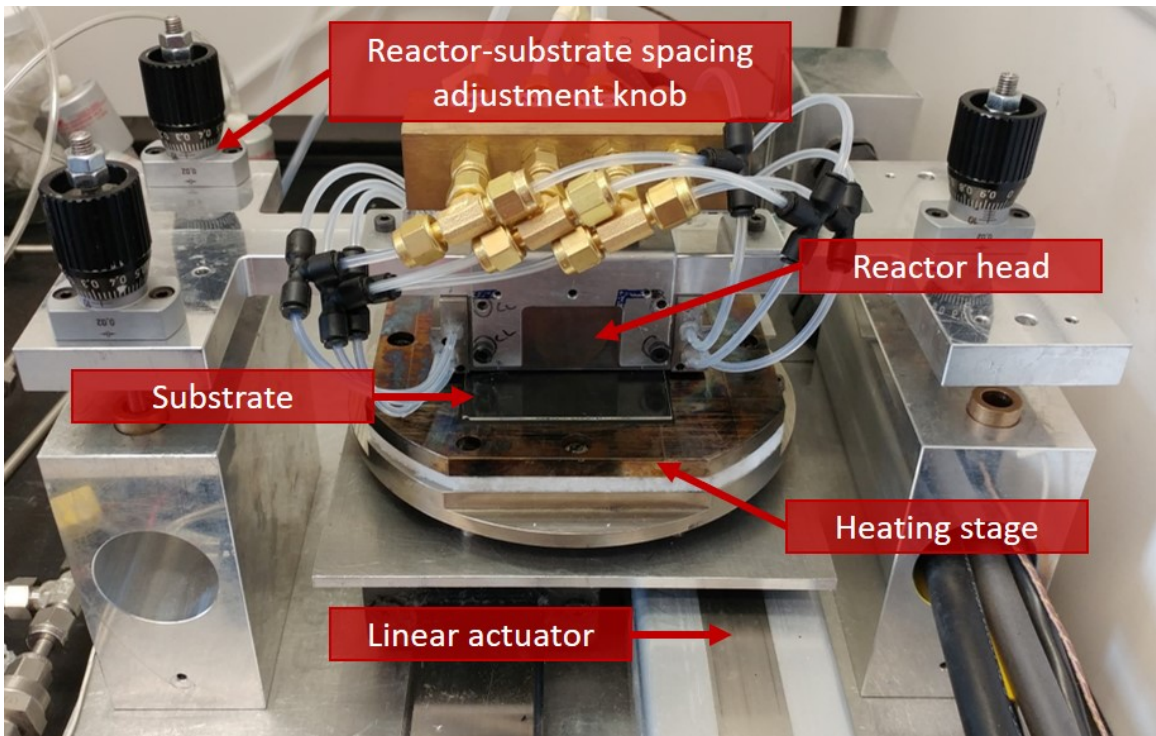


Figure 1.4 A photo of Dr. Kevin Musselman's lab-scale AP-SALD at the University of Waterloo. Obtained with permission from Chee Hau Teoh.

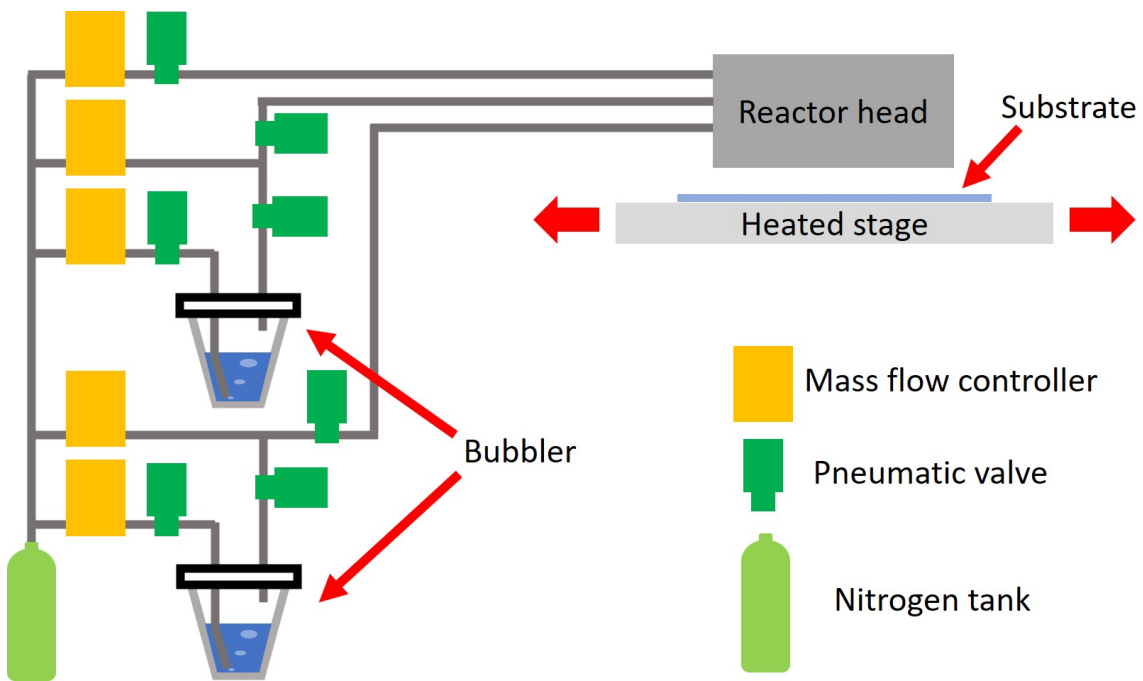


Figure 1.5 A schematic of Dr. Kevin Musselman's lab-scale AP-SALD at the University of Waterloo. Adapted with permission from Chee Hau Teoh.

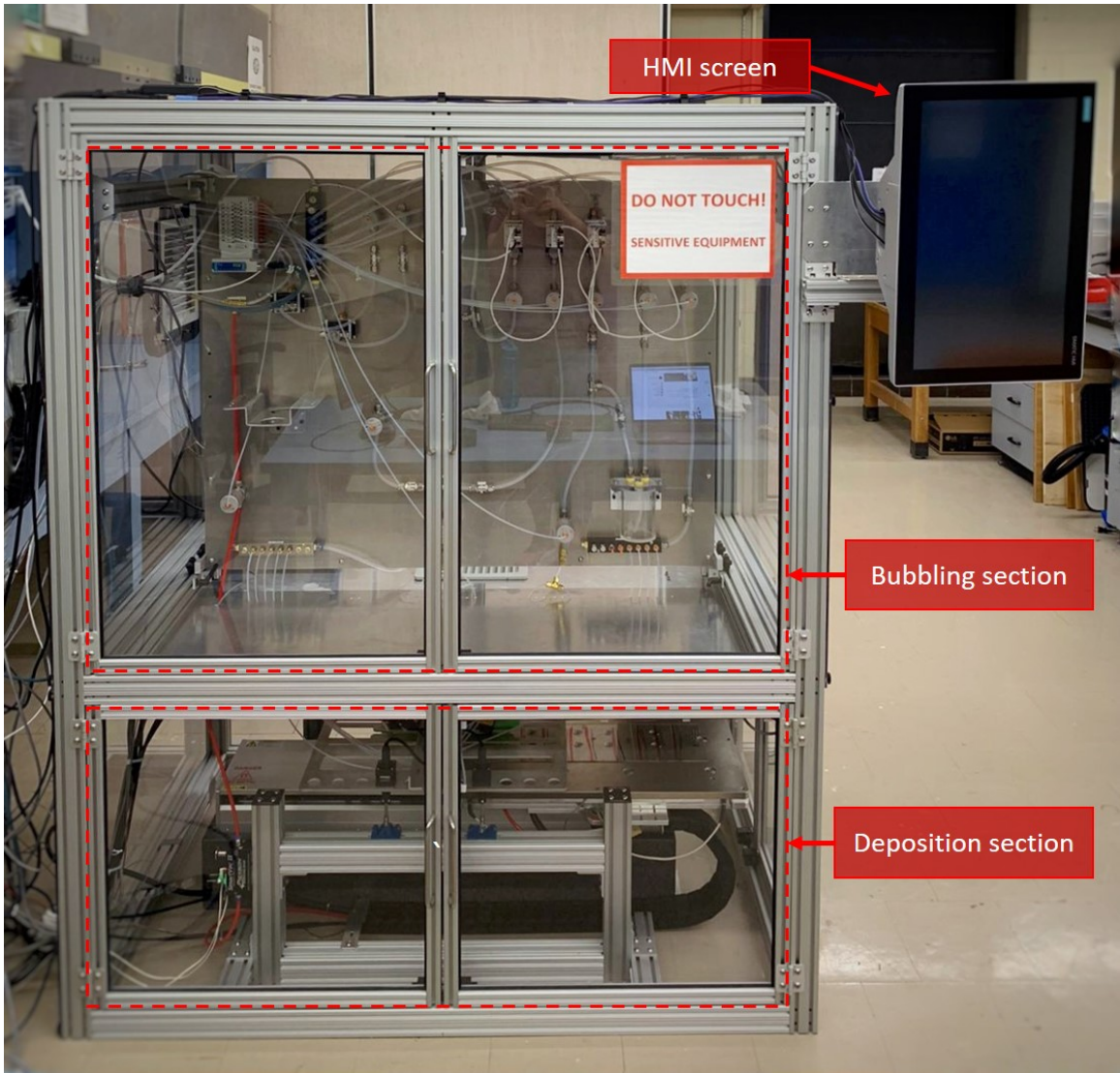


Figure 1.6 Photo of the pilot-scale AP-SALD system in Dr. Kevin Musselman's lab at the University of Waterloo. Obtained with permission from Chee Hau Teoh.

1.3 Thickness gradient films and applications

As nanoscale coatings play such a critical role in virtually all modern devices, it is important to optimize the film properties for superior device performance. To do so, researchers typically make several batches of devices, each with different film thickness, and the process is repeated for each film in the device. Not only does this method consume a lot of raw materials and is time-consuming, more importantly the iterated material synthesis process introduces unavoidable experimental artifacts due to the differences in experimental conditions. One way to prevent the experimental artifacts is through combinatorial high-throughput (CHT) techniques where the film properties vary across the film [19]. This technique enables multiple devices with varying properties (e.g. mechanical, electrical, optical, etc.) to be fabricated and tested all at once without having to go through batch processing. Such techniques reduce the consumption of materials, accelerates the prototyping and optimization of devices, and eliminates the batch-to-batch variations. Materials developed by CHT experiments are used in areas such as electrochemical catalysis, electronics, sensors, and biomaterials.

One method to perform CHT synthesis is by making films with thickness gradients as shown in Figure 1.7. Such combinatorial synthesis of films can be applied to numerous applications. Some notable examples include enhancement of ionic transport in micro-solid oxide fuel cells and lithium ion batteries [20], optimizing performance of semiconductor devices like solar cells and logic chips [21], tuning of solid-state organic light emitting diodes [22], understanding the impact of film thickness on phenomena such as wetting, block copolymer morphology, and crazing/fracture [23]. Furthermore, thin film CHT techniques have the capability to enable the discovery of new materials with unique functions and optimize existing materials through compositional alloying and doping [24].

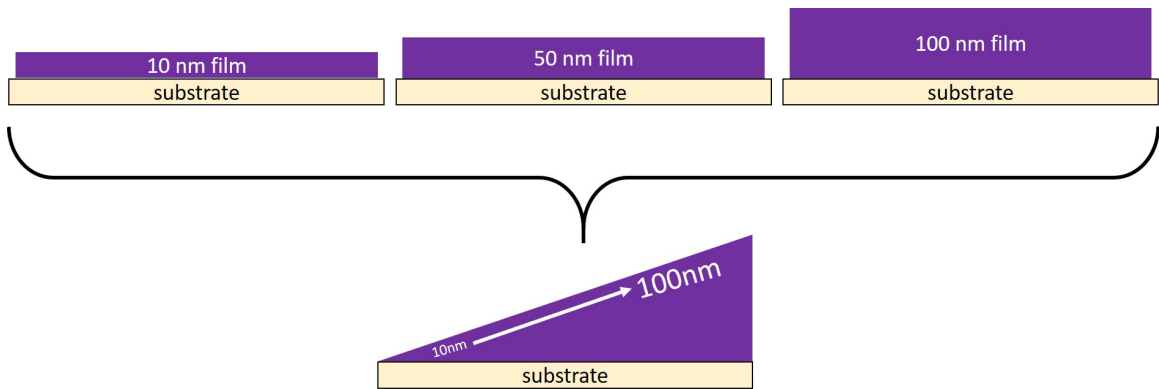


Figure 1.7 A representation of the concept of film with thickness gradient

1.4 Thesis overview

In this thesis, literature reviews on the current state of the art of synthesis of thickness gradient films and AP-SALD designs are detailed in Chapter 2. The design, fabrication and testing of custom 3D printed gradient AP-SALD reactors are detailed in Chapter 3. The design and construction of the heating stage for the pilot-scale AP-SALD are discussed in Chapter 4. Conclusions and areas for future work will be addressed in Chapter 5.

Chapter 2

Literature Review

2.1 Previous methods for making thickness gradient films

Various ways have been established to produce thin films with thickness gradients such as PVD coupled with intelligent shadow masking [25], and controlled gas flow into chamber-based ALD and CVD [26–28]. Table 2.1 is a summary of some methods that can produce films with thickness gradients. Most techniques reported require the need of high vacuum chambers which are not suitable for cost-effective and high-throughput manufacturing in atmospheric conditions.

On the contrary, atmospheric based techniques for producing thickness gradient films are less developed despite its advantages for many emerging technologies such as next-generation batteries, thin film solar cells, display technologies, ultrathin film semiconductors, flexible electronics and smart windows. Nevertheless, the established atmospheric based techniques produce films in the range of several hundreds of nanometers and some – for example spray pyrolysis – have issues with reproducibility. A flow coating technique has shown the ability to produce polymer films with thickness gradients on the order of 10 nm in atmosphere, but it has not demonstrated the capability for most classes of materials on the scale of nanometers. The ability to produce metal oxide films with thickness and composition gradients on the nanometer scale in open-air is a capability that has not previously been demonstrated.

Table 2.1 Existing methods that can produce thickness gradient films

Pressure types	Fabrication Method	Thickness gradient film	References
5* Vacuum-based synthesis	Physical Vapor Deposition	$La_{0.8}Sr_{0.2}(Mn_{1-x}Co_x)_{0.85}O_{3\pm\delta}$ (80-175 nm)	[20]
	High Vacuum CVD	TiO ₂ (50-400 nm)	[26]
	Sputtering	Cu (200-900 nm)	[29]
	Electron beam evaporation	Pd (0-50 nm)	[30]
	ALD	W (0-50 nm)	[27]
4* Atmospheric pressure synthesis (no vacuum)	Atmospheric Pressure CVD	Mixed Vanadium Oxide and Vanadium Oxynitride (90- 775 nm).	[24]
	Spray Pyrolysis	TiO ₂ (100-300 nm) Cu ₂ O (200-600 nm)	[21]
	Flow Coating	Polymer (90 nm to 140 nm), sub 10 nm	[23] [31]
	Horizontal Dip Coating	3 different polymers (200-350 nm) deposited on tilted stage	[22]

In Chapter 3, a method to produce zinc oxide films with nanoscale thickness gradients in open-air using the lab-scale AP-SALD will be discussed.

2.2 Previous CFD modelling of AP-SALD reactors

Computational Fluid Dynamics (CFD) is a branch of fluid mechanics that uses numerical analysis to analyze and solve problems involving fluid flows. The calculation is often carried out with the aid of a computer. CFD is a powerful tool to simulate various aspects of fluid mechanics including flow pattern, velocity, pressure, heat transfer, turbulence, and molar fractions to name a few. It is used in a wide variety of applications ranging from thermal management in consumer electronics, to airflow over airplane wings, air ventilation in a building, and wildfires. Likewise, the multitude of benefits that CFD offers have guided many aspects of ALD and AP-SALD in general which enables smarter design of experiments, provides key insights on reactor designs, and predicts reaction mechanisms for optimization.

CFD is typically broken down into four major steps – problem identification, pre-processing, solving and post processing. In problem identification, one must define the goals and the domain of the fluid problem. Pre-processing is the most involved step which consists of geometry modeling, meshing, definition of the related physics and configuration of the solver settings. Geometry modeling is where the fluid system is constructed, often with the assistance of 2D or 3D Computer Aided Design (CAD), to represent the domain to be analyzed. Meshing is where the constructed system is divided into small elements that can be used as discrete local approximations of the larger domain, an example is shown in Figure 2.1.

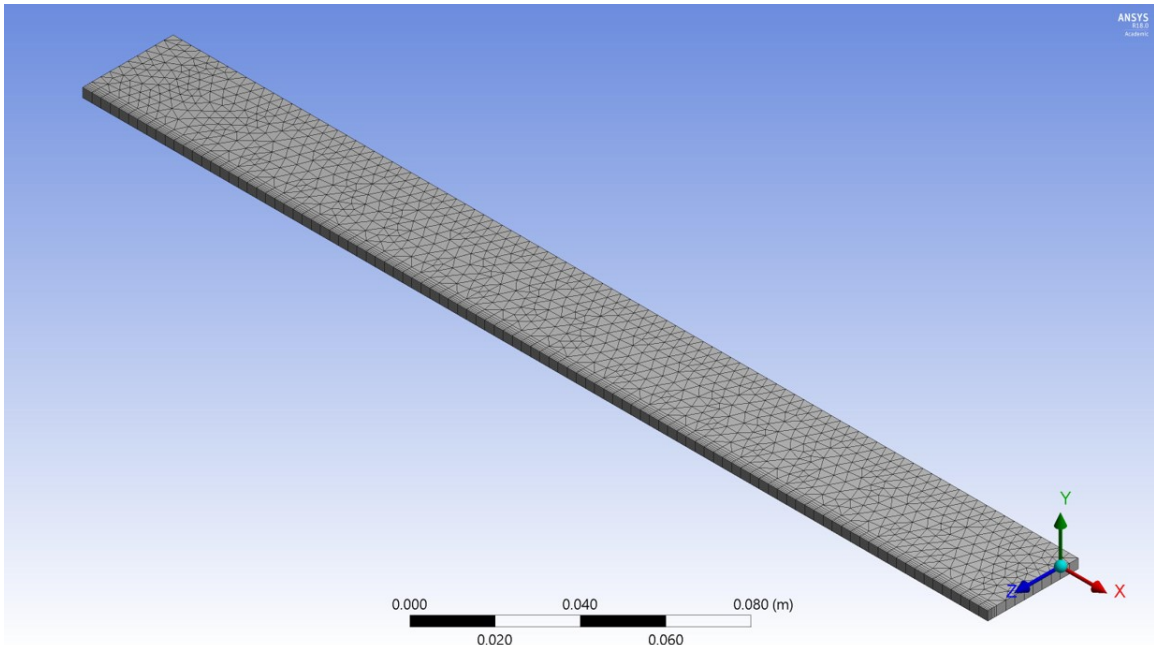


Figure 2.1 Example of a mesh for CFD analysis

Figure 2.2 shows the most common types of mesh element shapes. The physics is where different phenomena may be coupled into the simulation, for example heat transfer, mass transfer, vibration, chemical reaction, and types of flow. Solver setting is where the boundary conditions (such as velocity and pressure at inlet and outlet), type of turbulence model, solver schemes, convergence criteria, state of the simulation (transient or steady), fluid properties and such are defined. After the pre-processing comes the solving step, which is where the computer computes a set of equations describing the physics involved in an iterative manner until the solution converges to the defined convergence criteria. Finally, post-processing is where the user examines and draws meaningful data from the results produced.

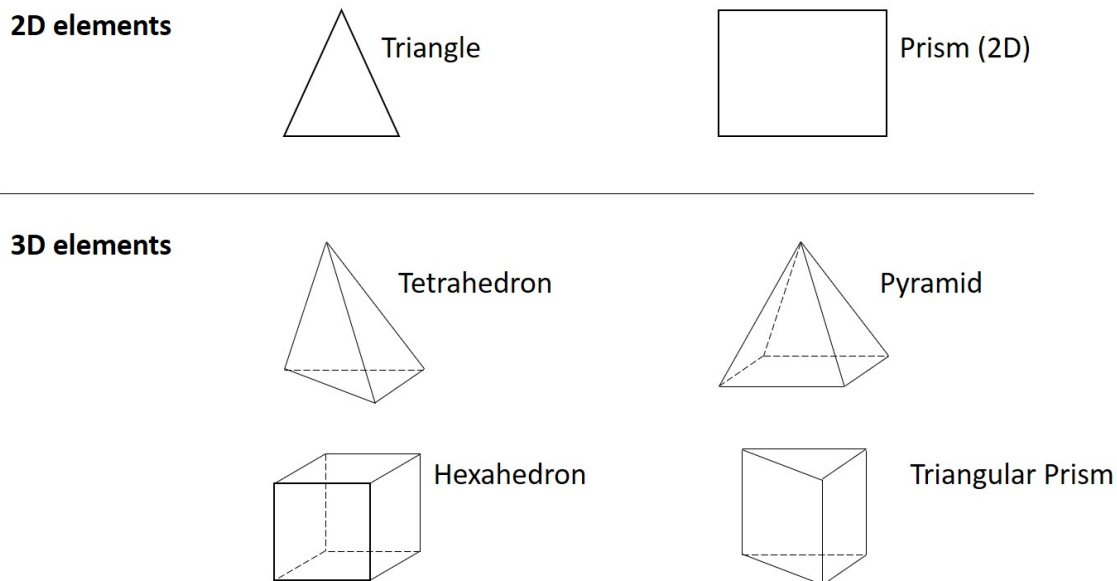


Figure 2.2 Most common element types for CFD mesh definition

CFD has been used to model the flow, diffusion, and heat transfer of an ALD micro-reactor head to calculate the pulses of reactant species and separations by purge streams [32]. The simulation helped optimize the micro-reactor head design in which various outlet geometries were modeled to realize a design that effectively confines the reaction zone. In another instance, CFD has been deployed to simulate the temperature distribution and flow field and concentration of precursor in an ALD chamber and on the substrate surface [33]. The simulation analyzed the importance to integrate CFD and surface kinetics coupled modelling to ALD process design and development, which were then validated through follow-up experiments [34]. CFD was also utilized to investigate the reactor inlet position, multi-inlets, chamber design, molar fraction distribution and the effects of high substrate temperatures in conventional ALD [35–37]. Despite the fact that the models discussed were based on single-wafer type ALD chambers which limit the number of substrates that can be processed, CFD simulations can be applied to commercial scale applications. For example, CFD was used to capture the velocity profile and mass fraction in a vertical furnace ALD system where 100 wafers are processed per batch [38].

Apart from chamber-based ALD, CFD has also been used in AP-SALD applications. It played a critical role in the initial development and optimization of the AP-SALD reactor head design as well as determining the operating conditions for roll-to-roll AP-SALD systems, where they were used to coat on porous (fabrics) and non-porous materials (polymers, metal foils). Notably, CFD was used to model the gas flow in and out of the reactor head, as well as on (non-porous) and through (porous) the substrate [39]. It was instrumental in predicting a certain optimal combination of web speed, gap spacing, and gas flow per slit needed to prevent mixing of the precursors before impinging on the substrate [40]. Similarly, by tweaking the geometric parameters such as gap spacing, width of slits, distance between slits, and area of exhaust in a CFD model, one can easily and quickly make informed design and experimental decisions before expending any resources [41]. The same principles can be applied to wafer-based AP-SALD systems where the wafer substrate moves or oscillates underneath the reactor as described in Chapter 1.2. An interesting example of a wafer-based AP-SALD system is one where the wafer floats on gas bearings and is moved under the reactor with a controlled gap spacing by carefully balancing the gas stream above (from the reactor) and below (gas bearings) the substrate, as shown in Figure 2.3. CFD was used to model the viscous drag and pressure difference on the substrate to determine the required force balance to keep it afloat with a specific gap spacing as well as the substrate translation speed [42].

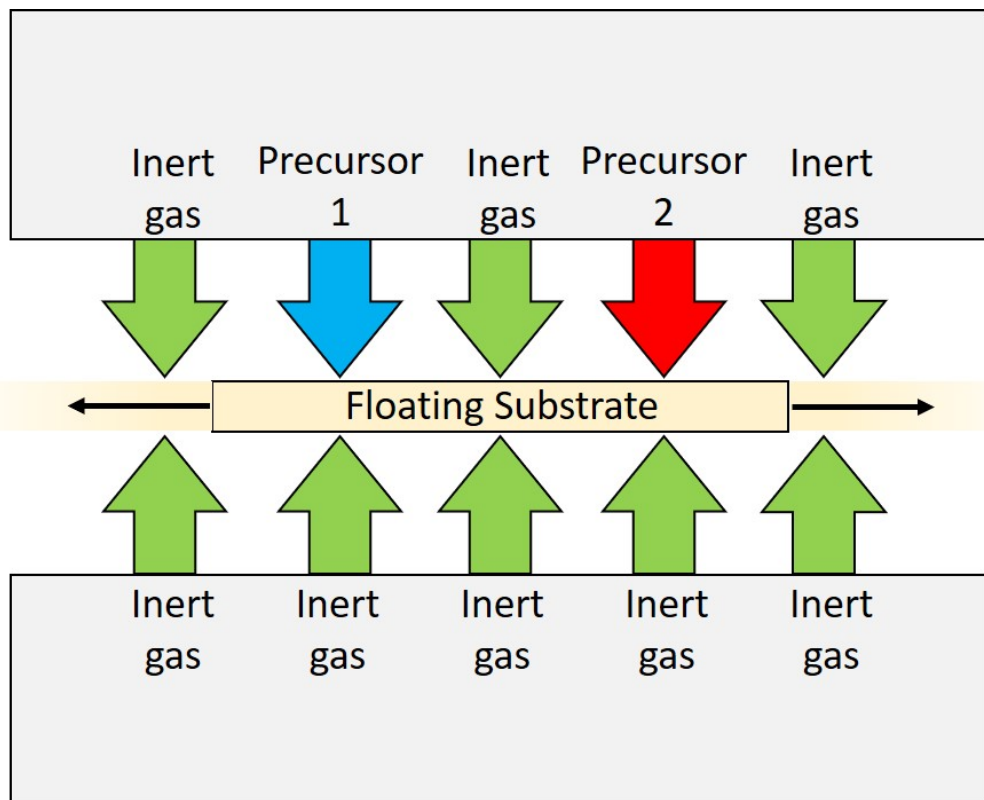


Figure 2.3 SALD floating substrate concept

2.3 Previous 3D printing of AP-SALD reactors

3D printing is a form of additive manufacturing process to construct a three-dimensional object from CAD model where material is being added and joined typically layer by layer. There are many types of additive manufacturing such as vat photopolymerization, material extrusion, material jetting, binder jetting, powder bed fusion, direct energy deposition and sheet lamination. These technologies can range from small desktop size to large commercial grade machines, producing parts anywhere from plastic, to metal, ceramic, and elastic materials.

The recent emergence of low-cost desktop 3D printers has driven rapid prototyping to a new paradigm. The most popular desktop 3D printers use fused deposition modeling technology where a thermoplastic filament is heated to its melting point and extruded continuously to form the product layer by layer. While fused deposition modeling offers prototypes to be produced at a high speed and at a low cost (accessible to the masses), it compromises on other aspects such as surface quality, feature details, dimensional accuracy, and watertightness.

On the contrary, despite costing more, desktop stereolithography (SLA) 3D printers such as the ones from Formlabs, can produce thermoset plastic parts that are dimensionally accurate, isotropic, and watertight with excellent surface quality and superior feature details. The SLA 3D printing process builds the part layer-by-layer using a laser source in the XY-direction to draw and cure each cross section to solidify the part from a liquid photopolymer resin pool as the part moves in the Z-direction. Interestingly, the same printer can be used to print a variety of resins for different applications. For example, the types of resins available such as high temperature, flexible and ceramics enable a wide range of engineering applications that require specific functional properties.

3D printing had been used to produce reactors for ALD and SALD applications. For

example, a ceramic rocket nozzle set was 3D printed for a superfast plasma ALD reactor [43]. The 3D printed ceramic rocket nozzle set comprises of alternating precursor nozzles arranged in a circle which surrounds a wafer substrate. Alternating short pulses (<10 ms) of precursors are introduced all-round the surface of the wafer to produce the ALD layers at high speeds. In another example, a Formlabs SLA printer had been used to create a dielectric barrier discharge plasma for a SALD reactor head with the goal to assist the SALD process by generating reactive species to the substrate surface [44, 45]. Not only does the 3D printed parts perform well as a dielectric barrier, it also allows for quick prototyping and testing of various plasma arrangement geometries for optimization. It was found that the thicknesses of the plasma arrangement influences the distribution of micro discharges on the dielectric surface. Doing so also affects the power dissipation as well as the formation of ozone through electrical and chemical characterizations, respectively.

Similarly, the Formlabs SLA printer had also been used to produce customized lab-scale AP-SALD reactor heads [46]. The reactor head design is made up of sophisticated network of inner distribution channels, which makes it impossible to be manufactured by traditional means without necessitating multiple assembly parts. Nevertheless, the 3D printing process allowed for a monolithic design to be realized. Additionally, it opens the possibilities for even more complex inner channel geometries. The reactor heads were tested to produce metal oxide films efficaciously. Furthermore, the low-cost rapid prototyping nature of 3D printing allows for different reactor designs to be fabricated and tested quickly. It also enables various reactor designs with unique functionalities to be fabricated. For example, one design which includes two different metallic precursor outlets that overlap on the central part of the deposition area has been used to create a zinc oxide/copper oxide/zinc oxide film stack [46]. Another unique design called “SALD pen”, resembles the function of a pen to draw zinc oxide films, resulting in an area-selective deposition effect [46]. Chapter 3 discusses the design for a printing process of a lab-scale AP-SALD reactor head that produces nanoscale

films with thickness gradients, as well as a commercial-scale AP-SALD reactor head that produces films nine times the size of the lab-scale reactor. The chapter also discusses the best practices and lessons learned from printing the reactors on a Formlabs SLA machine.

2.4 Design of AP-SALD systems

There have been recent developments in AP-SALD systems, most of which are still in the early phase or in research settings. Eastman Kodak for example developed an AP-SALD system where a series of hydrodynamic gas flow – precursor and inert gas, from the reactor under the substrate supports and moves the substrates, like a gas bearing. The reactor head design leverages on the thin narrowly separated slits configuration as described in Chapter 1.2. Since the substrate floats on the gas bearing, a small substrate-reactor gap can be maintained, hence achieving AP-SALD. The group worked on thin film transistors where aluminum oxide and zinc oxide films were deposited with their system.

A group at The University of Colorado at Boulder developed a system where the reactor is placed at close-proximity (approx. 100 microns) above the substrate, instead of having the substrate float on top of the reactor like in the Kodak system. Again, the reactor design uses the same thin narrowly separated slits configuration. The substrate is mounted to a frictionless translation table, where the substrate oscillates underneath the reactor to grow the films. The reactor head is mounted to micrometers which can be used to mechanically adjust the gap spacing of the deposition. Such a set up allows for testing of the influencing factors of gap spacing, substrate translation speed and gas flow rates on continuous AP-SALD. Aluminum oxide ALD films were deposited to demonstrate the system capability. However, the experiments revealed that mechanically adjusted gap spacings are difficult to maintain during the substrate oscillation.

Another example can be found at The Netherlands Organizations, an independent research organization, that developed an AP-SALD system which uses a round reactor head as shown in Figure 2.4a. The reactor head separates the precursor zones by the gas bearing plane. Each precursor slit is surrounded by exhaust zone. The substrate is placed on a servo-driven

rotating table at close-proximity below the round reactor head. The substrate is then rotated for which the substrate will be exposed to different precursor zones as shown in Figure 2.4b. The assembly is placed in an oven to provide the heating necessary to facilitate the gas reaction on the substrate surface.

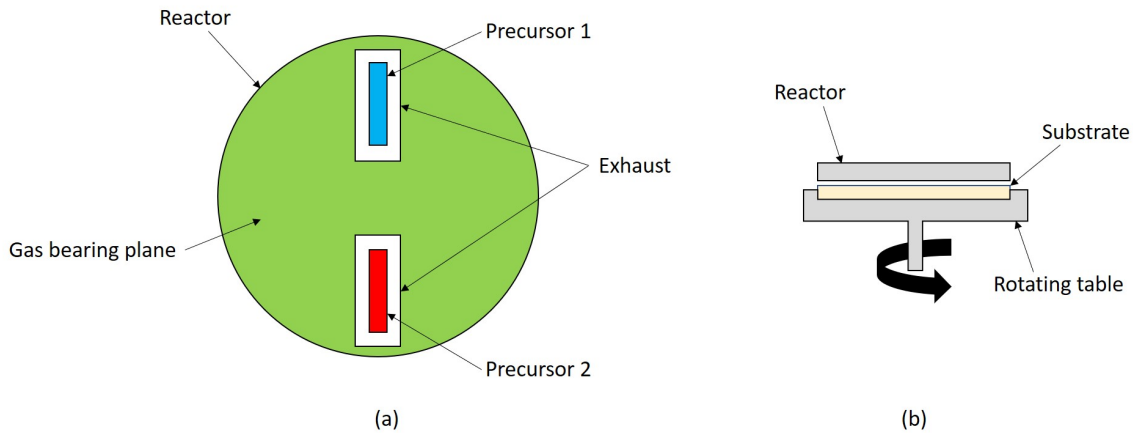


Figure 2.4 SALD round reactor concept

Companies like SoLayTec, Levitech, and Beneq have developed different variants of the AP-SALD. SoLayTec, a spin-off from TNO and Levitech, a spin-off from ASM International both use the floating substrate configuration, where the substrate is floated in between two gas streams (reactor above and gas bearing below), just as described in Chapter 2.2. The SoLayTec system is used to deposit aluminum oxide passivation layers for entire solar cell wafers (150 x 150 mm) by oscillating four times per second between the precursor zones. By default, the substrate only gets exposed to one metal precursor gas slot per oscillation, producing an effective deposition rate of 0.45 nm/s and throughput of the order of 100 wafers per hour based on a passivation layer thickness of 10 nm. Nevertheless, the system is modular and can integrate two to three metal precursor slots, and up-scaled to incorporate 10 to 15 reactors in parallel for throughput numbers over 3000 wafers per hour. On the other hand, the Levitech system passes the wafer through a series of precursor exposures in 1 s resulting in a throughput of 3600 wafers per hour. Similarly, the design

is somewhat modular in that the number of precursor slots represents the number of ALD cycles and hence the layer thickness through the reactor. The Levitech system successfully demonstrated the ability to deposit aluminum oxide passivation layers with thickness in the range of 5 to 10 nm on full solar cell wafers. However, one of the downsides of the systems is that they are designed for a specific wafer size and thickness, limiting the flexibility. Furthermore, the substrate heating process typically takes places in the beginning and the end of an oscillation, affecting the deposition properties due to non-continuous heating. The requirement to carefully balance the gas bearings and to ensure a consistent gap spacing also makes it challenging to optimize.

In another instance, Beneq developed a rotating system, WCS 600, for roll-to-roll applications to coat flexible materials such as polymer and metal foils up to 500 mm wide. The reactor drum consists of multiple precursor slots which are separated by inert gas bearings as shown in Figure 2.5. The foil is kept at a fixed close-proximity to the reactor drum with the help of the gas bearings. As the foil moves over the drum and gets exposed to alternating precursor zones, an ALD film is then deposited. The deposition rate can be tuned by rotating the drum in the direction opposite to the direction of movement of the foil. With a static reactor drum, the system can produce 1 nm film at a throughput rate of 30 m per minute. Whereas with a rotating reactor drum, the throughput reaches 1 m per minute for a 10 nm film. It has been tested with materials such as aluminum oxide ($\pm 2\%$ uniformity), titanium oxide, zinc oxide and silicon dioxide. Such a system is particularly useful for flexible electronics which include flexible displays, flexible organic light emitting diodes, flexible solar cells, and batteries.

Chapter 4 discusses the design of a heated stage for a commercial-scale AP-SALD system at The University of Waterloo. The stage is designed and built to heat (up to 300 °C), hold large-area (>150 x 150 mm) substrates and oscillate under a reactor head for the deposition.

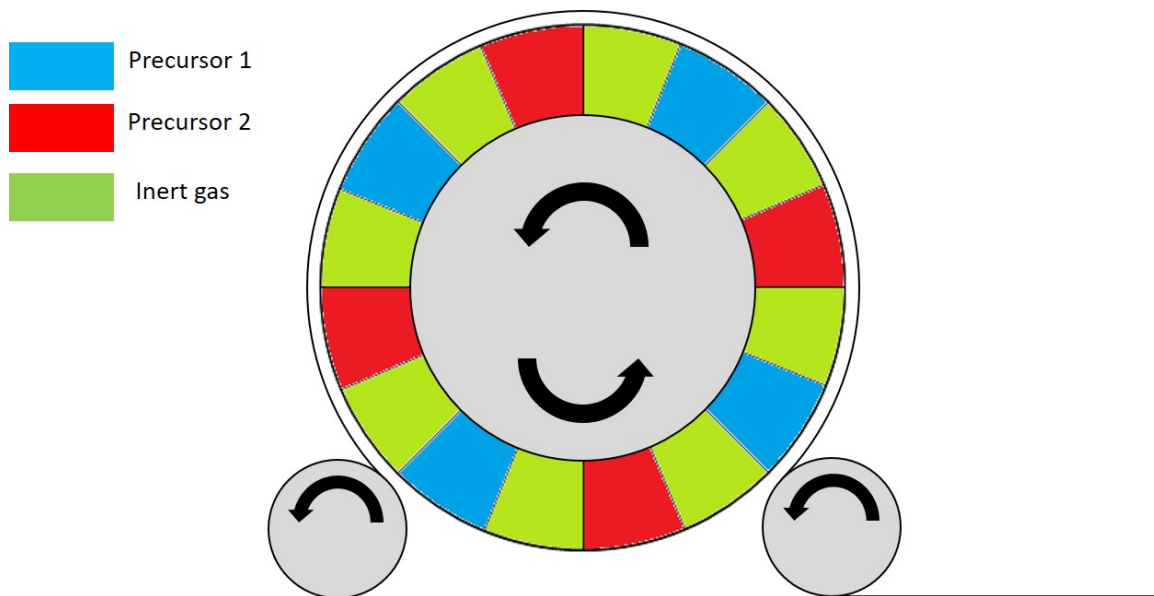


Figure 2.5 SALD for roll-to-roll process

The chapter will also discuss the design and 3D print of a reactor for the commercial-scale AP-SALD system.

Chapter 3

Gradient AP-SALD reactors

3.1 Chapter overview

Since the concept of producing nanoscale gradients using an AP-SALD reactor has never been previously reported in literature, there are many unknowns to begin with in terms of how to approach the problem, and what tools should be used. At The University of Waterloo, my colleague Abdullah Alshehri produced gradient films by tilting the AP-SALD reactor so that one side has a larger gap spacing than the other creating a region with more precursor cross-talking/mixing, which results in more CVD than ALD, as shown in Figure 3.1. This leads to a graded growth rate across the substrate (varying between AP-SALD and AP-CVD across the substrate).

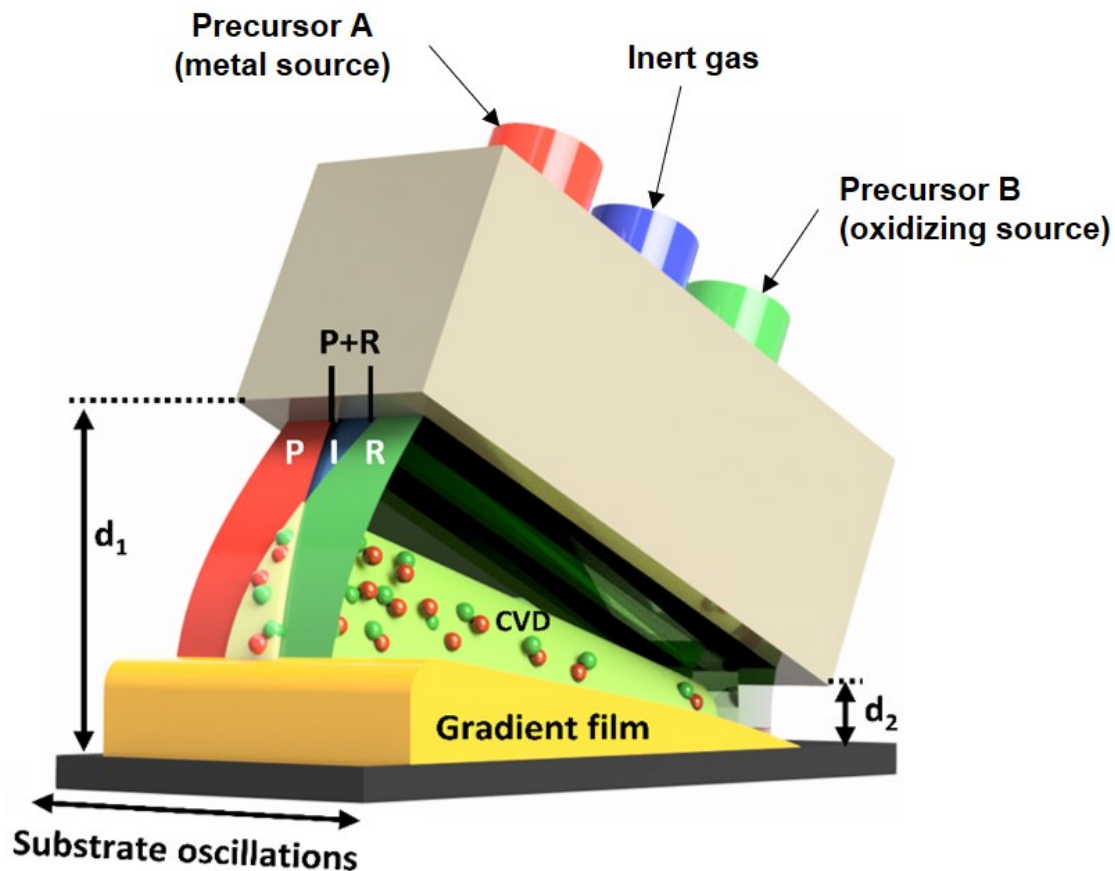


Figure 3.1 Concept of tilted reactor for depositing films with thickness gradient where d_1 exhibits a larger gap spacing than d_2 . Obtained with permission from Abdullah Alshehri

However, this method may lead to more precursors being leaked from the reactor. Furthermore, it is difficult to precisely control the gap spacing using this method. Hence, a novel customized reactor head design, which can deliver different amounts of precursor gas to different locations on the substrate while maintaining a fixed gap spacing, is needed. Figure 3.2 shows the concept of the customized reactor head design proposed.

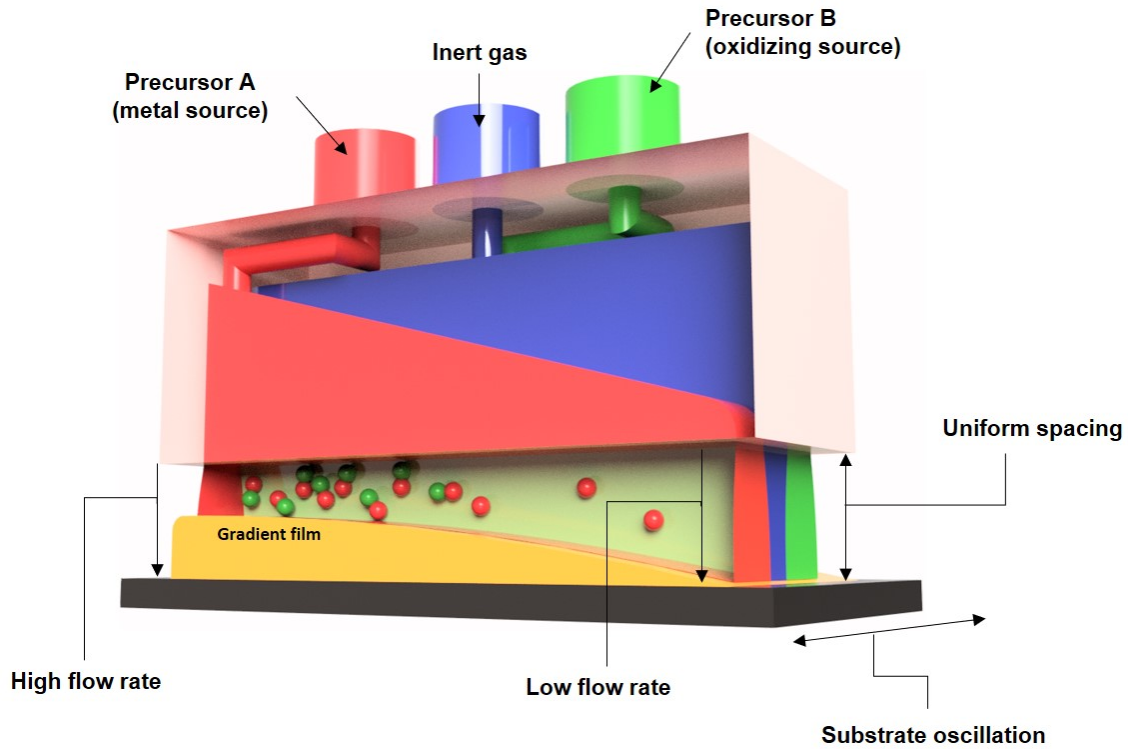


Figure 3.2 Concept of customized reactor for depositing films with thickness gradient

The motivation of the chapter is to evaluate the use of CFD modeling to guide the design of the reactor, the use of SLA 3D printing to fabricate the gradient reactor and the effectiveness of the reactor to produce gradient films. This chapter discusses the design, construction, decisions, lessons learned, challenges, simulation and experimental results of the 3D printed gradient AP-SALD reactor heads for the lab-scale system at The University of Waterloo.

Chapter 3.2 describes the experimental methods which include CFD modeling of reactor channels for producing films with uniform thickness and thickness gradients. The CFD model will reveal the main influencing factors that can affect the flow at the reactor outlet, and at what point is the flow fully developed. These parameters will then be used as the constraints for the design of the channels in the gradient reactor. Optimization of the gradient channel will also be described, where multiple channel geometries are modeled to determine the best geometry for the optimized gradient flow. The chapter will also elaborate on the design considerations, key parameters, and material selection for the reactor design to be successfully 3D printed. Finally, it will describe the triangulation code as well as the design and construction of a jig for film mapping.

Chapter 3.3 presents the results and discussions of the 3D printed gradient reactor, which includes the design of the internal network of channels and the overall monolithic design of the reactor for 3D printing. The design process will help elucidate the lessons learned and the decisions made, especially on how to handle the print and some important features to consider when designing the reactor. The chapter will then present the experimental results where the thicknesses across the film produced using the 3D printed reactor are measured. The experimental results are also compared with the CFD results to test the validity of the simulation.

3.2 Experimental Design

3.2.1 CFD modeling of reactor channels for producing uniform and gradient films

Before the CFD model of a reactor channel can be developed, some initial guiding parameters must be determined based on the capability of the 3D printing technology of choice. Since the Formlabs SLA printers are made available at The University of Waterloo for prototyping parts, most of the design considerations for the reactor are based on the design guidelines published by Formlabs and insights from the community forum. Notably, the most critical design constraints that are relevant are as follows:

- 0.5 mm minimum hole diameter
- 0.5 mm minimum distance between walls
- 0.4 mm minimum supported wall thickness

Based on the required minimum distance between walls, the width of the channel is hence constrained to 0.5 mm. To ensure that the reactors can be successfully printed, the decision was to set the channel width to 0.75 mm as opposed to 0.5 mm. As a benchmark, the lab-scale metal AP-SALD reactor, used to produce uniform films, has a channel width of 0.25 mm, which was fabricated using wire electrical discharge machining.

Using the same benchmark, a simple model that represents the metal reactor with a channel height of 15 mm and width of 0.25 mm is constructed to simulate the flow profile at the outlet of the channel. The channel consists of two inlets with 2 mm diameter and one outlet that is 50 mm long (0.25 mm wide). A structured mesh of the geometry, Figure 3.3, was

constructed to preserve flow physics and to reduce inherent numerical errors in the analysis which are common when using the default tetrahedral mesh.

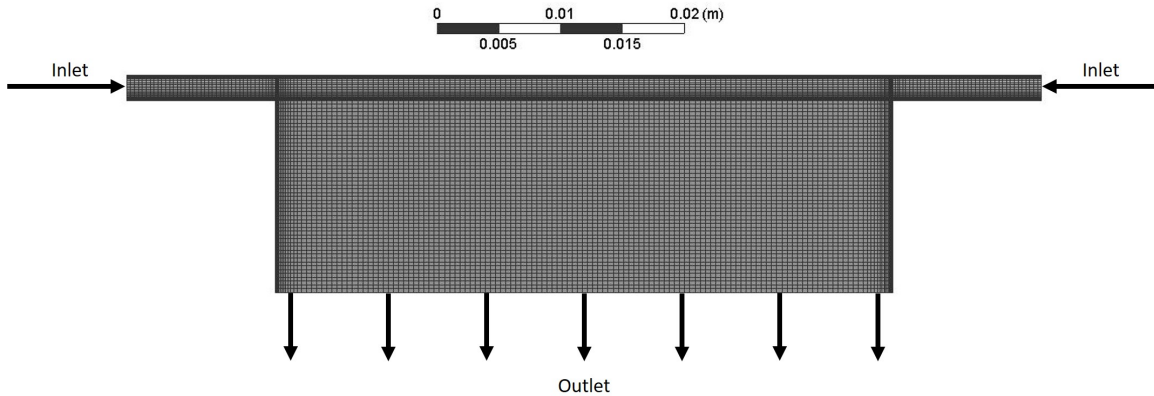


Figure 3.3 Structured mesh of the uniform channel

Figure 3.4 shows the concept of how an all-quad mesh can preserve the flow, such that numerical dissipation is minimized compared to when a tetrahedral mesh is used. A mass flow rate of velocity profile at the outlet is used as the metric to evaluate the flow profile of the precursor gas delivery from the reactor channel since velocity is proportional to the precursor flow rate. A mass flow rate of 1.56×10^{-6} kg/s at each inlet is used to reflect the typical deposition flow rate of 150 sccm per channel used in the lab. Nitrogen at normal temperature and pressure is used as the medium to simplify the CFD model. Since the channel dimensions are small (sub-millimetre to millimetre range) and the flow velocity is relatively low throughout (Reynolds number below 1000), the flow is assumed to be laminar and hence no turbulence models were used in the simulation. All meshing, simulation and post-processing were carried out in ANSYS CFX.



Figure 3.4 Difference in flow estimation between triangular and square cells

As shown in Figure 3.5a, the flow profile at the outlet is uniform with a channel width of 0.25 mm. However, when the channel width is increased to 0.75 mm, the flow profile resembles a valley (low velocity in the middle) instead of uniform as shown in Figure 3.5b. After running multiple simulations with varying channel geometries, it was found that apart from the channel width, the channel height also has strong influence over the flow profile at the outlet. This can be explained by the fact that the flow would require at least a certain travel distance before it is fully developed. A separate simulation was performed with the height increased to 40 mm to check for the point where the flow starts to be fully developed.

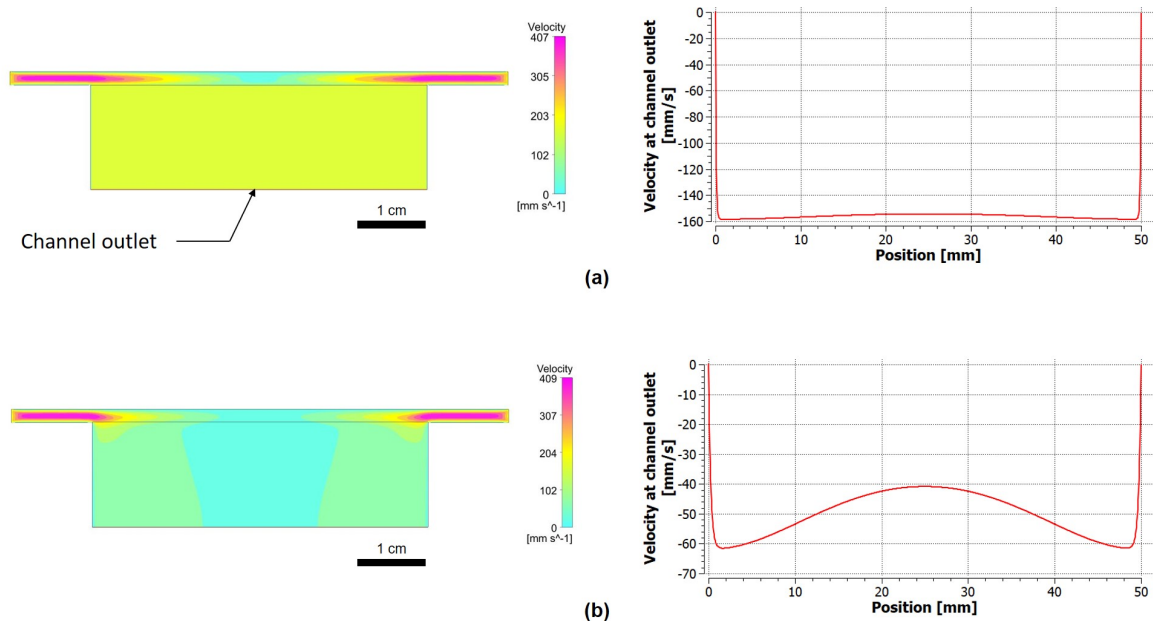


Figure 3.5 CFD analysis of the reactor channel with (a) 0.25 mm width, and (b) 0.75 mm width

Based on the CFD simulations, the flow becomes fully developed after 30 mm of travel. Figure 3.6 shows the contour plot of the velocity distribution in the channel as well as the velocity profile at different heights in the channel to determine the point at which flow is fully developed. An additional simulation with the width increased to 1.4 mm was performed to further test if having 30 mm of travel is sufficiently long to isolate from the effect caused by large channel width described in the previous paragraph.

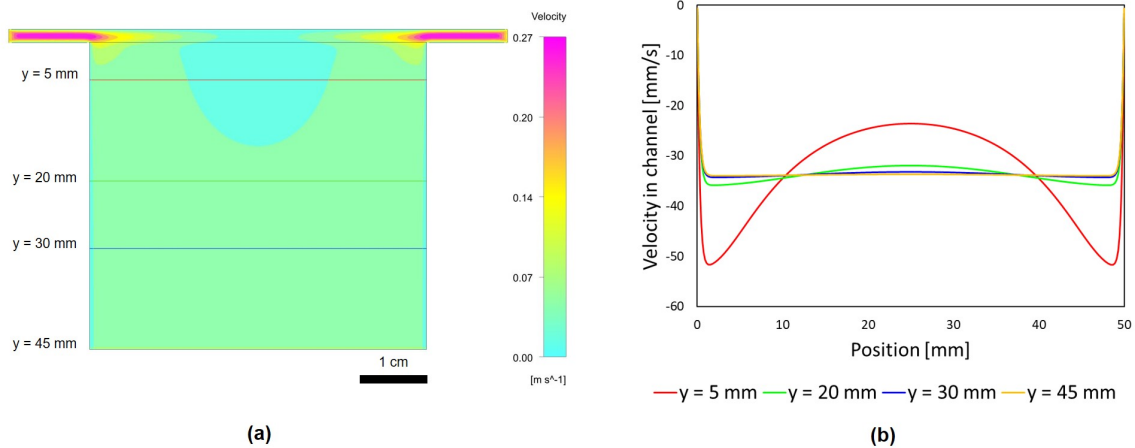


Figure 3.6 CFD analysis of the proposed 0.75 mm to determine height to achieve fully development

Figure 3.7 shows the comparison of flow profile at the outlet between a channel that is 0.75 mm wide, and one that is 1.4 mm wide. As expected, even when the channel width is increased by a factor of almost 2, the flow profile remains relatively uniform provided that the channel is sufficiently long.

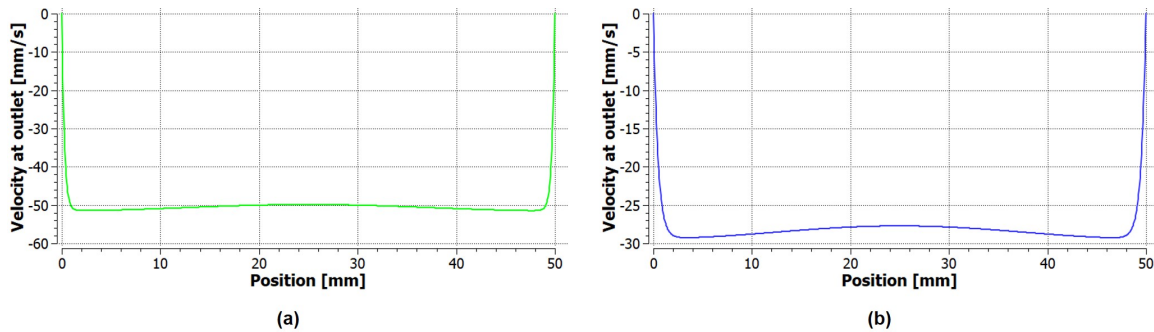


Figure 3.7 Comparison of flow profile at outlet between 0.75 mm and 1.4 mm channels (30 mm channel height)

With the channel height (30 mm) and width (0.75 mm) defined, the design process of a gradient channel is more informed and guided. Multiple gradient channel geometries were designed and modeled to achieve the desired gradient flow profile. Figure 3.8 shows the optimized gradient channel geometry which includes one inlet and one outlet.

Again, a similar structured meshing scheme and simulation conditions described in the case

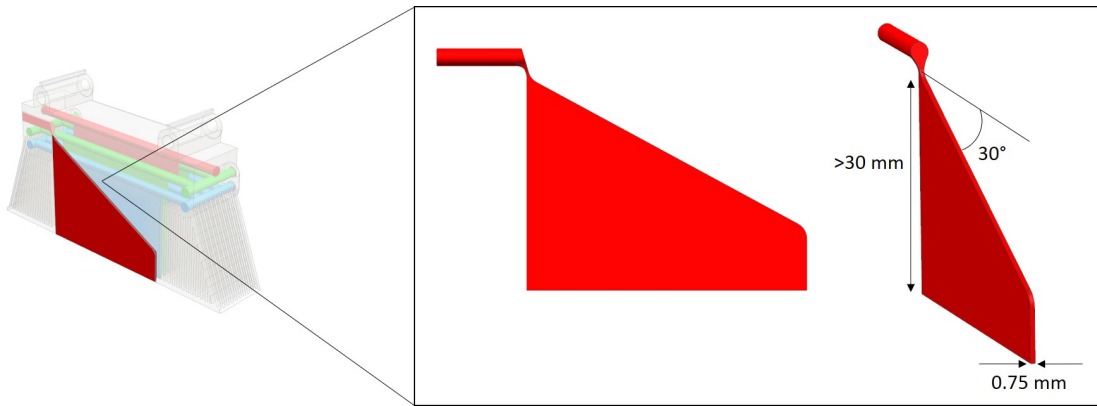


Figure 3.8 Optimized channel geometry for graded flow rates at outlet

with the uniform channel model were used to construct the model for the gradient channel. Based on preliminary CFD simulations, a 30° inlet angle was found to provide the best flow gradient profile at the outlet. On a separate note, a laminar flow regime was again assumed in this preliminary simulation because the Reynolds number is still below 1000. However, as can be seen in Figure 3.9, the transition from the inlet into the channel involves a drastic change in size such that the transition region behaves like a reducer. The small cross section at the transition region causes the flow to speed up considerably before quickly dissipating due to the channel expansion shortly after. With that in mind, given the abrupt changes and the high speeds at the transition region, turbulence may still occur in the channel.

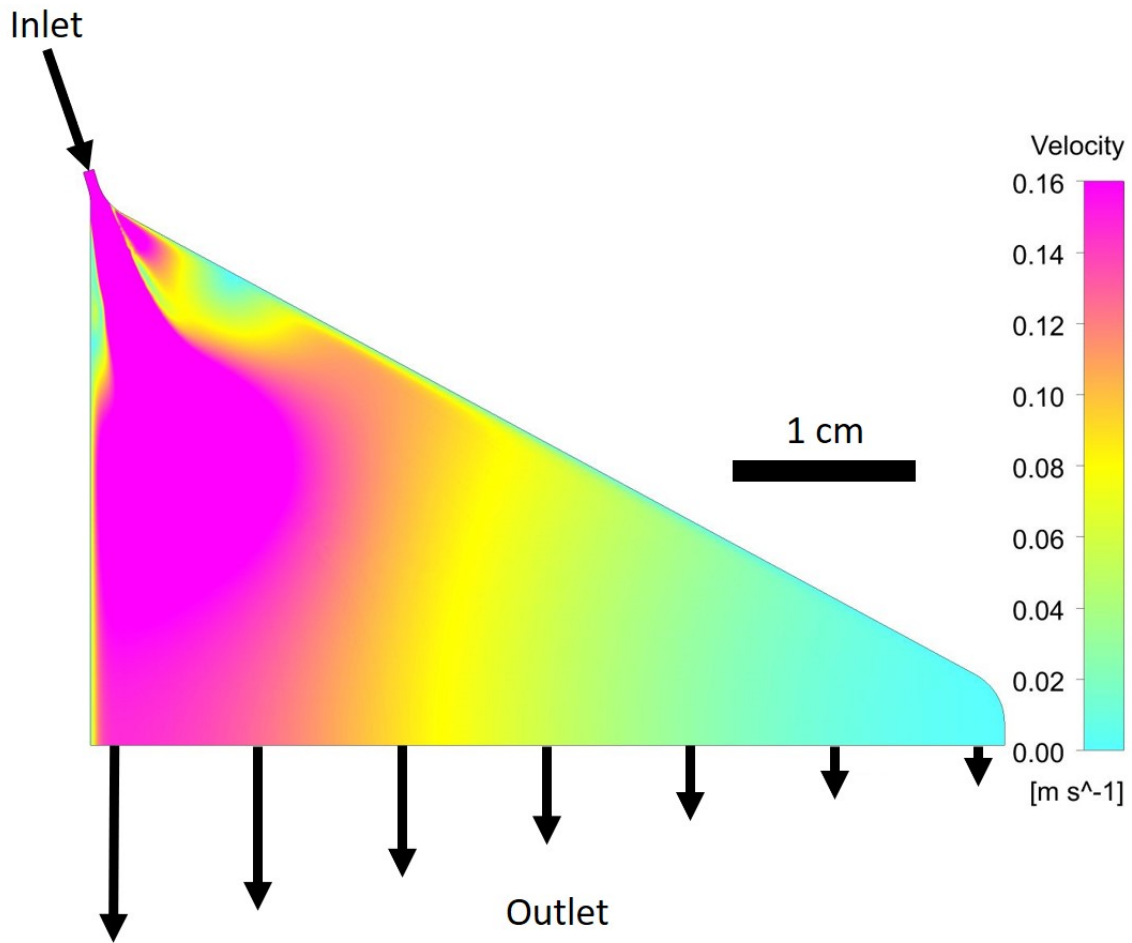


Figure 3.9 Flow velocity contour inside and at the outlet of the gradient channel

To verify the validity of the laminar assumption, two simulations with the same set up and conditions were performed, except that one assumes fully laminar flow and the other one was performed with a turbulence model. The use of turbulence models attempts to predict the effects of turbulence in a flow. The turbulent boundary layer region near the wall is typically split into three layers for building these models, namely the inner layer where viscous effect is dominant, the outer layer where large scale turbulence is dominant, and the overlap layer where the velocity profile can be represented in a logarithmic variation. Figure 3.10 shows the three layers in the turbulent boundary layer.

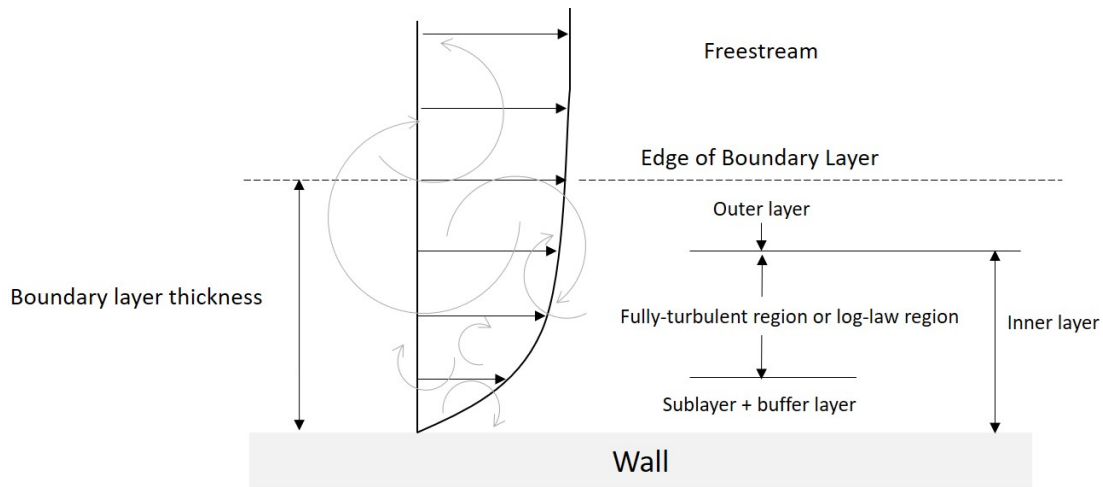


Figure 3.10 Turbulent inner layers of a flow

The Shear Stress Transport turbulence model is selected as the turbulence model of choice because of its versatility to capture both laminar and turbulent effects well as compared to some other models which can only be applied for turbulent flows. The Shear Stress Transport model is a low-Re turbulence model where the near-wall viscous sub-layer is solved numerically, hence a mesh with y^+ value of 1 is required, where y^+ is the non-dimensional distance from the wall to the first mesh node. Figure 3.11 shows a comparison between the y^+ of a high-Re model – which solves the logarithmic-based fully-turbulent region (log-law region) capturing only the turbulence effects near the wall but without the viscous effects at the wall; and the y^+ of a low-Re model – which solves for the viscous sublayer where turbulent effects near wall and viscous effects at the wall are both captured to provide more details.

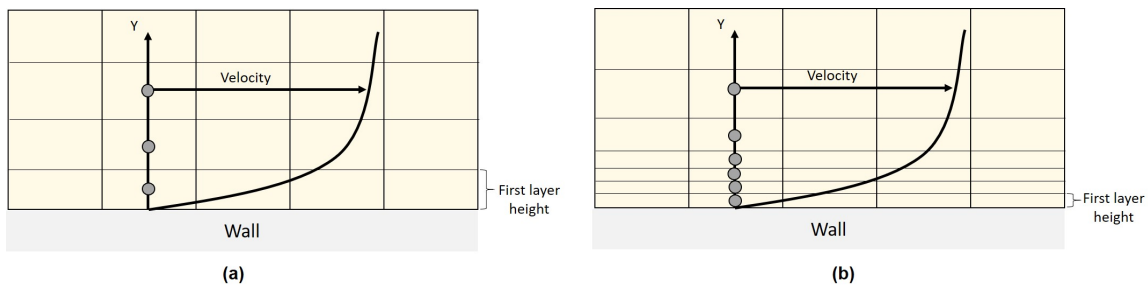


Figure 3.11 First layer height requirement of (a) high-Re and (b) low-Re turbulence models

The mesh was constructed with a first layer height of 0.045 mm, and a least 15 cell layers are maintained in the buffer layer ($y^+ < 30$) as shown in Figure 3.12.

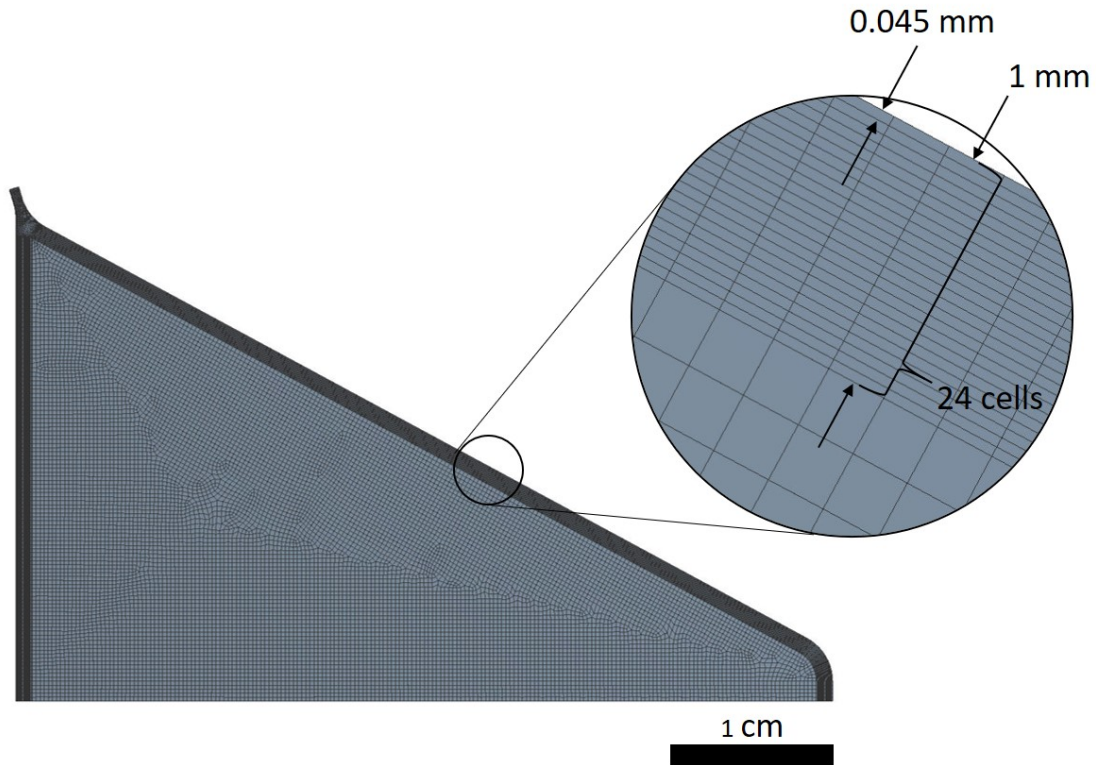


Figure 3.12 Structured mesh of the gradient channel with y^+ value of 1

Figure 3.13 shows the comparison of the velocity contour plot in the channel with the full laminar and Shear Stress Transport simulations. The velocities at the transition region are 5.7 m/s and 4.9 m/s for the laminar and SST simulations, respectively. However, the velocity quickly dissipates to 0.16 m/s within 2 cm of travel as the channel expand after the transition.

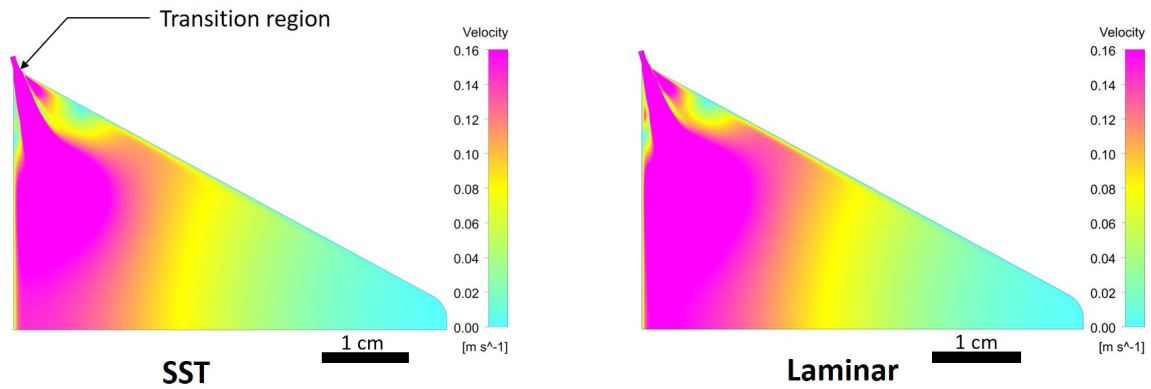


Figure 3.13 Flow velocity contour inside and at the outlet of the gradient channel, simulated (a) with the SST turbulence model and (b) without any turbulence model

Both simulations produce a similar velocity profile across the length of the outlet as indicated in Figure 3.14. The outlet velocity decreases from a maximum absolute velocity of 0.15 m/s on the left side of the reactor to 0 m/s on the right side. The velocity profile here is mostly driven by the vertical (y-axis) velocity component which is perpendicular to the channel outlet. The outlet velocity shows a reasonably linear variation in velocity especially in the central portion of the channel.

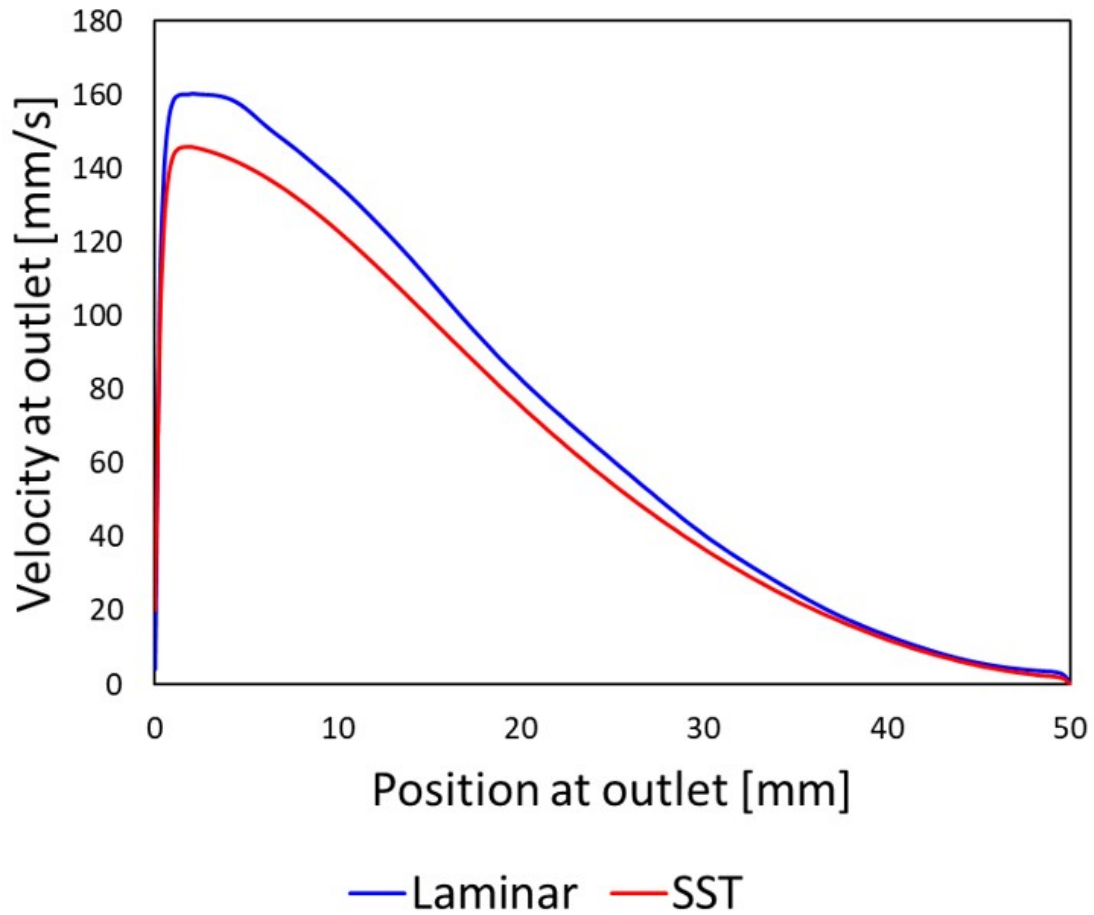


Figure 3.14 Vertical velocity profile at the outlet of the gradient channel based on (a) SST and (b) no turbulence model simulations

An additional CFD simulation was performed with a substrate placed 0.1 mm below the channel. Figure 3.15 shows the velocity contour of the flow outwards from channel parallel to the substrate surface.

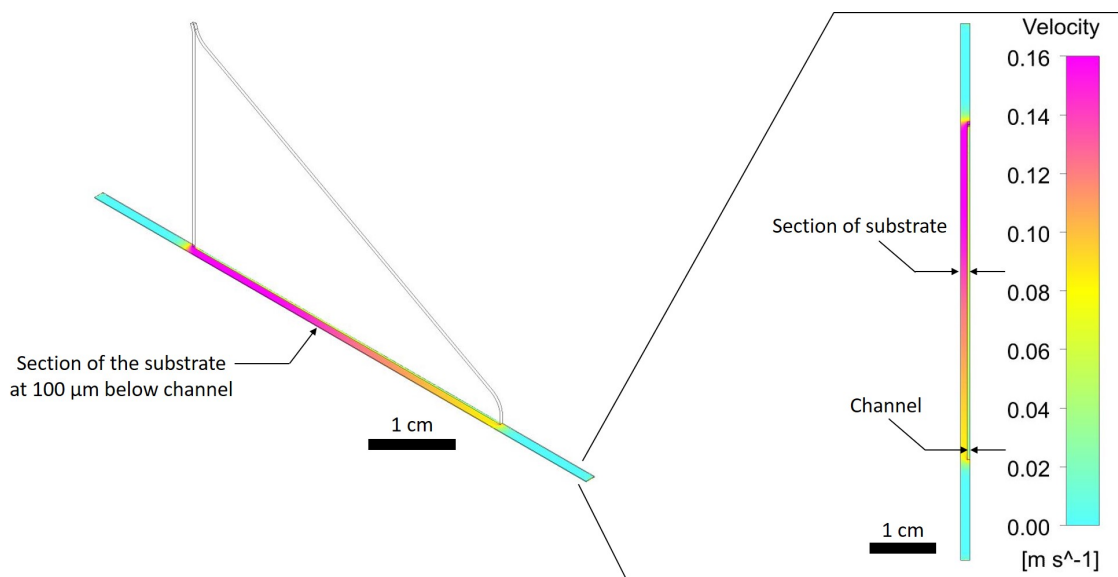


Figure 3.15 Velocity contour of the flow outwards from the gradient channel with a substrate placed 100 μm under

This is done to model the variation in precursor delivery to the surface of a substrate. Figure 3.16 shows the plots of the velocity components of the flow on the substrate surface along the length of the gradient channel. The CFD simulation reveals that the outlet flow now has a significant velocity component parallel to the substrate (x- and z-axis), as the vertical flow from the channel is re-directed horizontally into the space between the reactor and substrate. The CFD simulation shows that the horizontal velocity of the flow outwards from the right side of the gradient channel is not zero unlike the zero vertical flow velocity when no substrate is placed underneath. Notably, the horizontal velocity on the region of the substrate underneath the right side of the gradient channel is approximately half of that on the left side. This is attributed to the small reactor-substrate spacing, which squeezes the high flow rate from the left side outwards and redistributes the precursor to regions with lower flow rates. Nevertheless, the flow profile in the horizontal directions also shows a reasonably linear variation in velocity and hence corresponding to a gradient flow rate.

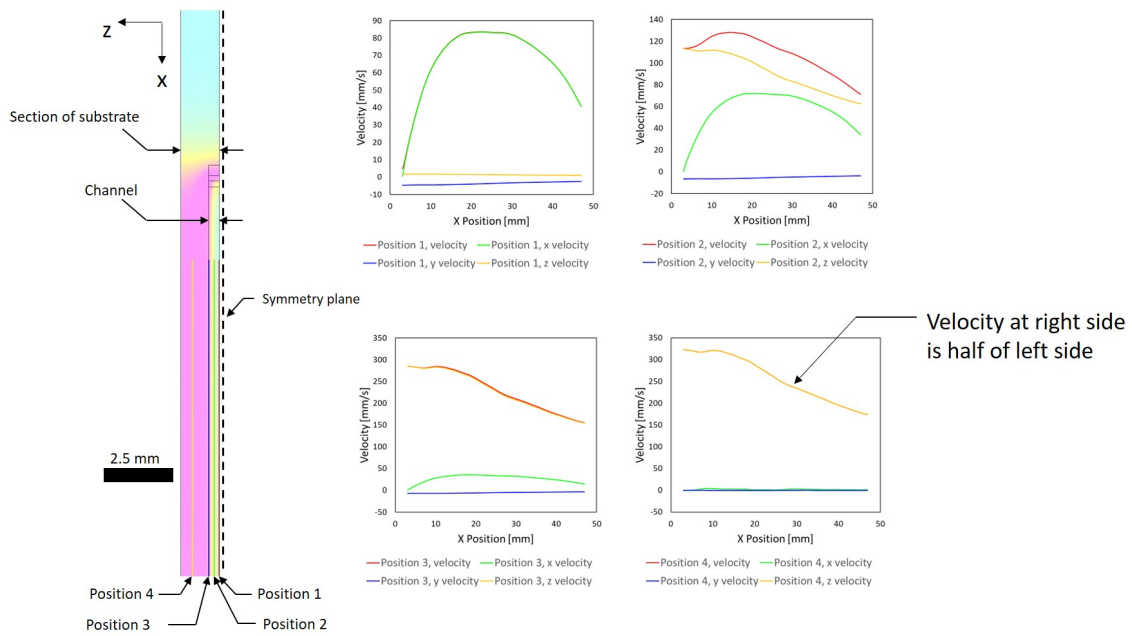


Figure 3.16 Plot of velocity components on different locations across the substrate surface

3.2.2 3D printing process and design considerations

When designing the reactor for SLA 3D printing, there are some important parameters to consider to ensure a successful print as well as a functional part is produced, they are:

- **Build volume of the printer**

The Formlabs Form 2 and Form 3 printer have a build volume of 145 x 145 x 175 mm³ and 145 x 145 x 185 mm³ respectively, which means the size of the reactor design must fit within this volume.

- **Appropriate resin type for the application and function**

Since the reactor head will be in close-proximity to a heated stage with surface temperature ranging anywhere from room temperature to 200 °C and potentially higher, the reactor head must be able to maintain its mechanical properties and geometry at elevated temperatures. Hence, a resin material that can withstand high temperature will be necessary. The Formlabs High Temp resin material is ideal for the application. When properly produced and processed, the part is expected to exhibit a heat deflection temperature of 238 °C according to Formlabs.

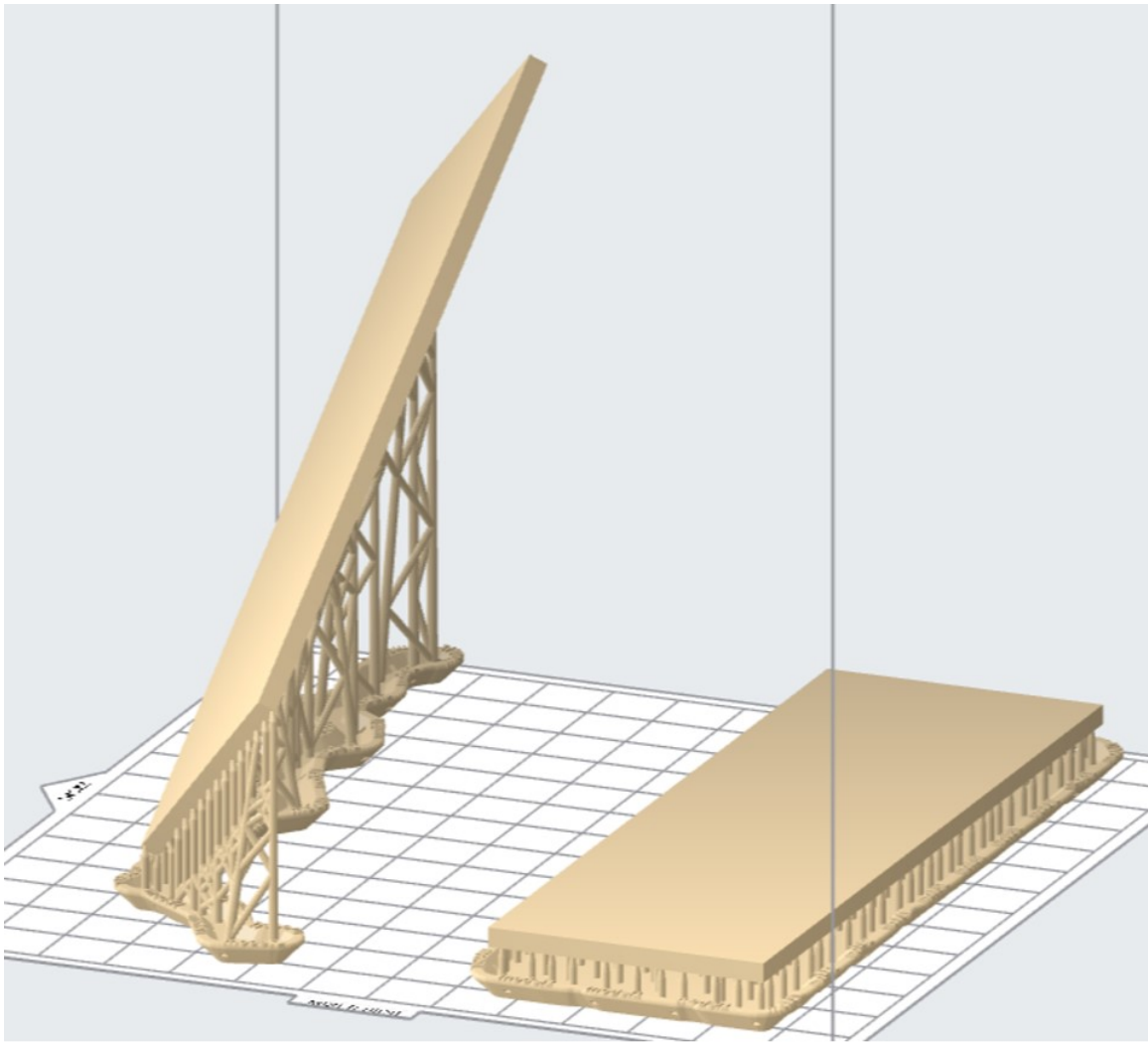
- **Minimum hole diameter and minimum distance between walls**

According to Formlabs Design Guide and the Formlabs community forum, a minimum hole feature diameter and minimum distance between walls of 0.5 mm is recommended. This is to make sure that the delicate features do not merge and close off during printing. The dimensional constraint is critical in guiding the decision of the channel width in which a width of smaller than 0.5 mm should be avoided.

- **Orientation of the print**

The orientation of a print is one of the most important process parameters in SLA that can directly affect the chance of success of the print as well as the functional properties of the produced part. Some examples of things to consider when orienting a part for printing includes how the uncured resin is drained, cross sectional area of each layer, critical features to preserve, number of minima sites.

When each cross-sectional layer is being cured and solidified by the laser source, there will be excess resin adhering to the layer and the solidified part. Given the viscous nature of the resin, the excess resin accumulates as the part is being built. Hence, it must be drained away from the part. When the part is oriented at an angle for the print, the excess resin build-up will be naturally be directed out from the part as it is being printed. Figure 3.17 is an example showing an identical rectangular piece being printed at an angle and flat.



(a)

(b)

Figure 3.17 Example of a part being printed (a) at an angle and (b) flat

It is better to print the part off itself without having to rely too much on printing on support structures. For example, if a part is being printed flat with a dense support structures under it, there may still be many regions where the part is not supported well, especially in between two support structures leaving the middle portion hanging. This may lead to the unsupported regions sagging, or leaving a cavity. Figure 3.18 is an example showing the support structures for the same rectangular piece when it is

oriented at an angle and when it is flat. Notably, the density of the support structure is lower when the part is oriented at an angle, because the part is mostly supported by itself (or printing off itself) rather than the support structures during the printing process.

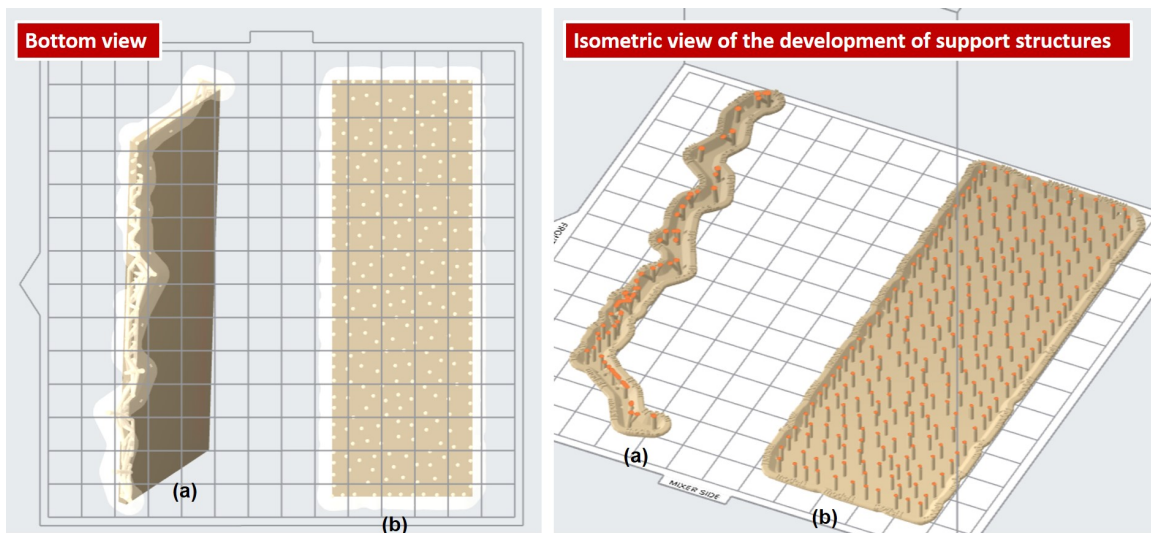


Figure 3.18 Support structures of an identical part being printed (a) at an angle and (b) flat

Printing the part off itself means that the subsequent layer is mostly built on top of the previous layer instead of being built mostly on support structures, which in some cases also reduces the number of supports needed. In addition, by printing the part off itself, it is also necessary to orient the part in a way that minimizes the cross-sectional area (Figure 3.19) of each layer to minimize the peeling force that occurs with each layer printed. The peeling force happens when the cured and solidified cross-sectional layer is lifted and separated from the bottom surface of the resin vat to prepare for the next layer. The larger the cross-sectional area, the higher the peel force, which affects the outcome and potentially distorts the geometry and dimensional inaccuracies. A larger peel force may also tear the part from the supports if the support structure is not strong enough. Furthermore, by minimizing the cross-sectional area, the degree of warpages reduces. As the liquid resin is cured and solidified, the transition tends

to shrink the part. Hence, the larger the cross-sectional area, the greater the shrinkage and consequently the more severe the warpages.

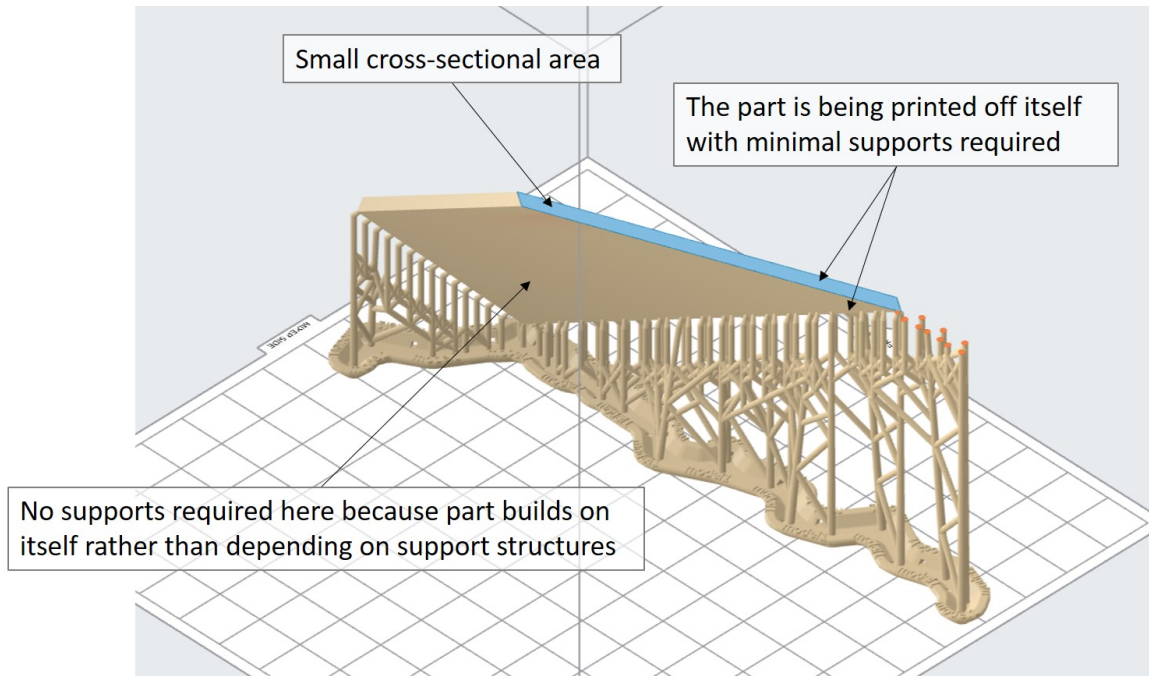


Figure 3.19 A sectioned print layer of the rectangular part oriented at an angle

Another aspect to consider is to define where the critical features are which require high dimensional accuracy and surface finish. Orient the part in a way that these critical features are facing away from the support structures. This ensures that the surface finish will be smooth and that no additional post processing is required (maintains dimensional accuracy).

Last but not least is to note the number of minima sites when orienting the print. Minima is the lowest point of a surface. Rotating a model to face the build platform from different angles helps to decrease the minima to as little and as small as possible for better prints.

A rule of thumb for orienting parts is to tilt the part 45° in both the X and Y axis to enforce small cross-sectional print layers.

- **Drain holes**

As described above, each layer is lifted after it is solidified, causing the peeling phenomena. However, if a part has a hollow or void in the design, it may create a cupping effect when the layer is being lifted – mimicking the suction effect with plungers and suction cups. Cupping happens when a previous print layer translates down until it touches the bottom of the resin vat and squeezes the resin out creating a low-pressure region. If the subsequent layer is hollow or a void, the low-pressure region can be severe. Once the layer is being lifted, the high suction force may disrupt the print and, in some cases, causes mini explosions damaging both the part and the printer. To mitigate the cupping issue, drain holes of at least 3.5 mm can be added to relieve the pressure. Another method is to orient the part in a way that avoids cupping.

- **Cure time and temperature**

Each resin material has an optimized curing time and temperature to set the part in its finalized form and mechanical properties. Printed SLA parts are typically washed in a bath of chemical agent such as isopropanol. Then the part will be placed in a curing chamber with ultraviolet lamps to finalize the part. However, it is important to note that the part will continue to cure under ultraviolet exposure even after it is set. SLA Resin printed parts, especially the ones fabricated using the High Temp resin, tends to be brittle. With continuous ultraviolet exposure, the part may overcure and crack. Nevertheless, before setting the part to cure, it must be noted that the part should be completely dried after washing with as isopropanol. If it is not fully dried, the isopropanol may be absorbed into the part and causes it to crack during curing. The recommended curing temperature and time for the High Temp V2 resin is 80°C for 120 minutes (not including additional oven baking step). Yet, curing the part at

such temperatures may cause the part to warp further as the internal stresses starts to take effect when the part gets slightly softer with heat.

- **Warpages**

Apart from orientation and curing techniques, warpages can be lessened with the right design considerations in mind. Generally, the key is to maintain uniform wall thickness throughout the design to prevent the internal stress mismatch between thicker and thinner areas. The mismatch of stresses may even lead to the part cracking as one area warps more than the other.

Furthermore, sometimes it may be beneficial to design the part with the warpages accounted for by designing the feature with an intentional warpage in the opposite direction to that of the predicted warpage.

- **Support structure**

There is a fine balance in terms of the support contact size and density for a desirable print result. The larger the support contact size, the stronger it is. Larger support contact provides more print stability since there will be lesser fluctuations when the layer is printed and lifted. However, removing the supports after printing will be harder and it may leave a larger mark on the surface. On the other hand, smaller support contact makes it a lot easier to remove the supports from the print and it tends to leave smaller marks which results in better surface finish which requires lesser post processing. Conversely, the trade off with smaller support contact is that it may necessitate a denser structure, and it risks stability issues.

Notably, when both larger and smaller support contacts are used in combination, lesser large marks on the surface can be expected and at the same time, dense support structure is no longer required, resulting in the best of both options.

A good way to strike a balance is to use larger support contacts around the border or edge of the part and use smaller support contacts everywhere else.

- **Residual resin**

Oftentimes after the print, there will be copious amount of residual resin everywhere internal and external of the part. In such instance, washing it in a bath of isopropanol may not be sufficient especially for internal geometries, for example reactor head channels.

For the case of reactor head channels, if the residual resin is not cleared, the network of channels may be clogged and render the part non-functional. Three methods have been found particularly useful, namely 1) using a small stationary utility knife to swipe across the channels to remove residual resin in channels, 2) use strong compressed air to blow into the channel inlets to force the residual resin out, 3) use isopropanol to wipe off the residual resin on the surface. Additionally, to examine if the channels are completely open, use a syringe filled with isopropanol dyed with food coloring and inject into the channel inlets to see the isopropanol pathway. It was found that a combination of all three methods had to be repeated multiple times to ensure that the channels are cleared of residual resin.

3.2.3 Film mapping

A simple code was developed in MATLAB to produce a visual map of the film based on a set of scattered data which is gathered by the user, namely the thicknesses (Z height) of the film at a certain specified position on the film (X, Y coordinates). The thickness of the film at certain location can be measured via reflectance spectroscopy with the use of a bifurcated reflectance probe connected to a UV-Visible spectrometer (Ocean Optix HDX)

and a light source (Ocean Optics DH 2000). The measurements are processed by fitting to the Tauc Lorentz reflectance model to obtain the thicknesses using a program developed by my colleague Kissan Mistry [47].

The operation is simple: the user can key in the thickness and its corresponding coordinate on the film one by one as prompted, or create arrays of the thicknesses and their corresponding coordinates, and then run the code to generate the map. Alternatively, the user can conveniently take thickness measurements and plot the map altogether, since the film mapping code is also tied in with the reflectance spectroscopy program.

The film mapping code uses the Delaunay triangulation which is then interpolated to create a triangular mesh from the scattered data points to generate the map. The triangulation portion of the code can be found in Appendix A.1. Figure 3.20 is an example of a mapped film along 20 mm (film length in x direction) and across 10 mm (film width in y direction).

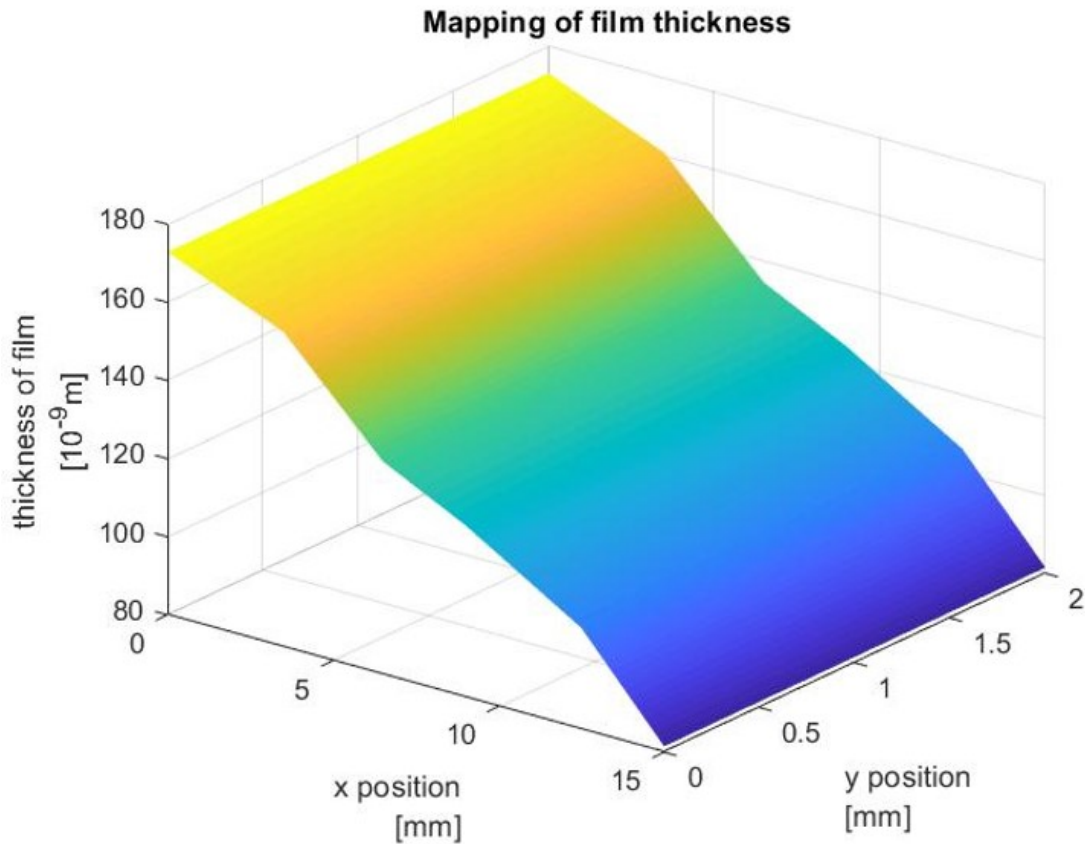


Figure 3.20 Example of a gradient film mapped using the film mapping code

Additionally, a manual XY translation jig was designed and constructed out of laser cut acrylic pieces to complement the film mapping code. The reflectance spectrometer probe is fixed in place above the substrate with the film to be measured. The jig consists of a substrate carrier which constraints the substrate to translate only in the Y direction (140 mm total). Likewise, the substrate carrier holding the substrate can be translated in the X direction (120 mm total). The translations in both directions are guided by the laser engraved measurements markings (1 mm increments) on the jig. This enables more accurate control of the position/coordinate at which the film thickness is measured. Figure 3.21 shows the 3D CAD model of the jig and a physical set up of the film thickness measurement system.

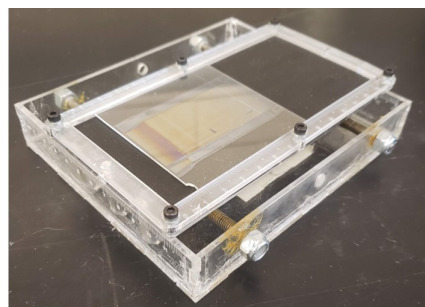
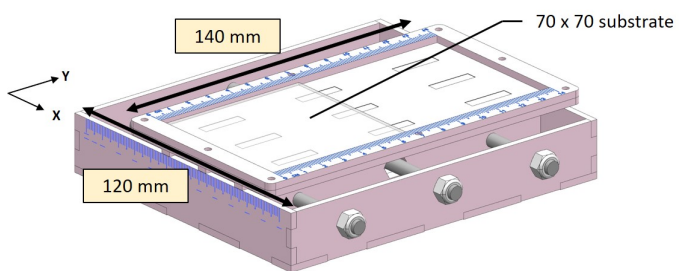


Figure 3.21 Film mapping rig

3.3 Results and Discussion

3.3.1 Design of customized reactor for multimodal deposition

The customized reactor is designed in such a way that it can be easily retrofitted to the existing lab-scale AP-SALD system, notably it includes the same mounting locations as those on the metal reactor. Figure 3.22 shows a 3D printed reactor retrofitted into the lab AP-SALD system.

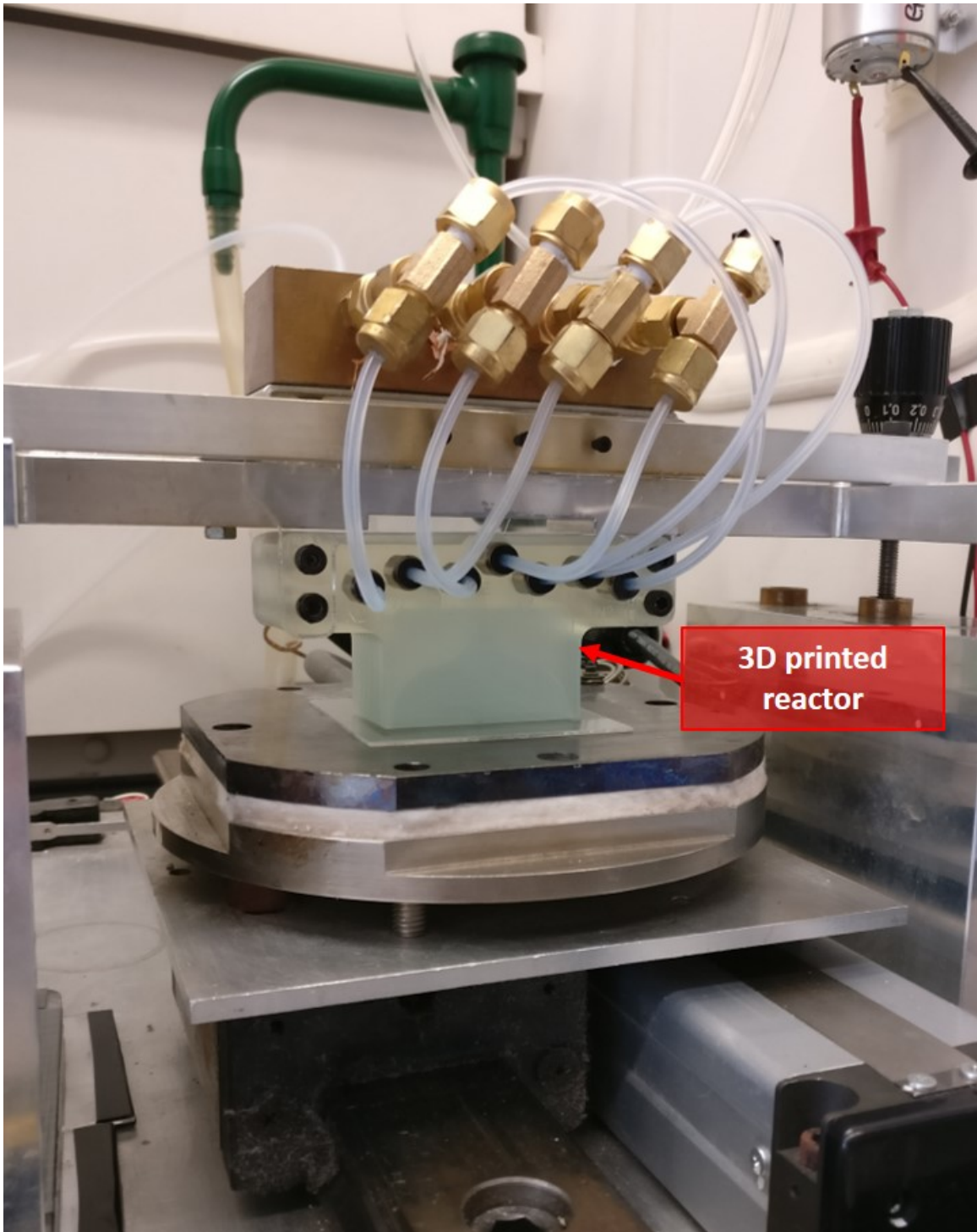


Figure 3.22 A 3D printed reactor installed into Dr. Musselman's lab-scale AP-SALD system

The dimensions of the internal network of inner distribution channels are defined based on the constraints discussed in Section 3.2, where the height of the channel is chosen to be

at least 30 mm (based on CFD results to achieve fully developed flow regime), and that the minimum distance between walls must be at least 0.5 mm (to avoid the channels from closing off during SLA 3D printing).

As described in the Chapter Overview (Chapter 3.1), the reactor is designed with the intent to produce films with thickness gradient while maintaining a fixed gap spacing across the reactor and the substrate. With the metal reactor, it is possible to examine if the reactor is leveled in parallel to the substrate by visually inspecting the film it deposits. When the reactor is leveled in parallel to the substrate, a uniformly thick film will be produced. However, if the customized reactor design only includes a precursor channel for producing films with thickness gradient, there will be no way to inspect with certainty if it is leveled parallel to the substrate. Hence, a mechanism to inspect the parallelism is required be built into the reactor design.

After designing, 3D printing and testing a few concepts, it was found that the best solution is to incorporate an additional precursor channel that is meant for depositing uniform films. Such a design has the benefit of enabling multimodal deposition options, namely producing films with uniform or graded thicknesses. The uniform channel is used to deposit a uniform film before switching the precursor flow to the gradient channel. This ensures that the reactor-substrate spacing is uniform and that any gradients produced are defined by the design of the gradient channel and not due to unintended tilting of the reactor. When depositing with either of the precursor channels, we flow inert gas through the channel that was not in use to prevent precursor or reactant gas from entering the unused channel. Figure 3.23 shows the internal network of channels in the customized reactor design.

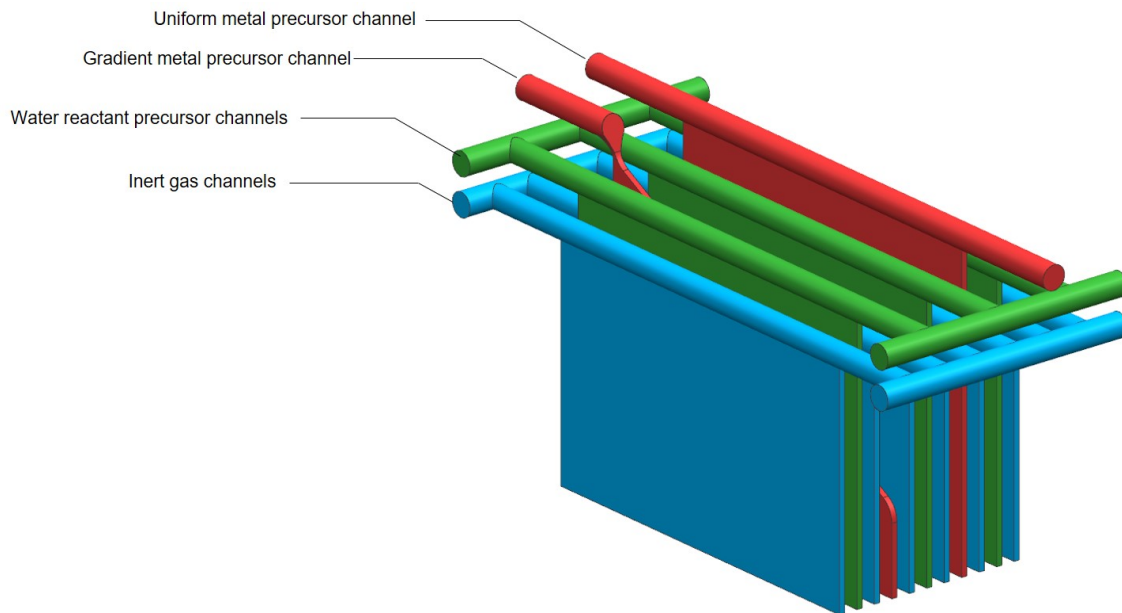


Figure 3.23 Internal network of gas distribution channels in the customized reactor design

Once the design of the internal channels is defined, the next step involves designing the reactor for 3D printing, as shown in Figure 3.24.

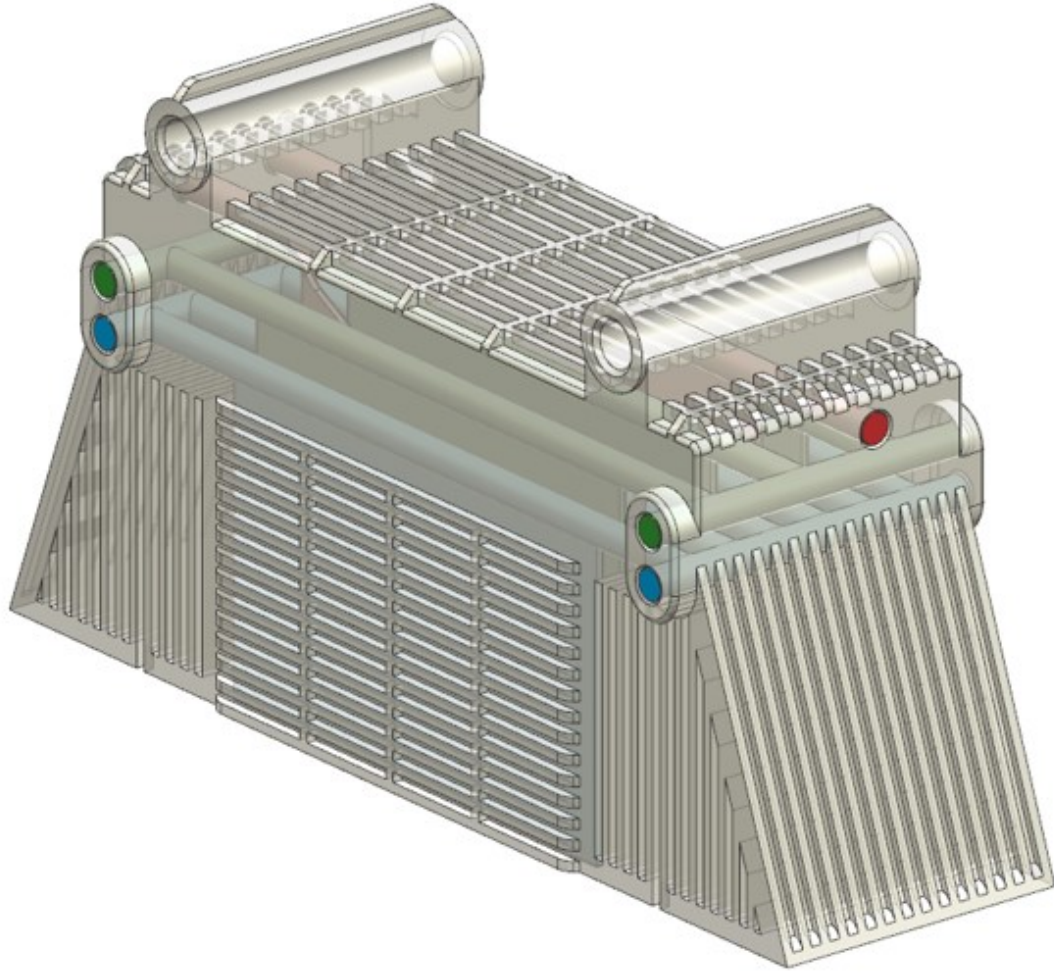


Figure 3.24 Custom reactor design

Figure 3.25 shows the printing orientation in Formlabs' PreForm slicer software for a successful print as well as the actual physical product of the print.

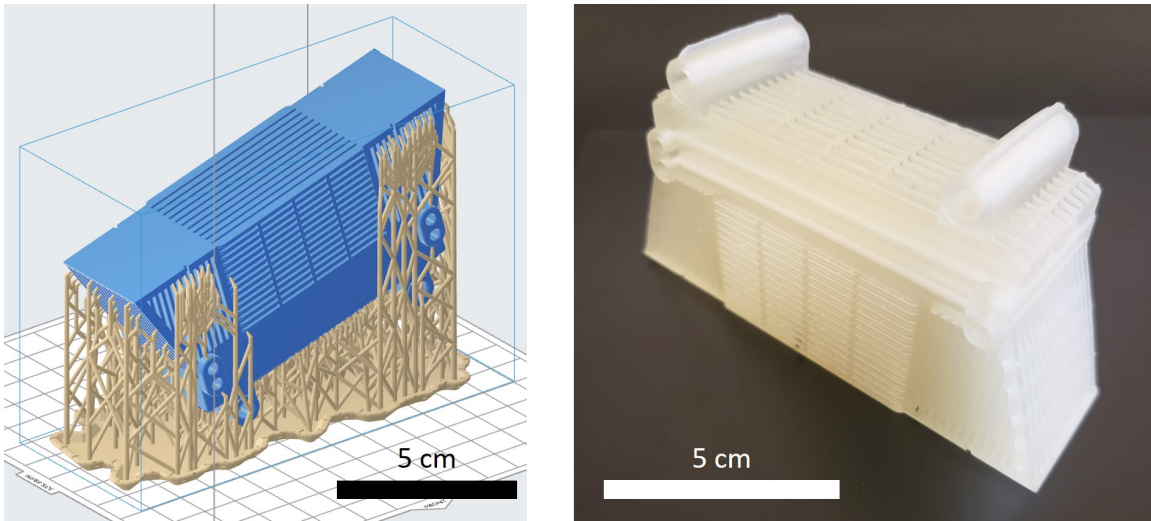


Figure 3.25 Preparation of customized reactor design using Formlabs' PreForm slicer software and photo of the 3D printed reactor

3.3.2 Uniform and gradient film thickness measurements

The reactor was used to produce zinc oxide films with uniform thickness and graded thickness. Figure 3.26 shows a film with a uniform thickness deposited on $70 \times 70 \text{ mm}^2$ borosilicate glass.

For the deposition of the film, nitrogen gas was bubbled through a diethylzinc precursor at 45 sccm and combined with a 127 sccm nitrogen carrier flow. Water was bubbled at 68 sccm and combined with a 382 sccm nitrogen carrier flow. A 900 sccm nitrogen curtain was used to partially separate the precursors and remove excess unreacted precursors or by-products. A reactor-substrate spacing of $200 \mu\text{m}$ was used. The substrate was heated to $100 \text{ }^\circ\text{C}$ and oscillated at a speed of 15 mm/s for 150 (27 mm) cycles. The film thickness was measured across the substrate using reflectance spectroscopy. The film indicated a thickness of 178 nm , a growth per cycle (GPC) of 1.19 nm/cycle (0.66 nm/s) with uniformity of $\pm 5\%$. Furthermore, the film was measured to have a band gap value of 3.19 eV , consistent with that previously reported for zinc oxide [47].

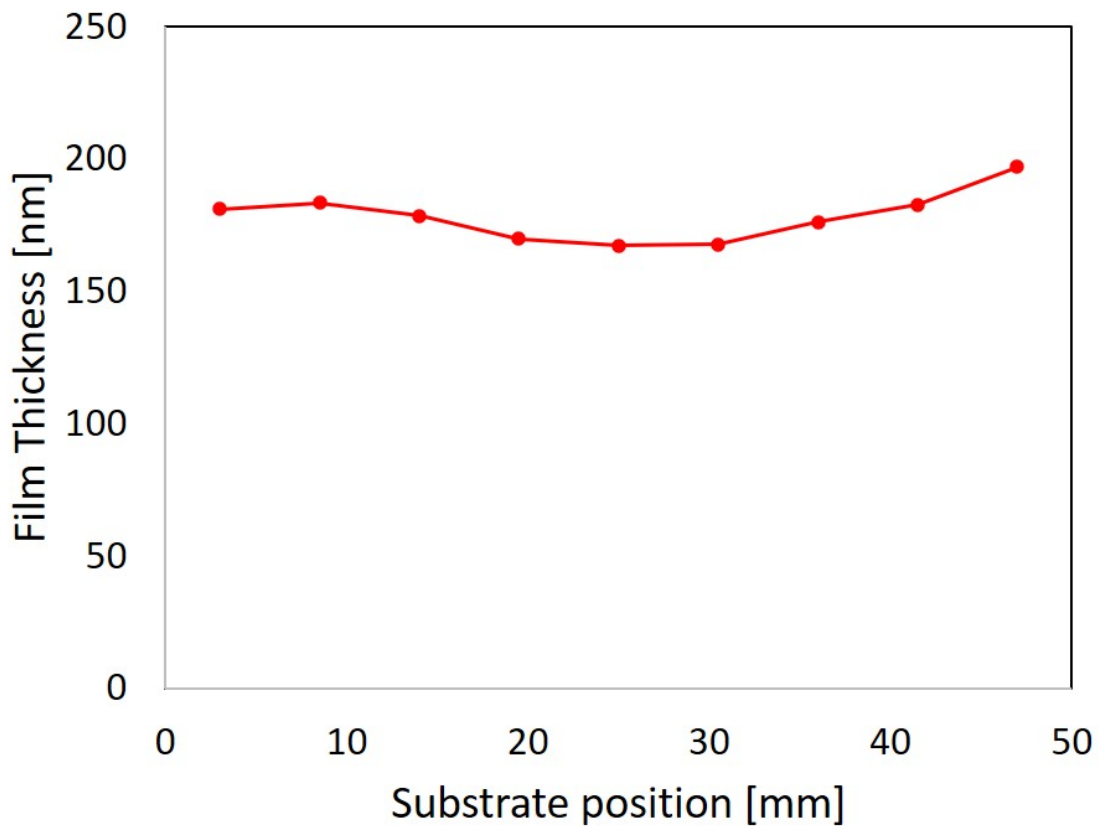
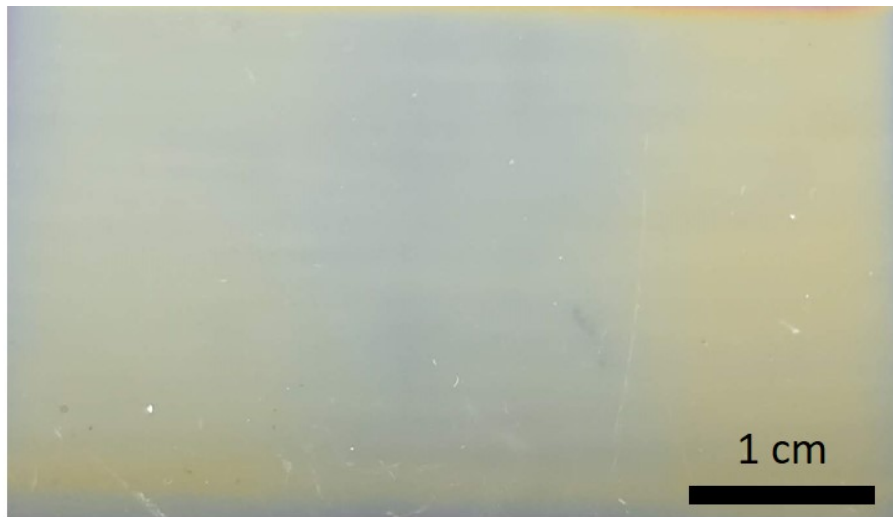


Figure 3.26 Uniform film produced via the printed reactor using the uniform channel

Figure 3.27 shows a film with a thickness gradient deposited on 70 x 70 mm² borosilicate glass. Here, nitrogen gas was bubbled through the diethylzinc precursor at 20 sccm and combined with a 50 sccm nitrogen carrier flow. Water was bubbled at 32 sccm and

combined with a 179 sccm nitrogen carrier flow. A 560 sccm nitrogen curtain was used. A reactor-substrate spacing of 100 μm was used. The substrate was heated to 100 $^{\circ}\text{C}$ and oscillated at a speed of 30 mm/s for 500 (27 mm) cycles. The measured thicknesses indicated a GPC of 0.30 nm/cycle (0.33 nm/s) on the side with higher flow rates (left side) and 0.17 nm/cycle (0.19 nm/s) on the side with lower flow rates (right side). The GPC on the left side is approximately double of than on the right side. Notably, the variation in GPC was consistent with the simulated variation in flow velocity in Figure 3.16 in Chapter 3.2.1. However, more experiments and studies will be required to corroborate this comparison.

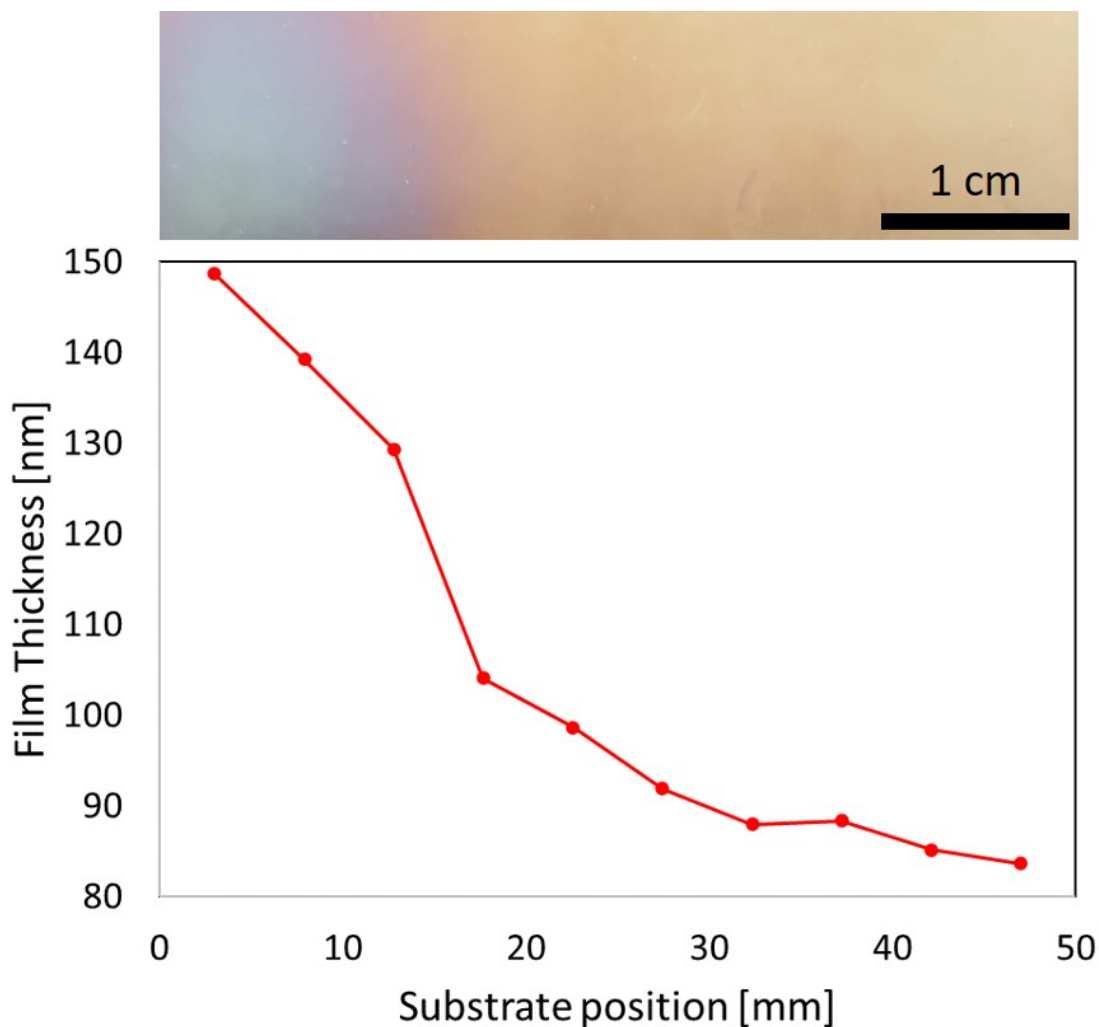


Figure 3.27 Gradient film produced via the printed reactor using the gradient channel

3.4 Conclusion

In conclusion, the concept of a customized gradient reactor was designed and tested to demonstrate the ability to deposit films with thickness gradients using a fixed reactor-substrate spacing. CFD modeling was used to guide the design of the reactor, particularly the geometry of the channels inside the reactor. Furthermore, SLA 3D printing design guidelines were adopted to help define some of the key dimensional constraints on the reactor design.

The customized reactor was designed in such a way that enables multimodal depositions for producing films with uniform and graded thicknesses. The sophisticated internal network of channels cannot be fabricated by traditional machining means, and hence SLA 3D printing was selected as the method of choice to realize the design. The customized reactor design was 3D printed and tested to produce both the types of films mentioned. Notably, the gradient film that was produced indicated growth rates that are consistent with the CFD simulated variation in flow velocity. However, more experiments and studies are still required to confirm the comparison.

Chapter 4

Heated stage and 3D printed reactor for pilot-scale AP-SALD

4.1 Chapter overview

As the lab-scale AP-SALD system has already been demonstrated, a key next step is to scale it up to a pilot-scale system that reflects its viability in the commercial space. However, there are not many commercial spatial ALD, let alone AP-SALD systems currently available as discussed in Chapter 2. Hence, there is a need to design, build and test one to validate its scalability and accelerate its development for large scale high throughput manufacturing.

Chapter 4.2 discusses primarily the analysis, simulation, design considerations and construction of a heated stage that holds substrates with suction for the commercial-scale system at the University of Waterloo. It will also describe the design and 3D print of a unique reactor design for the system, which aims to isolate the precursor gases more effectively by making it less sensitive to gap spacing.

Chapter 4.3 presents the results and discussions of the performance of the substrate stage, particularly the effectiveness of the suction design and the stage heating. The heating performance will also be compared with the simulated results. The chapter will also present the experimental results of the films produced using the novel 3D printed reactor design.

4.2 Experimental Design

4.2.1 Substrate stage requirements

The main requirements that were considered when designing the substrate stage for the pilot-scale system are:

- **Surface of the substrate stage can be heated up to 300 °C**

The temperature required for AP-SALD varies from approximately 50-300 °C based on the ALD window. Hence, the surface of the substrate stage should have the capacity to heat the substrate up to 300 °C to facilitate the thermal ALD reaction on the substrate surface. Figure 4.1 is a depiction of the ALD window.

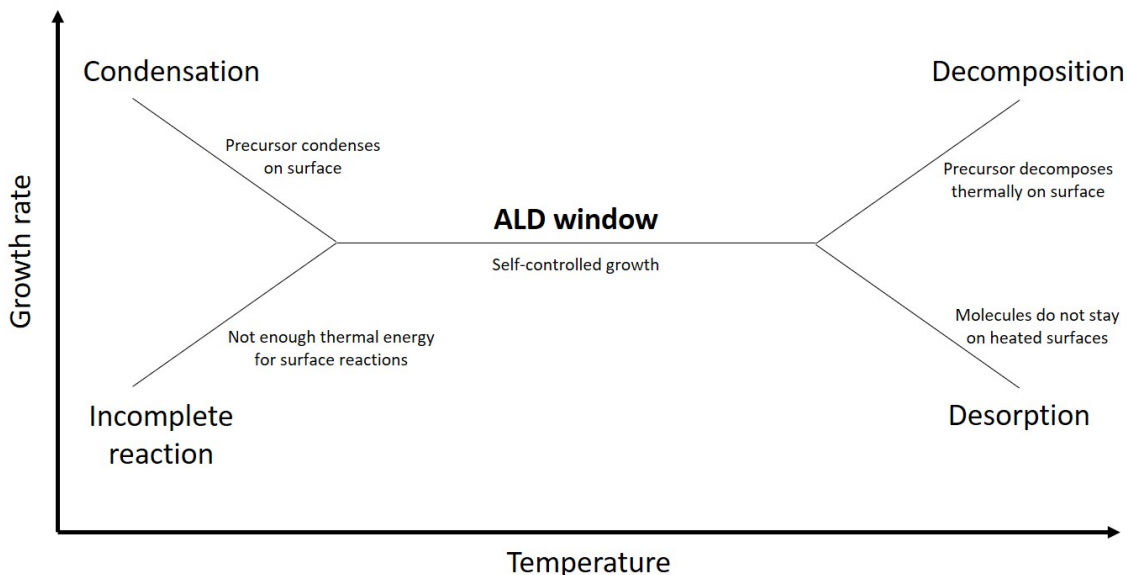


Figure 4.1 ALD window

- **Stage should be heated to user defined temperatures within 10 minutes**

The stage should be heated up in as short amount a time as possible to reflect the time constraints aspect in the industry and manufacturing plants. The 10-minute target is

an arbitrary target to guide the sizing of the heating element and design of the stage. The stage will then be tested to verify if the method of sizing the heating element and the design of the stage work as expected (i.e. heat up to desired temperature within 10 minutes).

- **Stage material should be thermally conductive**

To ensure good heat transfer within the substrate stage and to the substrate, thermally conductive material should be used for the stage design.

- **Surface of substrate stage should be uniformly heated**

To ensure that the substrates are uniformly heated to minimize the variation of deposition growth rates across the substrates.

- **Surface of the substrate stage should remain flat when heated**

Since the gap spacing between the reactor and the substrate is small, any variation in the flatness may impact the film deposition. Such adverse effects include the substrate clashing into the reactor, difficulty in controlling the gap spacing, and uneven or non-uniform deposition on the substrate.

- **Stage material should remain flat during machining**

The machining process of a flat piece of material may lead to distortions and warpages due to the residual stress introduced. Material selection is key in making sure the stage remains as flat as possible when it is undergoing the fabrication process.

- **Stage material should be sufficiently light for motion requirement**

The oscillation speed and frequency of the linear stage is sensitive to the mass of the load it bears, in this case the substrate stage. The lighter the load, the faster the linear stage can oscillate. Faster oscillation also leads to higher throughput, which is desired for demonstrating the efficacy of the pilot-scale system.

- **Substrates should be firmly and securely held in place during deposition**

Being able to firmly hold the substrate in place helps to ensure better quality films by preventing mini movements from the high oscillating speeds during deposition. Furthermore, it is required to securely hold the substrate in place to prevent catastrophic failures such as the substrate flying off from the substrate stage with high speeds, colliding with other objects and breaking. Such a catastrophe not only damages the system and its components, it is also a potential source of harm to humans.

- **Stage should be able to hold multiple substrates**

The pilot-scale system should be designed with the intent to prove that the technology is suitable for large-scale high throughput production. One way to increase the throughput is by increasing the number of substrates the stage can hold, so that the process can deposit on more than one substrate per cycle.

4.2.2 Substrate stage design

Based on the requirements, an initial idea of a lightweight, heated substrate stage with suction chucks that hold four 150 x 150 mm² substrates was conceptualized. When designing the stage, there was no obvious process which could be followed. Rather, the design was iterated and guided by dimensional constraints (e.g. heating element and O-rings), weight constraint (ideally below 20 kg), suction area required, heating power required, and such; all of which depended on each other and hence had to be designed cohesively. With that in mind, this section will not serve as a step-by-step guide of the substrate stage design, instead it discusses the rationale behind material and component selections, the design of suction chucks, the design of the heating element, heating power budgeting calculations and simulations.

- **Overall substrate stage design and construction**

The main components of the stage include four machined aluminum pieces, combined with 18 stainless-steel tubes. Essentially, the four machined aluminum pieces are split into two at the top and two at the bottom. The top assembly sandwiches a 8 mm diameter tubular heating element in between to generate the required heating. The bottom assembly is clamped with a thin layer of high temperature RTV silicone gasket to ensure sufficient seal, creating a suction reservoir. The stainless-steel tubes connect the suction reservoir to the top assembly where the substrates are held down, by the suction through these tubes. MIC6 cast aluminum was selected as the material of choice for the four pieces because it is machinable and remains relatively flat during the machining process, it is inexpensive, lightweight (at least three times lighter than copper and steel) and it has good thermal conductivity (second most conductive among common metals after copper). The piece on which the substrate sits on was electroplated with 6 to 8 microns of nickel plating as a protective layer to prevent direct deposition from the reactor to the aluminum underlayer. Conversely, stainless-steel is chosen as the material for the tubes because of its low thermal conductivity to inhibit as much heat transfer from the top assembly to the bottom assembly as possible, while at the same time providing structural strength. The entire stage is $600 \times 400 \times 43$ mm³ and weighs slightly under 20 kg. Figure 4.2 is a cross section of the substrate stage design.

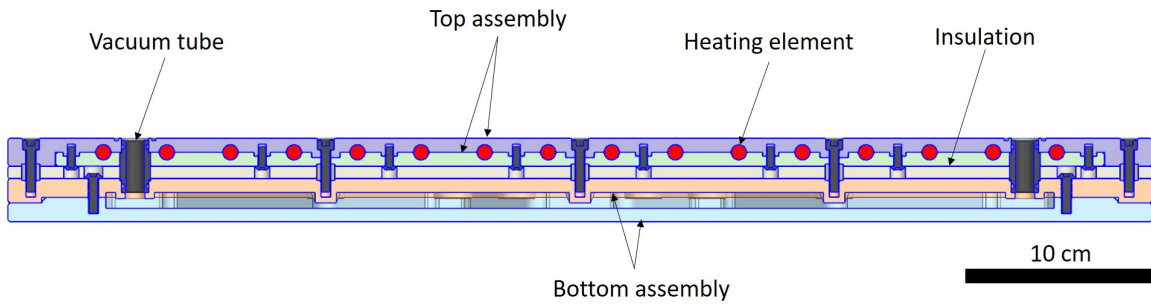


Figure 4.2 Cross section of the substrate stage design

Figure 4.3 shows the physical substrate stage installed on the pilot-scale AP-SALD system.

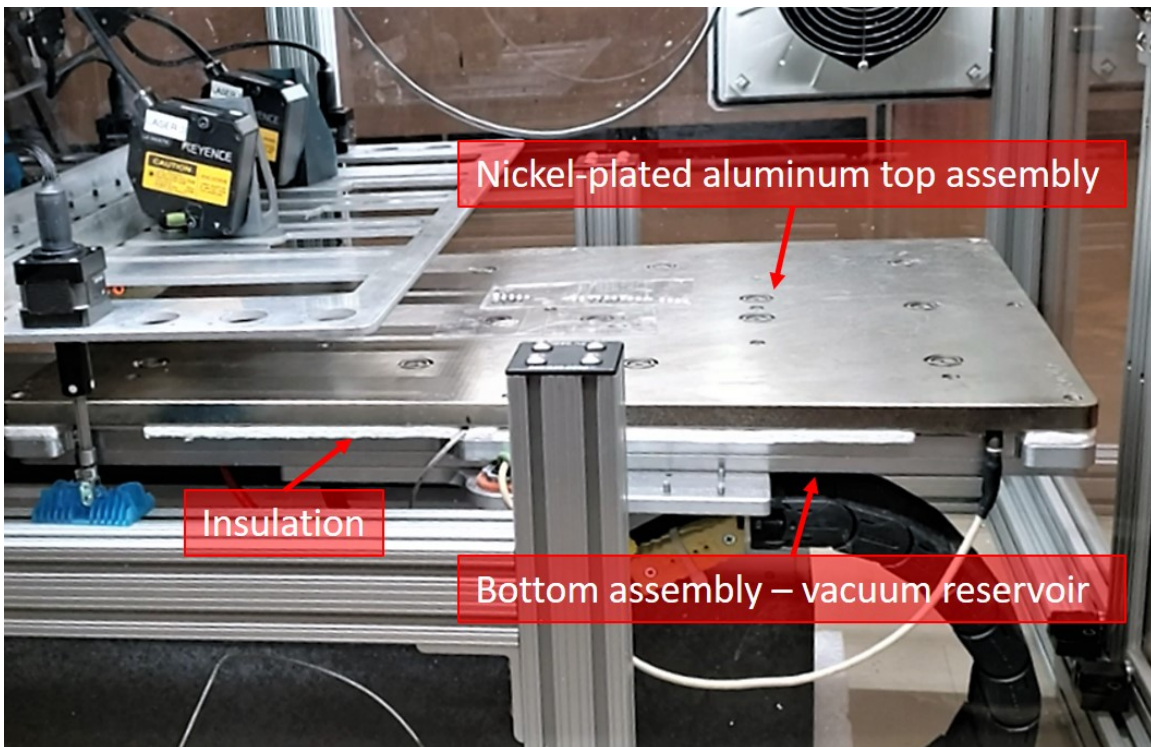


Figure 4.3 Photo of the physical substrate stage installed into the pilot-scale AP-SALD system. Adapted with permission from Chee Hau Teoh.

The heating element grooves are designed in such a way that either one full heating element or up to three separate heating elements can be embedded into the top assembly. The advantage of having three separate heating elements is that they create

three unique heating zones which can vary the deposition rate across the substrates, for combinatorial studies. Figure 4.4 shows the heating element design inside into the top assembly and the potential for three separate heating zones.

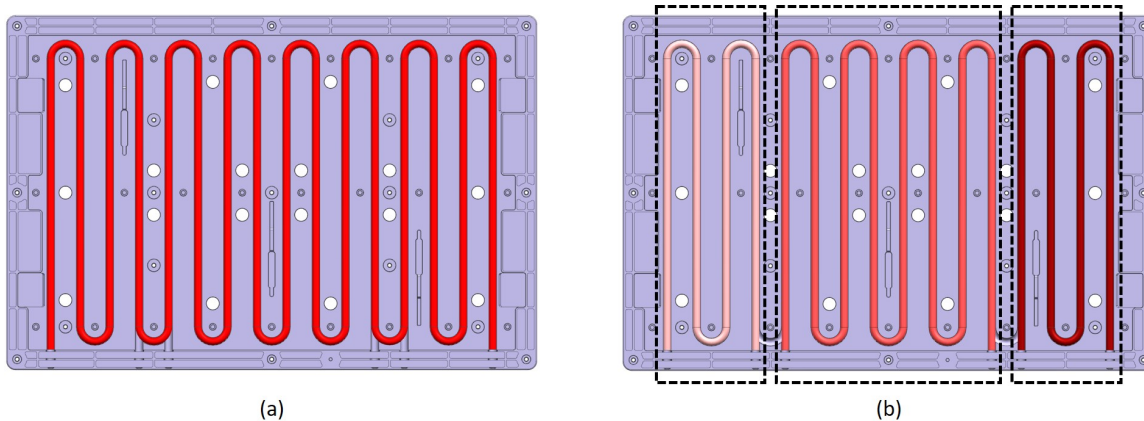


Figure 4.4 Heating element design for the top assembly

Figure 4.5 shows one heating element installed into the substrate stage.

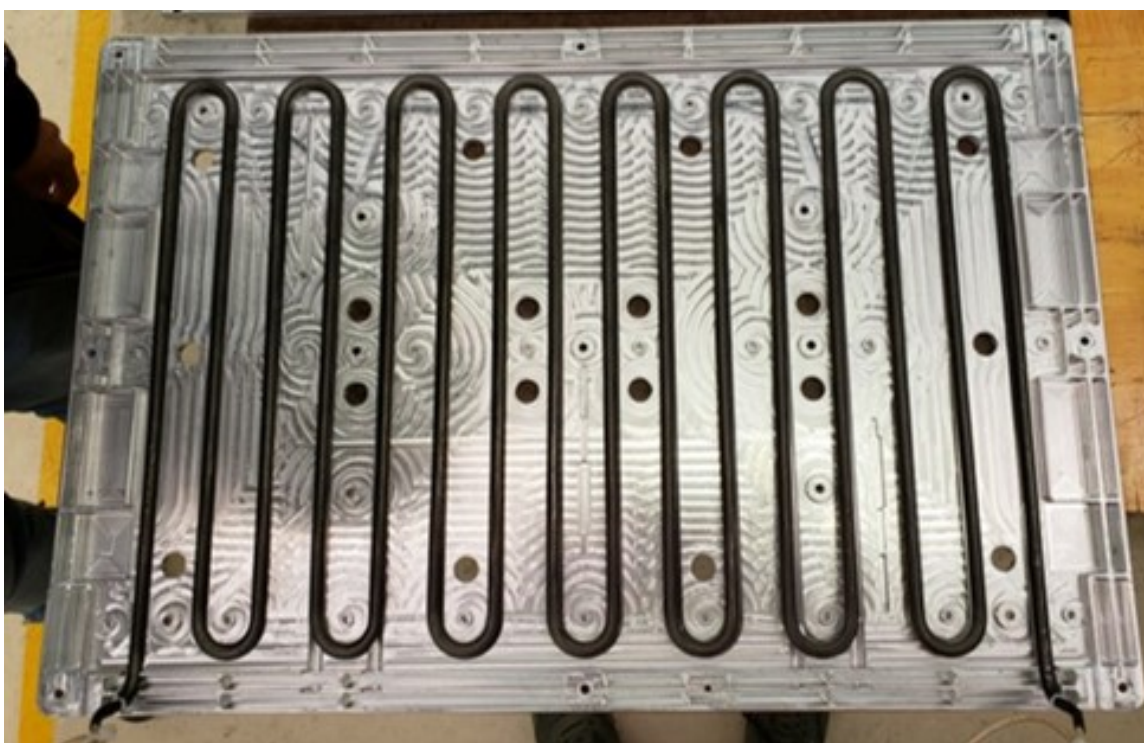


Figure 4.5 Photo of the physical heating element being fitted into the top assembly

- **Heating power budgeting**

The heating power budgeting involves analyzing three main aspects, namely:

1. Power required to heat the top assembly of the stage up to a user defined temperature (i.e. 300 °C) within 10 minutes when the stage is idle (i.e. during start up)
2. Power required to compensate for heat loss from the top assembly of the stage during idle mode
3. Power required to compensate for heat loss from the top assembly of the stage when it is oscillating

A heating power budgeting calculation tool was developed in Microsoft Excel. All of the formulae in the Excel worksheet are adapted from or derived based on the formulae found in the book Fundamentals of Heat and Mass Transfer [2].

The main goal of the tool is to compute the appropriate power density (or Watt density) and provide relevant information for fine tuning the stage design as well as making informed decisions, especially with the sizing of the heating element. The tool includes seven linked worksheets, which also attempts to compare the performance and power requirement of two stage materials (aluminum and copper); as follows (snapshots of the sheets can be found in Appendix B.1):

1. “Geometry” – where the user enters relevant geometrical dimensions of the stage, such as thickness, volume, surface area, and so on, for the thermal analysis in other worksheets.
2. “Interpolator” – where the user can easily obtain the interpolated thermophysical properties of air (based on published tabulated data) by entering a desired

temperature. The interpolated data is then entered and used in the “Iterative solver” sheet.

3. “Material properties” – where the user enters relevant thermophysical properties of all materials involved (i.e. aluminum, copper, borosilicate glass) and substances (i.e. air) used for the thermal analysis
4. “Iterative solver” – where the user can estimate the surface temperatures at the four side faces of the stage by entering an initial guess value. The sheet then iterates and converges the side temperatures to a more realistic value. The derivation of the iterative functions is detailed in Appendix B.2.
5. “Total heat loss (idle)” – with the values entered by the user in the first four sheets, this sheet calculates the heat transfer coefficients of the relevant heat transfer modes which are used to compute the total heat loss from the stage during idle mode.

The heat loss being calculated includes the natural convection from all sides including the top surface of the stage, the conduction heat loss from the ends of the serpentine heating elements to the four sides of the stage, the conduction heat loss from the top of the fasteners and the suction tubes to the bottom which is cooler (in contact with the bottom assembly), and the heat loss due to radiation. All computed heat loss values are combined to derive the total heat loss when the stage is idle. Figure 4.6 shows the heat transfer modes of the top assembly when it is idle.

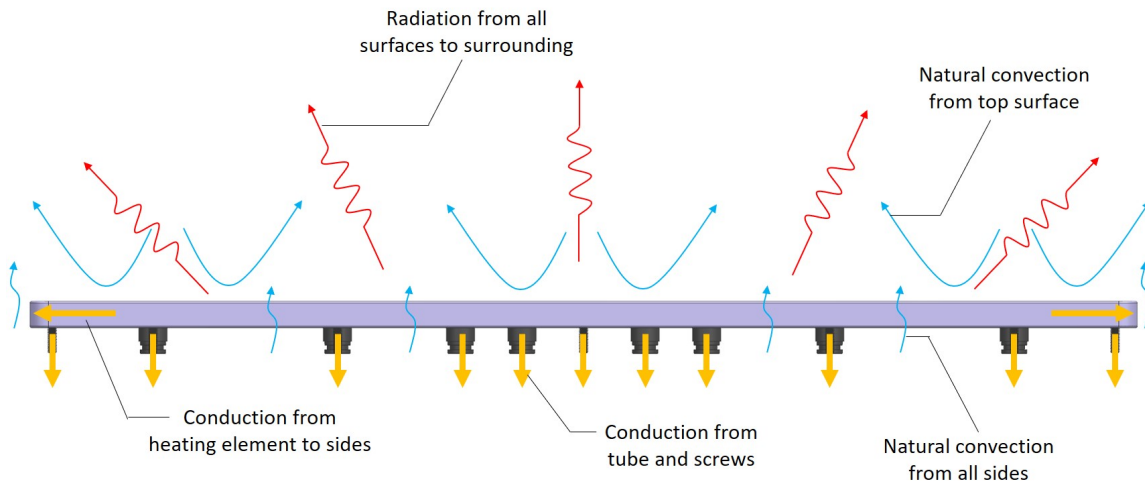


Figure 4.6 Heating modes of the top assembly during idle

6. “Total heat loss (operation)” – this sheet calculates the heat loss due to forced convection on the sides and the top surface when the stage is oscillating. The only data that the user enters is the oscillation speed of the stage. The computed heat loss due to forced convection is combined with the heat losses due to conduction (i.e. to sides, and from top to bottom of the screws and tubes), and radiation to derive the total heat loss when the stage is oscillating.
7. “Power needed to heat up stage” – where the user enters the desired top surface temperature value and the time required. This sheet calculates the power needed to achieve the user defined target (with and without heat losses). It also includes the power required to maintain surface temperature, which effectively is equivalent to the total heat loss (idle/operation whichever is higher). Most importantly, this sheet calculates the Watt density to meet the heating power requirement. It must be noted that the sizing (diameter and power ratings) and design of the heating element are presumed to first calculate the heating power required.

Based on the tool, a heating element with a Watt density of 4.77 W/cm^2 and heating

power of 6.3 kW should be used to heat the stage surface up to 300 °C within 10 minutes (2.28 W/cm² and 3.0 kW to maintain it at 300 °C). In the end however, a heating element with Watt density of 1.11 W/cm² and heating power of 2.8 kW was sized using the tool, and was installed into the stage, in part because the foreseeable deposition temperatures mostly fall within 200 °C for initial testing of the system.

- **Substrate stage heating simulation**

In addition to the power budgeting calculations, heat and buckling simulations were carried out in ANSYS. The heat simulation is used to create a predicted temperature map across the stage surface to examine the temperature distribution especially on the areas covered by the four substrates. The heat flux and heat transfer coefficients (thermal conductivity, convection, radiation) from the power budgeting calculations were used in the simulation. Heat mapping is necessary to make informed design decisions to minimize the temperature variations that could affect the uniformity of the deposition. Figure 4.7 shows the generated heat map of the top assembly with the heating element sized for 300 °C, the heat transfer coefficients as per the values derived from the heating power budgeting tool, and 25 °C ambient air temperature. The simulation indicated a temperature delta of 10 °C from the hottest to the coldest regions ($\pm 3.33\%$) in the areas covered by the four substrates.

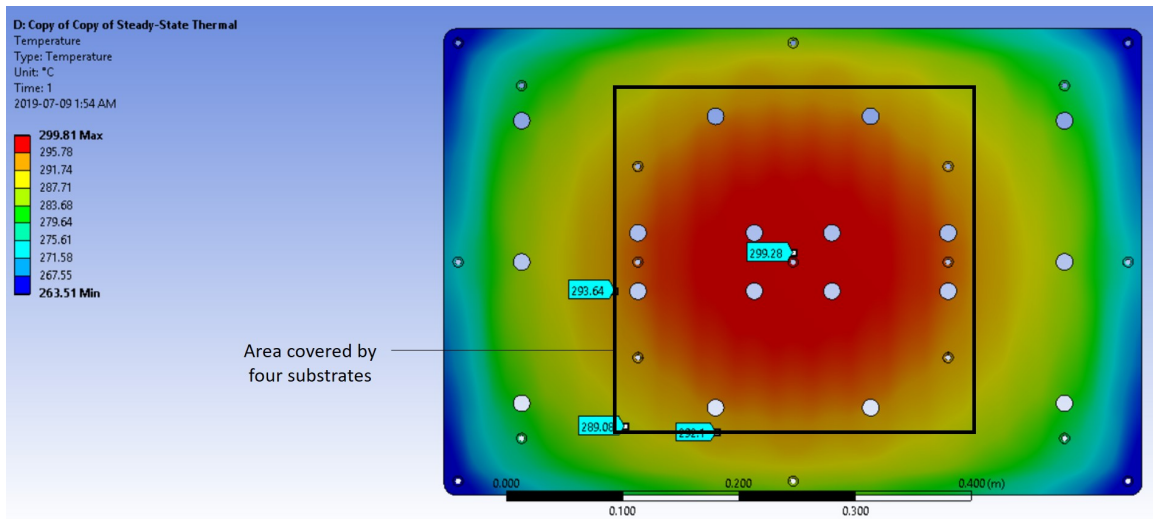


Figure 4.7 Thermal simulation of the top assembly

Based on the simulated results, a map of heat buckling was also generated to identify regions with exceptionally severe buckling displacements. Since the AP-SALD uses a close-proximity approach, where gap spacing is ideally kept as small as possible, any large buckling displacements on the stage may risk clashing into the reactor. The buckling displacements were measured relative to the centre region of the stage where the four substrates are placed, since that is where deposition mostly occurs. Variations in the buckling displacements on the areas covered by the substrates may cause unintended tilting relative to the reactor, which results in potential non-uniformity in depositions. The heat buckling analysis is thus useful in guiding the design, especially in determining the appropriate fastener locations to minimize overall buckling displacements. Figure 4.8 shows the buckling displacement map of the top assembly, which indicated a buckling displacement variation of 0.2 mm at the areas covered by the substrates.

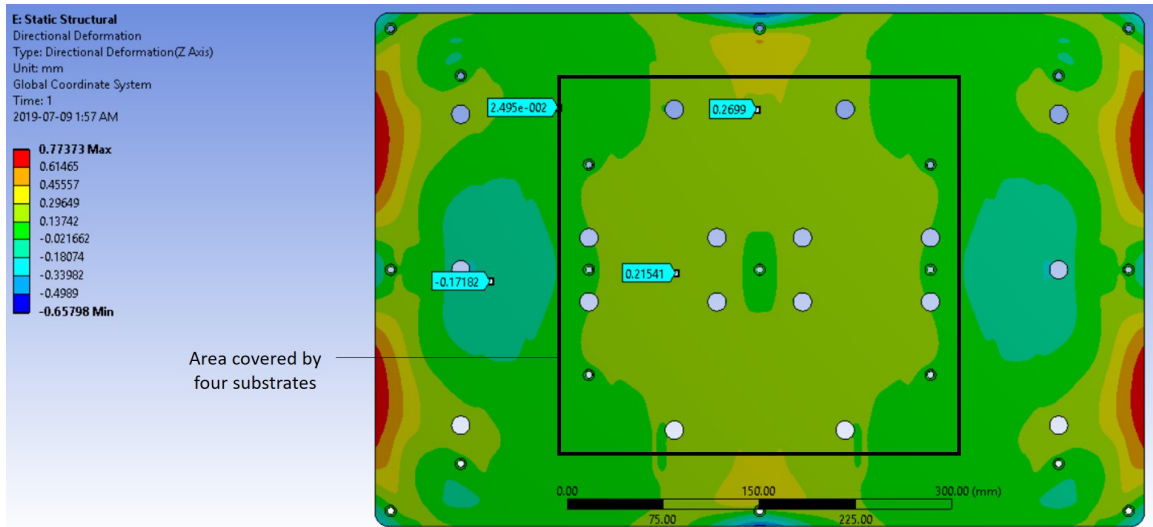


Figure 4.8 Simulated buckling due to thermal effects of the top assembly

- **suction chucks**

The design makes use of three suction holes, that are distributed in a shape that resembles a triangle, to securely hold a flat piece of substrate in place. The reason being that it takes three points to create a flat plane. Hence, each of the four substrates to be coated should at least be held down by the three suction holes.

A suction reservoir connects the suction hole to the suction pump to hold the substrates down. Figure 4.9 is a depiction of the inner workings of the suction system inside the stage. The O-ring grooves around the tube are designed with the rod and piston sealing guidelines in mind [48]. An O-ring size of -013 and cross section of 0.07 inch was chosen for the grooves on the tubes. Similarly, the O-ring groove for the contact between the substrate and the stage was designed with face sealing guidelines. An O-ring size of -017 and cross section of 0.07 inch was chosen for the groove where the substrate sits on. Since the stage potentially heats up to 300 °C, Kalrez O-rings would be ideally used as they can withstand up to 315 °C. However, because the depositions for initial testing will fall under 200 °C, high temperature silicone O-rings were used.

The first step is to define how much suction strength is necessary to firmly hold the

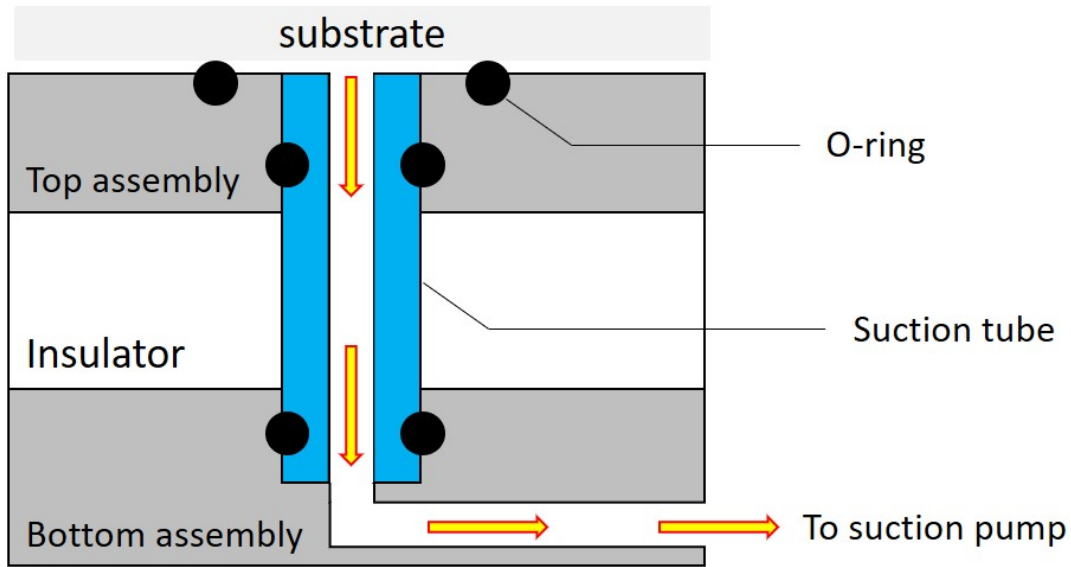


Figure 4.9 suction chuck concept to hold substrates

four substrates down. Since the substrates will be placed on top of the oscillating substrate stage, the suction needs to strongly pull the substrate to the stage surface to generate sufficient static friction in between the contacts to prevent sliding during the oscillation, as shown in Figure 4.10.

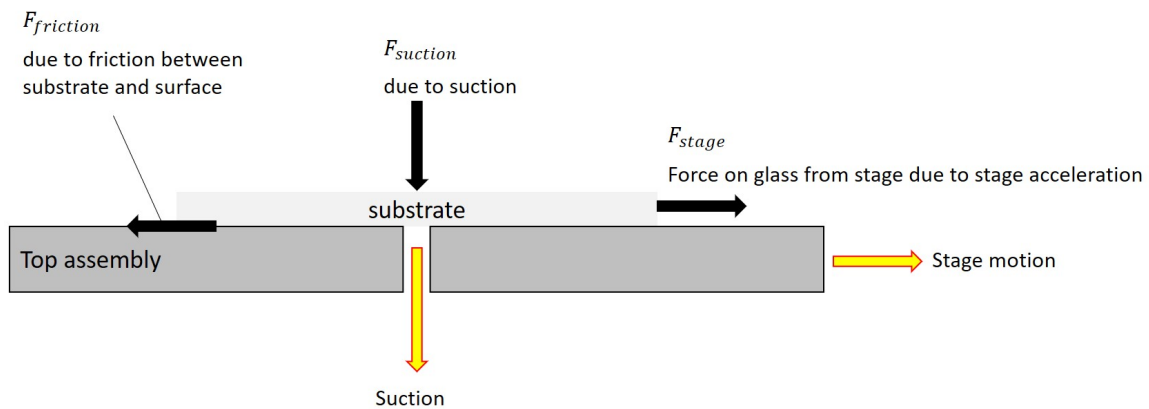


Figure 4.10 Free body diagram of the substrate during stage acceleration or deceleration

The oscillating distance is limited by the maximum stroke length of the linear stage, which is 0.6 m. The ideal oscillating frequency was determined to be 2 Hz to realize the high commercial-scale throughput. To prevent significant flow disruption during

the deposition process, the travel speed is kept as uniform as possible while the substrates are passing underneath the reactor. Hence, the linear stage motion profile follows the shape of a trapezoid where the left and right triangles represents the acceleration and deceleration zones as shown in Figure 4.11.

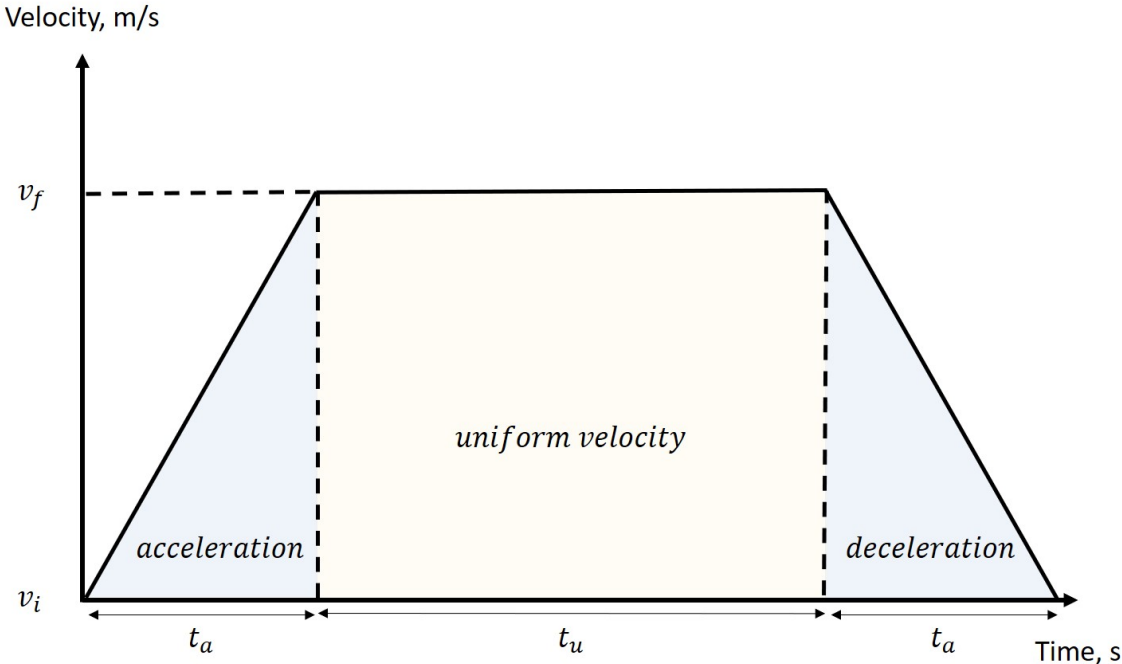


Figure 4.11 Motion profile of the stage

A uniform velocity region of 0.434 m, and maximum acceleration/deceleration distance of 0.083 m were previously defined (details can be found in Chee Hau Teoh’s MASc. thesis). To maximize the uniform velocity region, the total dwell time in the acceleration and deceleration regions should be kept as short as possible. We assigned a total accelerate and decelerate time of 0.1 s per oscillation, or 0.025 s to accelerate or decelerate each time. This leaves 0.8 s for uniform velocity for an oscillation frequency of 2 Hz, or 0.4 s per oscillation (0.2 s per stroke). Using the kinematics equation, the acceleration/deceleration of the substrate stage is:

$$\text{Uniform speed region, } v_f = \frac{0.434 \text{ m}}{0.2 \text{ s}} = 2.17 \text{ m/s} \quad (4.1)$$

$$\text{Acceleration or deceleration, } a_{stage} = \frac{v_f - v_i}{t} = \frac{(2.17 - 0) \text{ m/s}}{0.025 \text{ s}} = 86.8 \text{ m/s}^2 \quad (4.2)$$

Knowing the acceleration of the stage, the friction required to hold the substrate down can be calculated.

$$\text{Density of borosilicate, } \rho_{borosilicate} = 2225 \text{ kg/m}^3$$

$$\text{Coefficient of friction, } \mu_{borosilicate \text{ on metal}} = 0.5$$

$$\text{Dimensions of substrate, } 0.15 \times 0.15 \times 0.001 \text{ m}^3$$

$$\text{Total mass of four substrates, } 0.2 \text{ kg}$$

$$F_{stage} - F_{friction} = m_{substrate} a_{substrate} \quad (4.3)$$

Since the desired case is that the suction is strong enough to prevent any sliding motion of the substrate relative to the stage, $a_{substrate} = 0 \text{ m/s}^2$

$$F_{stage} = F_{friction} \quad (4.4)$$

$$F_{stage} = m_{substrate} a_{stage} = 0.2 \text{ kg} \times 86.8 \text{ m/s}^2 = 17.36 \text{ N} \quad (4.5)$$

$$F_{friction} = \mu_{borosilicate\ on\ metal} \times F_{suction} \quad (4.6)$$

$$F_{suction} = \frac{F_{stage}}{\mu_{borosilicate\ on\ metal}} = \frac{17.36}{0.5} = 34.72\ N \quad (4.7)$$

Hence, the force needed to hold all four substrates down is 34.72 N. With a diametral constraint of 10 mm per suction hole and a total of at least twelve holes to hold four substrates, the effective suction strength can be calculated.

$$\text{Total area of suction, } A_{suction} = 12 \times \pi \times \left(\frac{0.01\ m}{2}\right)^2 = 9.42 \times 10^{-4}\ m^2 \quad (4.8)$$

$$\text{Minimum suction pressure needed, } P_{suction} = \frac{F_{suction}}{A_{suction}} = 36.9\ kPA \quad (4.9)$$

Applying a safety factor of 2.5 [49], a suction of 92.25 kPA is required.

Pierson Workholding SmartVac 3, a Venturi style suction pump, which only requires 85-100 psi of compressed air at 0.8 CFM, was chosen for its compact size and its ability to generate 95 kPA of suction.

4.2.3 Design of 3D printed pilot-scale reactor

To verify the scalability of the AP-SALD technique, large-area deposition of thin film must be demonstrated. A deposition area of at least $150 \times 150 \text{ mm}^2$ is required because that is the area of a standard 6-inch silicon wafer used in the semiconductor and solar cell industries. Hence, a scaled up version of the lab-scale AP-SALD reactor head has to be designed and fabricated.

CFD and SLA 3D printing constraints were again used to guide the channel design, similar to the approach described in Chapter 3. To meet the ideal aforementioned deposition area, a channel length of at least 150 mm is needed. However, due to the limitation on the build volume ($145 \times 145 \times 185 \text{ mm}^3$) of the Formlabs Form 3 SLA printer, designing a reactor with channels of 150 mm and above in length that fits within the build volume is challenging, although possible. Hence, a channel length of 120 to 135 mm was used for initial testing.

A major technical challenge with the pilot-scale AP-SALD system is the difficulty in reliably controlling and maintaining the reactor-substrate gap spacing throughout the deposition. This is due to the large-scale format of the system which exacerbates any inaccuracy and imprecision in all mechanical features, dimensional and assembly variances. All the more, the number of components involved in the system - such as laser displacement sensors, linear actuators, and the linear stage, add complexity to the gap spacing control. As mentioned in Chapter 2 and Chapter 3, the gap spacing plays a critical role in ensuring that the deposition is in ALD regime by preventing precursors from cross-talking/mixing or reacting with the air in the environment [41].

A unique pilot-scale reactor which reduces the adverse effects associated with larger gap spacing was designed. The reactor was designed with the same 3D printing guidelines described in Chapter 3.2.2. Figure 4.12 shows the design and the 3D printed reactor.

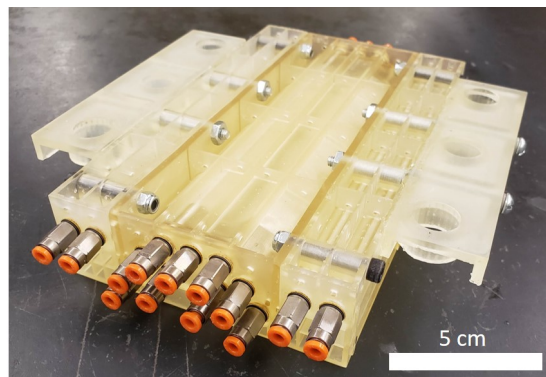
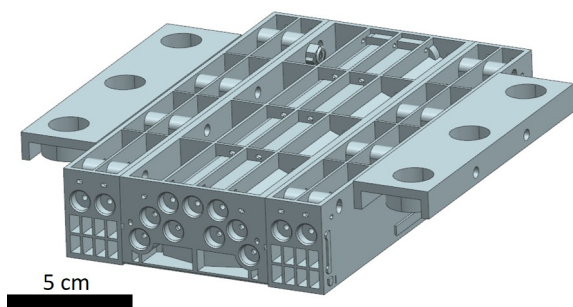


Figure 4.12 Design of the pilot-scale reactor and photo of the 3D printed reactor

4.3 Results and Discussion

4.3.1 Substrate stage testing

Two key tests of the substrate stage were performed, mainly the heating of the stage and the suction strength.

- **Stage heating test**

For initial testing, the stage was intended to be heated to 200 °C. It took a total of 12 minutes to heat the stage up from room temperature to 200 °C which is close to the target specified in Chapter 4.2.2. However, it was found that the temperature at the top surface of the stage is 20 °C lower than the temperature at the center core of the stage. The reason being that the thermocouple is installed to the core inside the stage to measure and provide feedback to the controller, this is also the location where most of the heat is concentrated at. The same test was carried out at 150 °C, and again the 20 °C temperature difference was observed. Hence, when setting the temperature of the stage, the user must keep in mind to include a 20 °C temperature offset to the set value to make sure the stage surface temperature reflects that of the intended temperature. To evaluate the temperature distribution of the surface where the substrates are placed. This was done to check if the areas covered by the substrate are relatively uniform to make sure the deposition rate stays consistent across the substrate. A temperature variation of less than 10 °C from the center of the stage to the edges of the substrate was observed.

- **Suction strength test**

The four 150 x 150 mm substrates were placed on the stage, where the suction holes are located, without any heating and oscillations for preliminary testing. The substrates

were forcefully pushed using hands, and they stayed firmly and securely affixed in position without any noticeable movements. The test was repeated, however this time with the stage heated to 200 °C and oscillated at 1.3 m/s for multiple cycles. Again, the four substrates firmly and securely stayed in position throughout the test. Hence, the estimated required suction strength was sufficient and that the suction design was shown to work effectively.

4.3.2 3D printed pilot-scale reactor testing

The reactor was used to produce zinc oxide and aluminum oxide films on 150 x 150 mm² borosilicate glass. Both depositions took approximately 5 minutes.

For the deposition of the zinc oxide film, nitrogen gas was bubbled through a diethylzinc precursor at 75 sccm and combined with a 425 sccm nitrogen carrier flow. Water was bubbled at 240 sccm and combined with a 1360 sccm nitrogen carrier flow. A 4800 sccm nitrogen curtain was used to partially separate the precursors and remove excess unreacted precursors or by-products. A reactor-substrate spacing of 250 µm was used. The substrate was heated to 120 °C and oscillated at a speed of 800 mm/s for 800 (101 mm) cycles. Figure 4.13 shows the zinc oxide film produced. The film thickness is 63 nm with uniformity variation of ±7% across the substrate, measured using reflectance spectroscopy. The measurement indicated a GPC of 0.08 nm/cycle (0.21 nm/s). The GPC is lower than that achieved by previously reported for zinc oxide (GPC of 0.18) [50, 51]. This can be caused by the high oscillation speed which shortens the time for surface reaction and saturation, leading to a decreased GPC [47]. Hence, more experiments are still required to optimize the oscillation speed for depositing zinc oxide.

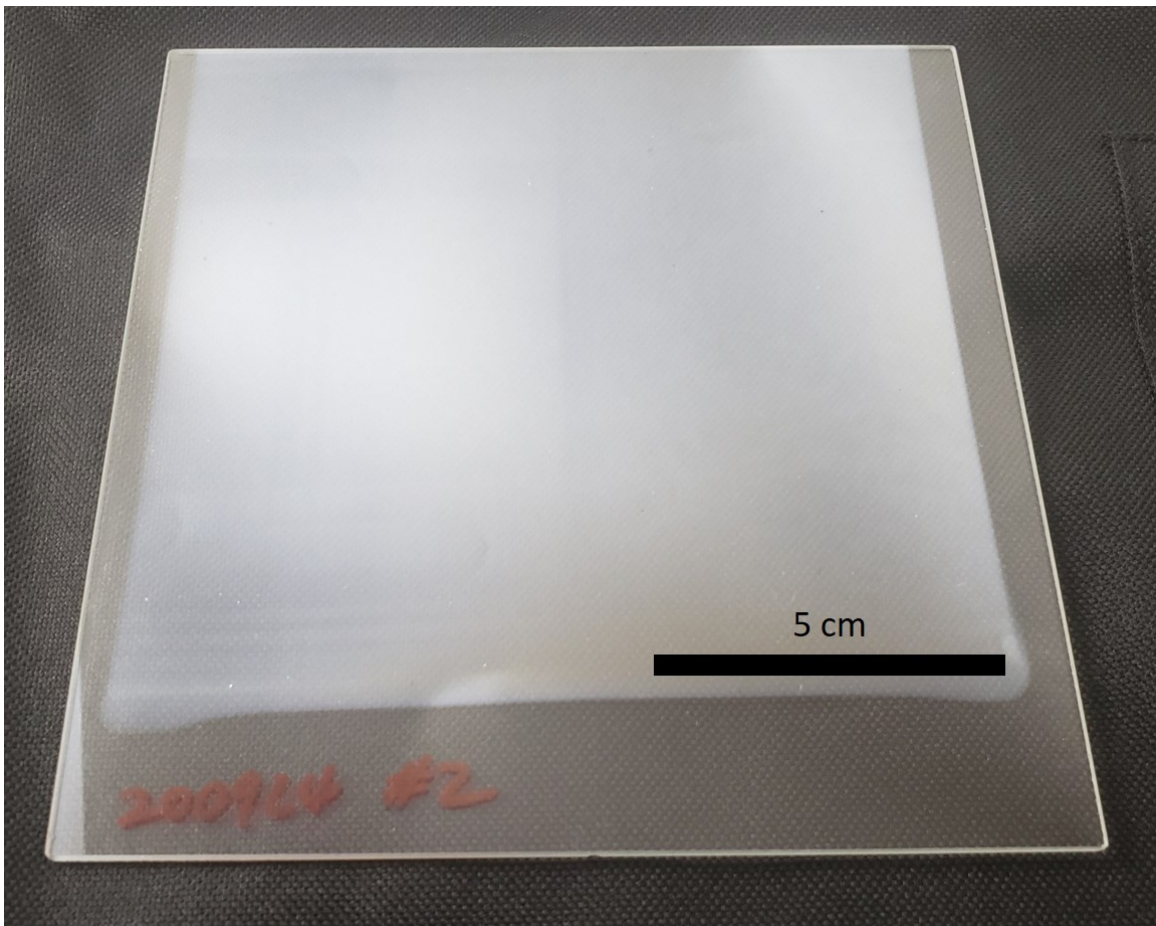


Figure 4.13 Zinc oxide film produced using the 3D printed pilot-scale reactor

For the deposition of the aluminum oxide film, nitrogen gas was bubbled through a trimethylaluminum precursor at 60 sccm and combined with a 340 sccm nitrogen carrier flow. Water was bubbled at 240 sccm and combined with a 1360 sccm nitrogen carrier flow. A 4800 sccm nitrogen curtain was used to partially separate the precursors and remove excess unreacted precursors or by-products. A reactor-substrate spacing of 250 μm was used. The substrate was heated to 150 $^{\circ}\text{C}$ and oscillated at a speed of 800 mm/s for 800 (123 mm) cycles. Figure 4.14 shows the aluminum oxide produced. The film thickness was measured using the Bruker dehtaXT, a stylus profilometry equipment. Five points distributed across the length of the substrate were chemically etched using sodium hydroxide to create a step for the profilometry measurement. The thicknesses was found

to be 108 nm with uniformity variation of $\pm 6\%$ across the substrate indicating a GPC of 0.135 nm/cycle (0.36 nm/s), consistent with that previously reported for aluminum oxide [52]. The film was measured using the Bruker dektakXT, a stylus profilometry machine.

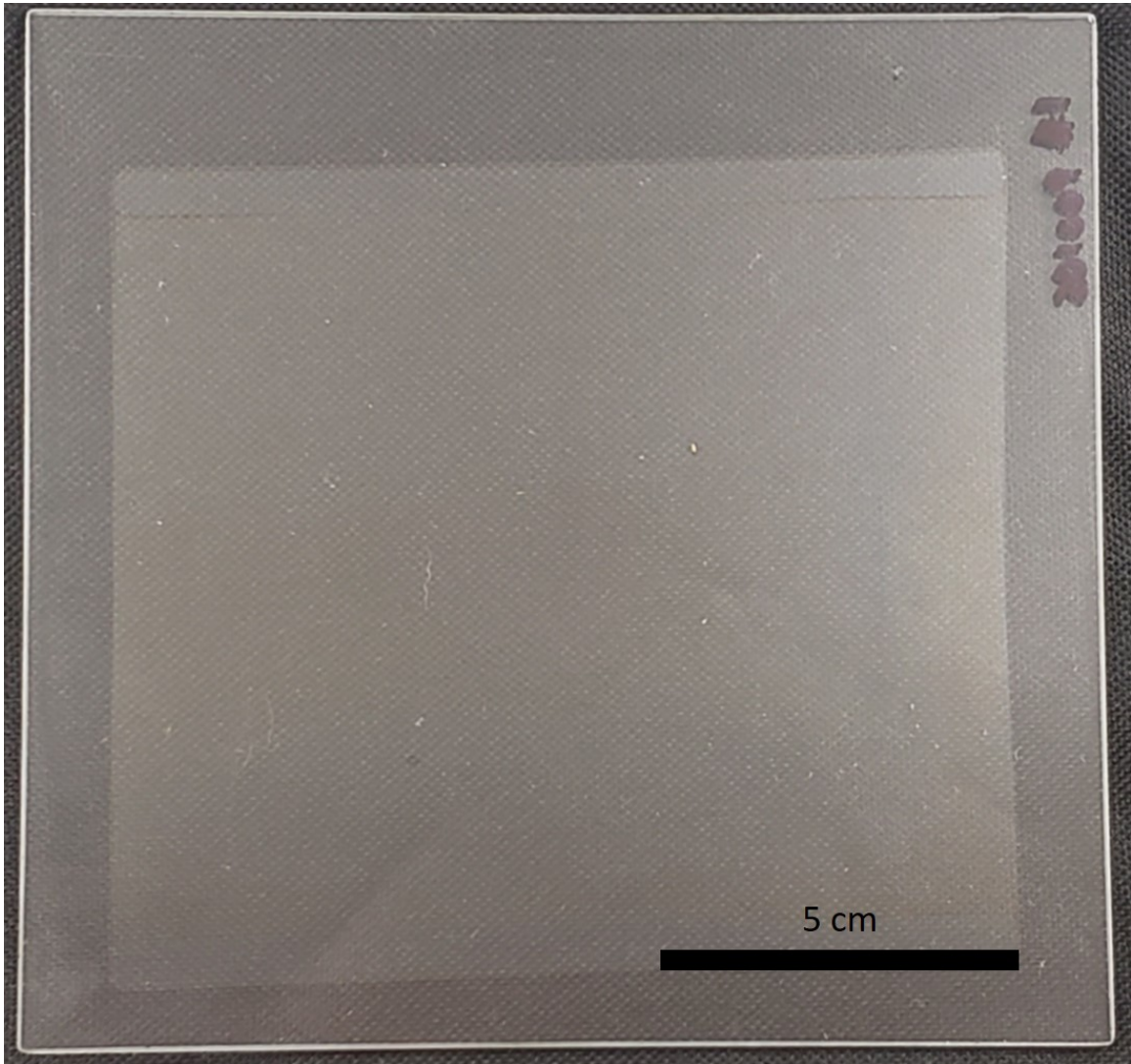


Figure 4.14 Aluminum oxide film produced using the 3D printed pilot-scale reactor

4.4 Conclusion

In conclusion, a pilot-scale heated stage that securely holds multiple substrates down while oscillating during deposition was designed and constructed. For initial experiments, the precursor materials being tested tend to have an ALD window within 200 °C, hence a heating element was appropriately sized for the initial experiments instead of the required specification (300 °C) listed in Chapter 4.2.1. The heating element was tested and has demonstrated efficacy in heating the stage up to and maintaining at the user defined temperature throughout the deposition.

The stage uses a suction chuck concept to hold the substrates down. The suction system was carefully designed. It includes the use of a Venturi style suction pump, a suction reservoir and some connecting tubes to pull the substrates down to the stage surface, generating high enough force to create sufficient sliding friction that prevents movement when the stage is oscillated. The design was tested by placing multiple substrates on the heated stage and oscillating it several times. The substrates were securely held in place with no noticeable movement observed during the oscillations indicating that the design works effectively.

A unique pilot-scale reactor head was designed, 3D printed and tested. A zinc oxide film with thickness of 63 nm (uniformity $\pm 10\%$) and aluminum oxide film with thickness of 108 nm (uniformity $\pm 7.5\%$) were deposited on large glass substrates.

Chapter 5

Conclusion and Future works

A custom lab-scale AP-SALD reactor head that can produce both uniform and gradient films was designed, and 3D printed. The design of the reactor head was in part guided by the feature size constraints of the fabrication method of choice – SLA 3D printing with the Formlabs Form machine. One such example is the minimum distance between two walls to prevent them from closing off during the 3D printing process. Apart from the SLA 3D printing design guidelines, CFD simulations played a big part in driving the considerations and decisions when designing the custom reactor head. For example, CFD was used in determining the ideal height of the channels to ensure that the flows are fully developed and have a relatively uniform flow profile (except for gradient channel) coming out from the channel outlets. Multiple channel geometries were conceptualized for which the predicted flow profile at the outlet were simulated. As a result, CFD was one of the most important aspects in guiding the design of the gradient channel. Due to the sophisticated inner network of channels inside the reactor head, SLA 3D printing is one of the best ways to rapidly produce a functional prototype at a low cost. The custom designed reactor was 3D printed and tested to produce both uniform and gradient zinc oxide films, during which the

gap spacing between the reactor and the substrate was uniform in both cases. This method of producing gradient films is contrary to another method that was developed in the lab where the reactor is tilted at an angle against the substrate, promoting a higher film growth rate (more AP-CVD than AP-SALD) at regions with higher gap spacing. Interestingly, the gradient film produced indicated a GPC variation across the substrate that is similar to the simulated results. Notably, the GPC on the side with a higher flow rate is twice that of the side with lower flow rates, consistent with the CFD results. However, more experiments should be conducted to corroborate this observation.

Separately, a pilot-scale heated stage that securely holds multiple substrates down while oscillating during deposition was designed and constructed. The heating element was tested and has demonstrated effectiveness in heating the stage up to and maintaining at the user defined temperature throughout the deposition. The stage also uses a vacuum design to hold the substrates down firmly and securely throughout the deposition. This is done by generating high enough force on the substrate to create sufficient sliding friction that prevents movement when the stage is oscillated. The design was tested by placing multiple substrates on the heated stage and oscillating several times. The test was successful such that the substrates were securely held in place with no noticeable movement observed during the oscillations indicating that the design works effectively. Furthermore, a unique pilot-scale reactor head was designed with the aim to reduce and potentially mitigate the adverse effects associated with larger gap spacing. This was necessary because the gap spacing is challenging to control and maintain due to the large-scale format of the system as well as the number of components involved, which are explained in greater detail in Chee Hau Teoh's MASc thesis. The reactor head was 3D printed and tested by successfully producing uniform zinc oxide (uniformity +/- 10%) and aluminum oxide (uniformity +/- 7.5%) films.

Future work for the lab-scale custom designed reactor includes 3D printing the lab-scale

custom designed reactor in metal for longevity, durability, and reusability (i.e. washable with strong acids/bases to remove the residual deposition in the reactor). With the 3D printed metal reactor, more experiments should be run to confirm the correlation between the GPC variation in the physical film produced and the velocity profile from the simulation (where a substrate is placed underneath the reactor).

Future work for the pilot-scale system revolves around improving the reactor head design. While already somewhat effective, the reactor can still be optimized to make it even less susceptible to the adverse effects associated with larger gap spacing such as the likelihood for metal precursor gas to still react with atmospheric air forming powder, as well as the potential crosstalk between precursor gases. Furthermore, a plasma source could be designed and integrated into the pilot-scale reactor, to enable plasma enhanced ALD at lower temperature (as low as 60 °C). This is an important next step because some substrates (e.g. polymer films) or underlying layers (e.g. metal halide perovskite) to be deposited on are sensitive to elevated temperatures. Another area to work on is to retrofit the system with roll-to-roll equipment (e.g. winders, unwinders, idlers, edge sensor, diametral sensor, etc) to test and validate the roll-to-roll compatibility of the technology for high throughput manufacturing processes. Finally, more effort is required in trying and developing recipes for more metal oxides (e.g. tin, titanium, tungsten, hafnium, zirconium oxides), pure metals (e.g. copper, palladium), nitrides, and sulphides for AP-SALD applications. This work will be important to validate the capability of the technology for making a wide range of functional thin films as a benchmark against other thin film deposition techniques, especially conventional ALD.

References

- [1] K. P. Musselman, C. F. Uzoma, M. S. Miller, Nanomanufacturing: high-throughput, cost-effective deposition of atomic scale thin films via atmospheric pressure spatial atomic layer deposition, *Chemistry of Materials* 28 (2016) 8443–8452.
- [2] T. L. Bergman, A. S. Lavine, F. P. Incropera, D. P. DeWitt, *Fundamentals of Heat and Mass Transfer*, 7 ed., Wiley, 2011.
- [3] S. M. George, Atomic layer deposition: an overview, *Chemical reviews* 110 (2010) 111–131.
- [4] R. W. Johnson, A. Hultqvist, S. F. Bent, A brief review of atomic layer deposition: from fundamentals to applications, *Materials Today* 17 (2014) 236–246.
- [5] H. Kim, H.-B.-R. Lee, W. J. Maeng, Applications of atomic layer deposition to nanofabrication and emerging nanodevices, *Thin Solid Films* 517 (2009) 2563–2580.
- [6] R. A. Ovanesyan, E. A. Filatova, S. D. Elliott, D. M. Hausmann, D. C. Smith, S. Agrawal, Atomic layer deposition of silicon-based dielectrics for semiconductor manufacturing: Current status and future outlooks, *Journal of Vacuum Science Technology* 37 (2019).
- [7] Y. S. Jung, A. S. Cavanagh, L. A. Riley, S.-H. Kang, A. C. Dillon, M. D. Groner, S. M. George, S.-H. Lee, Ultrathin direct atomic layer deposition on composite electrodes for highly durable and safe li-ion batteries, *Advanced Materials* 22 (2010) 2172–2176.
- [8] S. Moitzheim, B. Put, P. M. Vereecken, Advances in 3d thin-film li-ion batteries, *Advanced Materials Interfaces* 6 (2019).
- [9] Z. Chen, H. Wang, X. Wang, P. Chen, Y. Liu, H. Zhao, Y. Zhao, Y. Duan, Low-temperature remote plasma enhanced atomic layer deposition of zro₂/zirconia nanolaminate film for efficient

- encapsulation of flexible organic light-emitting diodes, *Scientific Reports* 7 (2017).
- [10] F. J. Ramos, T. Maindron, S. Béchu, A. Rebai, M. Frégnaux, M. Bouttemy, J. Rousset, P. Schulz, N. Scheider, Versatile perovskite solar cell encapsulation by low-temperature Al_2O_3 with long-term stability improvement, *Sustainable Energy Fuels* 2 (2018) 2468–2479.
- [11] R. J. Narayan, S. P. Adiga, M. J. Pellin, L. A. Curtiss, A. J. Hryn, S. Stafslie, B. Chisholm, C.-C. Shih, C.-M. Shih, S.-J. Lin, et al., Atomic layer deposition-based functionalization of materials for medical and environmental health applications, *Philosophical Transactions of the Royal Society A: Mathematical, Physical and Engineering Sciences* 368 (2010) 2033–2064.
- [12] D. Muñoz-Rojas, V. H. Nguyen, C. M. de la Huerta, S. Aghazadehchors, C. Jiménez, D. Bellet, Spatial atomic layer deposition (sald), an emerging tool for energy materials. application to new-generation photovoltaic devices and transparent conductive materials, *Comptes Rendus Physique* 18 (2017) 391–400.
- [13] A. H. Alshehri, K. Mistry, V. H. Nguyen, K. H. Ibrahim, D. Muñoz-Rojas, M. Yavuz, K. P. Musselman, Quantum-tunneling metal-insulator-metal diodes made by rapid atmospheric pressure chemical vapor deposition, *Advanced Functional Materials* 29 (2018) 1805533.
- [14] T. Kümmell, D. Andrzejewski, Y. Beckmann, M. Adelbaky, T. Yeow, A. Grundmann, M. Heuken, H. Kalisch, A. V. Vescan, K. P. Musselman, G. Bacher, WSe_2 monolayer based light emitting devices fabricated by scalable deposition techniques, *Proceedings of SPIE* 11302 (2020).
- [15] F. J. van den Bruele, M. Smets, A. Illiberi, Y. Creyghton, P. Buskens, F. Roozeboom, P. Poodt, Atmospheric pressure plasma enhanced spatial ald of silver, *Journal of Vacuum Science & Technology A: Vacuum, Surfaces, and Films* 33 (2015) 01A131.
- [16] T. W.-K. Yeow, K. Mistry, A. Shahin, M. Yavuz, K. P. Musselman, Atmospheric-pressure spatial chemical vapor deposition of tungsten oxide, *Journal of Vacuum Science & Technology A: Vacuum, Surfaces, and Films* 38 (2020) 052411.
- [17] R. L. Hoye, D. Muñoz-Rojas, S. F. Nelson, A. Illiberi, P. Poodt, F. Roozeboom, J. L. MacManus-Driscoll, Research update: Atmospheric pressure spatial atomic layer deposition of zno thin films: Reactors, doping, and devices, *APL materials* 3 (2015) 040701.

- [18] A. H. Brozena, C. J. Oldham, G. N. Parsons, Atomic layer deposition on polymer fibers and fabrics for multifunctional and electronic textiles, *Journal of Vacuum Science & Technology A: Vacuum, Surfaces, and Films* 34 (2016) 010801.
- [19] R. Potyrailo, K. Rajan, K. Stoewe, I. Takeuchi, B. Chisholm, H. Lam, Combinatorial and high-throughput screening of materials libraries: review of state of the art, *ACS combinatorial science* 13 (2011) 579–633.
- [20] A. M. Saranya, A. Morata, D. Pla, M. Burriel, F. Chiabrera, I. Garbayo, A. Hornes, J. A. Kilner, A. Tarancon, Unveiling the outstanding oxygen mass transport properties of mn-rich perovskites in grain boundary-dominated $\text{La}_{0.8}\text{Sr}_{0.2}(\text{Mn}_{1-x}\text{Co}_x)\text{O}_{3\pm\delta}$ nanostructures, *Chemistry of Materials* 30 (2018) 5621–5629.
- [21] M. Pavan, S. Rühle, A. Ginsburg, D. A. Keller, H.-N. Barad, P. M. Sberna, D. Nunes, R. Martins, A. Y. Anderson, A. Zaban, et al., $\text{TiO}_2/\text{Cu}_2\text{O}$ all-oxide heterojunction solar cells produced by spray pyrolysis, *Solar Energy Materials and Solar Cells* 132 (2015) 549–556.
- [22] S. Klinkhammer, X. Liu, K. Huska, Y. Shen, S. Vanderheiden, S. Valouch, C. Vannahme, S. Bräse, T. Mappes, U. Lemmer, Continuously tunable solution-processed organic semiconductor dfb lasers pumped by laser diode, *Optics express* 20 (2012) 6357–6364.
- [23] C. M. Stafford, K. E. Roskov, T. H. Epps III, M. J. Fasolka, Generating thickness gradients of thin polymer films via flow coating, *Review of scientific instruments* 77 (2006) 023908.
- [24] A. Kafizas, G. Hyett, I. P. Parkin, Combinatorial atmospheric pressure chemical vapour deposition (capcvd) of a mixed vanadium oxide and vanadium oxynitride thin film, *Journal of Materials Chemistry* 19 (2009) 1399–1408.
- [25] S. Guerin, B. E. Hayden, Physical vapor deposition method for the high-throughput synthesis of solid-state material libraries, *Journal of Combinatorial Chemistry* 8 (2006) 66–73.
- [26] M. Reinke, Y. Kuzminykh, P. Hoffmann, Low temperature chemical vapor deposition using atomic layer deposition chemistry, *Chemistry of Materials* 27 (2015) 1604–1611.
- [27] M. A. Wei Lei, Laurent Henn-Lecordier, G. W. Rubloff, Real-time observation and optimization of tungsten atomic layer deposition process cycle, *Journal of Vacuum Science Technology B* 24 (2006) 780–789.

- [28] H. Salami, A. Poissant, R. A. Adomaitis, Anomalously high alumina atomic layer deposition growth per cycle during trimethylaluminum under-dosing conditions, *Journal of Vacuum Science Technology A* 35 (2006).
- [29] Y. W. Lai, M. Krause, A. Savan, S. Thienhaus, N. Koukourakis, M. R. Hofmann, A. Ludwig, High-throughput characterization of film thickness in thin film materials libraries by digital holographic microscopy, *Science and technology of advanced materials* (2011).
- [30] H. Oguchi, J. Hattrick-Simpers, I. Takeuchi, E. Heilweil, L. Bendersky, An infrared imaging method for high-throughput combinatorial investigation of hydrogenation-dehydrogenation and new phase formation of thin films, *Review of Scientific Instruments* 80 (2009) 073707.
- [31] R. L. Davis, S. Jayaraman, P. M. Chaikin, R. A. Register, Creating controlled thickness gradients in polymer thin films via flowcoating, *Langmuir* 30 (2014) 5637–5644.
- [32] J.-R. Chen, Alternative routes to atomic layer deposition: Reactor design and process development (2017).
- [33] G. Gakis, H. Vergnes, E. Scheid, C. Vahlas, B. Caussat, A. G. Boudouvis, Computational fluid dynamics simulation of the ald of alumina from tma and h₂o in a commercial reactor, *Chemical Engineering Research and Design* 132 (2018) 795–811.
- [34] G. P. Gakis, H. Vergnes, E. Scheid, C. Vahlas, A. G. Boudouvis, B. Caussat, Detailed investigation of the surface mechanisms and their interplay with transport phenomena in alumina atomic layer deposition from tma and water, *Chemical Engineering Science* 195 (2019) 399–412.
- [35] M. R. Shaeri, T.-C. Jen, C. Y. Yuan, Reactor scale simulation of an atomic layer deposition process, *Chemical Engineering Research and Design* 94 (2015) 584–593.
- [36] Y. Zhang, Y. Ding, P. D. Christofides, Multiscale computational fluid dynamics modeling of thermal atomic layer deposition with application to chamber design, *Chemical Engineering Research and Design* 147 (2019) 529–544.
- [37] D. Pan, Numerical and experimental studies of atomic layer deposition for sustainability improvement (2016).
- [38] Y. Zhang, Y. Ding, Z. Wu, P. D. Christofides, Run-to-run control of thermal atomic layer

- deposition, in: 2020 28th Mediterranean Conference on Control and Automation (MED), IEEE, 2020, pp. 1080–1086.
- [39] M. M. Mousa, et al., High throughput atomic layer deposition processes: High pressure operations, new reactor designs, and novel metal processing. (2015).
- [40] A. Yersak, Roll-to-roll atomic layer deposition of ultrabarriers, PhD (2016).
- [41] C. Masse de la Huerta, V. H. Nguyen, J.-M. Dedulle, D. Bellet, C. Jiménez, D. Muñoz-Rojas, Influence of the geometric parameters on the deposition mode in spatial atomic layer deposition: A novel approach to area-selective deposition, *Coatings* 9 (2019) 5.
- [42] G. Ramirez Troxler, Wafer transport and gas separation in a contact-less spatial atomic layer deposition track (2011).
- [43] A. Thakur, J. Sundqvist, M. Krug, R. Weidl, Superfast plasma ald with 3d-printed ceramic rocket nozzles (2019).
- [44] F. Zoubian, H. Rabat, O. Aubry, N. Dumuis, S. Dozias, D. Muñozrojas, D. Hong, Development and characterization of an atmospheric pressure plasma reactor compatible with spatial ald, in: *Journal of Physics: Conference Series*, volume 1243, IOP Publishing, 2019, p. 012002.
- [45] V. H. Nguyen, A. Sekkat, C. A. Masse de la Huerta, F. Zoubian, C. Crivello, J. Rubio-Zuazo, M. Jaffal, M. Bonvalot, C. Vallee, O. Aubry, et al., Atmospheric plasma-enhanced spatial chemical vapor deposition of sio₂ using trivinylmethoxysilane and oxygen plasma, *Chemistry of Materials* (2020).
- [46] C. A. M. de la Huerta, V. H. Nguyen, A. Sekkat, C. Crivello, F. Toldra-Reig, P. Veiga, C. Jimenez, S. Quessada, D. Muñoz-Rojas, Facile patterning of functional materials via gas-phase 3d printing, *arXiv preprint arXiv:2006.05235* (2020).
- [47] K. Mistry, A. Jones, M. Kao, T. W.-K. Yeow, M. Yavuz, K. P. Musselman, In-situ observation of nucleation and property evolution in films grown with an atmospheric pressure spatial atomic layer deposition system., *Nano Express* (2020).
- [48] Parker o-ring handbook ord 5700, 2018.
- [49] K. Korane, How do you size a vacuum cup?, 2016.

- [50] A. Illiberi, F. Roozeboom, P. Poodt, Spatial atomic layer deposition of zinc oxide thin films, *ACS applied materials & interfaces* 4 (2012) 268–272.
- [51] E. Guziewicz, M. Godlewski, T. Krajewski, Ł. Wachnicki, A. Szczepanik, K. Kopalko, A. Wójcik-Głódowska, E. Przeździecka, W. Paszkowicz, E. Łusakowska, et al., ZnO grown by atomic layer deposition: A material for transparent electronics and organic heterojunctions, *Journal of Applied Physics* 105 (2009) 122413.
- [52] D. Munoz-Rojas, J. MacManus-Driscoll, Spatial atmospheric atomic layer deposition: a new laboratory and industrial tool for low-cost photovoltaics, *Materials Horizons* 1 (2014) 314–320.

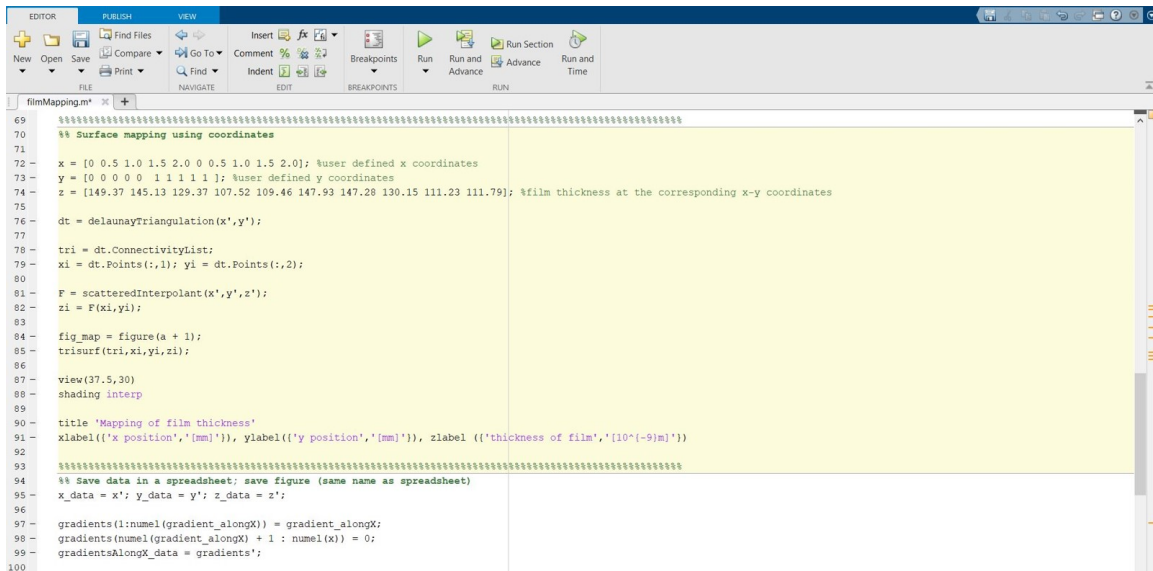
APPENDICES

Appendix A

Thickness gradient film with a lab-scale AP-SALD reactor

A.1 Film mapping code

Figure A.1 is a portion of the film mapping code developed in MATLAB showing the application of Delaunay triangulation, how data points are interpolated and meshed for creating a mapped profile of the film thicknesses (measurement is taken at user defined coordinates on the film).



```
69 %%%%%%%%%%%%%%%%%%%%%%%%%%%%%%%%%%%%%%%%%%%%%%%%%%%%%%%%%%%%%%%%%%%%%%%%%%%
70 %% Surface mapping using coordinates
71
72 x = [0 0.5 1.0 1.5 2.0 0 0.5 1.0 1.5 2.0]; %user defined x coordinates
73 y = [0 0 0 0 1 1 1 1 1]; %user defined y coordinates
74 z = [149.37 145.13 129.37 107.52 109.46 147.93 147.28 130.15 111.23 111.79]; %film thickness at the corresponding x-y coordinates
75
76 dt = delaunayTriangulation(x',y');
77
78 tri = dt.ConnectivityList;
79 xi = dt.Points(:,1); yi = dt.Points(:,2);
80
81 F = scatteredInterpolant(x',y',z');
82 zi = F(xi,yi);
83
84 fig_map = figure(a + 1);
85 trisurf(tri,xi,yi,zi);
86
87 view(37.5,30)
88 shading interp
89
90 title 'Mapping of film thickness'
91 xlabel(['x position','[mm]']), ylabel(['y position','[mm]']), zlabel(['thickness of film','[10^-9]m'])
92
93 %%%%%%%%%%%%%%%%%%%%%%%%%%%%%%%%%%%%%%%%%%%%%%%%%%%%%%%%%%%%%%%%%%%%%%%%%%%
94 %% Save data in a spreadsheet; save figure (same name as spreadsheet)
95 x_data = x'; y_data = y'; z_data = z';
96
97 gradients(1:numel(gradients_alongX)) = gradient_alongX;
98 gradients(numel(gradients_alongX) + 1 : numel(x)) = 0;
99 gradientsAlongX_data = gradients';
100
```

Figure A.1 Film mapping code using the Delaunay triangulation method of interpolation

Appendix B

Scale-up of a heated substrate stage for pilot-scale AP-SALD system

B.1 Heating Power Budgeting Tool

This section is a collection of the snapshots of the Heating Power Budgeting Tool developed on Microsoft Excel. Yellow highlighted fields are user defined input, whereas orange highlighted ones are the output values

All of the formulae in the Excel worksheet are adapted from or derived based on the formulae found in the book Fundamentals of Heat and Mass Transfer [2].

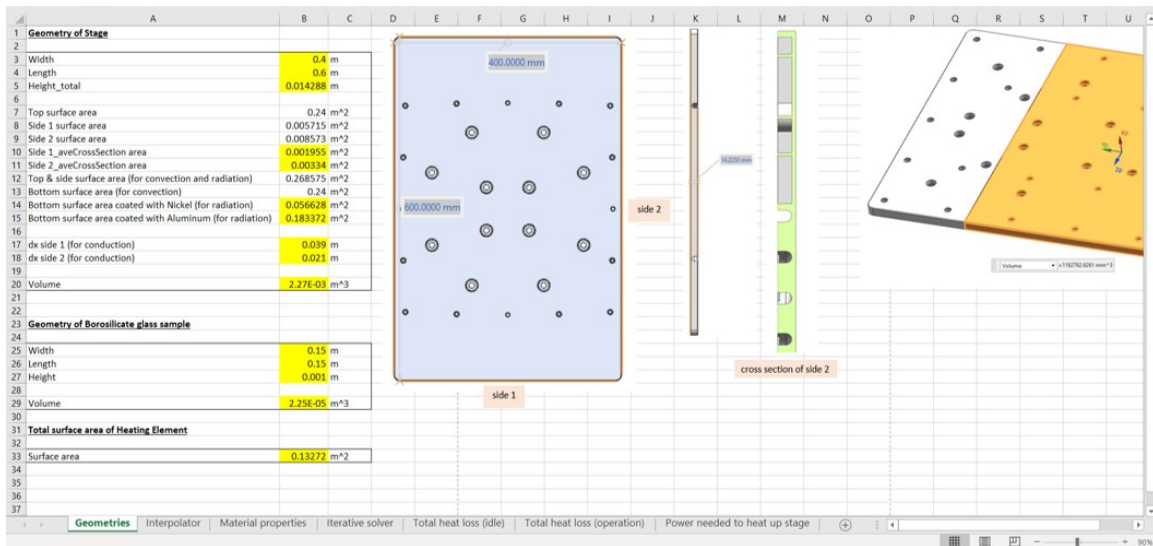


Figure B.1 Sheet 1: Geometry definition of the stage top assembly

Thermophysical properties of solids							
	rho (kg/m ³)	cp (J/kg.K)	k (W/m.K)	alpha (m ² /s)	emissivity of Nickel (at 573K)	emissivity of Aluminum (at 573K)	
Aluminum	2702	903	140	0.000971		0.38	0.058
Copper	8933	385	401	0.0000117		0.4	
Borosilicate glass	2225	835	1.4				

Thermophysical properties of gases at atmospheric pressure							
	rho (kg/m ³)	cp (J/kg.K)	mu (N.s/m ²)	nu (m ² /s)	k (W/m.K)	alpha (m ² /s)	Pr
air (at 434K)	0.805072	1.01876	2.44E-05	3.05E-05		0.03618	4.44E-05 0.68728

Figure B.2 Sheet 2: Material Properties of the stage top assembly

Interpolation										TABLE A.4 Thermophysical Properties of Gases at Atmospheric Pressure*									
air	T	rho	cp	mu	nu	k	a	Pr		T	rho	cp	mu	nu	k	a	Pr		
Set 1	400	0.87	1.014	2.30E-05	2.64E-05	0.0338	3.83E-05	0.69		(K)	(kg/m ³)	(kJ/kg·K)	(N·s/m ²)	(m ² /s)	(W/m·K)	(m ² /s)			
Set 2	450	0.77	1.021	2.51E-05	3.24E-05	0.0373	4.72E-05	0.69		Air, $\theta = 28.97$ kg/kmol									
Interpolated	434	0.81	1.01876	2.44E-05	3.05E-05	0.03618	4.44E-05	0.69		100	3.552	1.032	71.1	2.00	9.34	2.54	0.786		
air	T	rho	cp	mu	nu	k	a	Pr		150	2.364	1.012	103.4	4.426	13.8	5.84	0.758		
Set 1	550	0.63	1.04	2.88E-05	4.56E-05	4.39E-02	6.67E-05	0.68		200	1.7488	1.007	132.5	7.500	18.1	10.3	0.737		
Set 2	600	0.58	1.051	3.06E-05	5.27E-06	4.69E-02	7.69E-05	0.69		250	1.3947	1.006	159.6	11.44	22.3	15.9	0.720		
Interpolated	570	0.61	1.0444	2.95E-05	2.94E-05	0.0451	7.08E-05	0.68		300	1.1614	1.007	184.6	15.89	26.3	22.5	0.707		
										350	0.9950	1.009	208.2	20.82	30.0	29.9	0.700		
										400	0.8711	1.014	230.1	26.41	33.8	38.3	0.690		
										450	0.7740	1.021	250.7	32.39	37.3	47.2	0.686		
										500	0.6964	1.030	270.1	38.79	40.7	56.7	0.684		
										550	0.6329	1.040	288.4	45.57	43.9	66.7	0.683		
										600	0.5804	1.051	305.8	52.69	46.9	76.9	0.685		
										650	0.5356	1.063	322.5	60.21	49.7	87.3	0.690		
										700	0.4975	1.075	338.8	68.10	52.4	98.0	0.695		
										750	0.4643	1.087	354.6	76.37	54.9	109	0.702		
										800	0.4354	1.099	369.8	84.93	57.3	120	0.709		
										850	0.4097	1.110	384.3	93.80	59.6	131	0.716		
										900	0.3868	1.121	398.1	102.9	62.0	143	0.720		
										950	0.3666	1.131	411.3	112.2	64.3	155	0.725		
										1000	0.3482	1.141	424.4	121.9	66.7	168	0.726		
										1100	0.3166	1.159	449.0	141.8	71.5	195	0.728		

Figure B.3 Sheet 3: Interpolator to determine the thermophysical properties at a user defined temperature based on established data set [2]

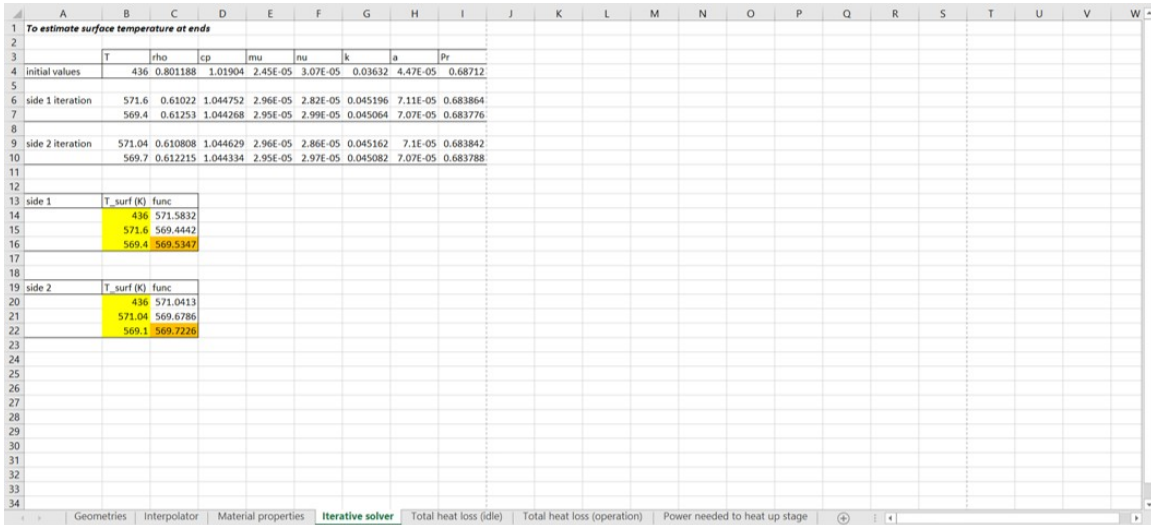


Figure B.4 Sheet 4: Iterative solver to estimate the side temperatures of the stage

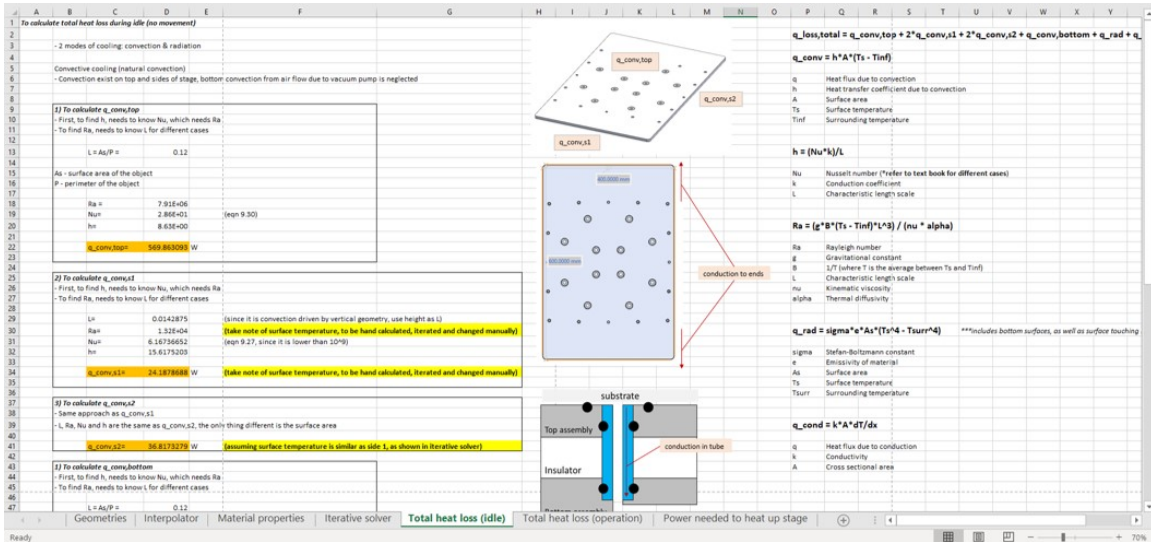


Figure B.5 Sheet 5a: Calculation of the total heat loss from the stage top assembly to bottom assembly and environment during idle

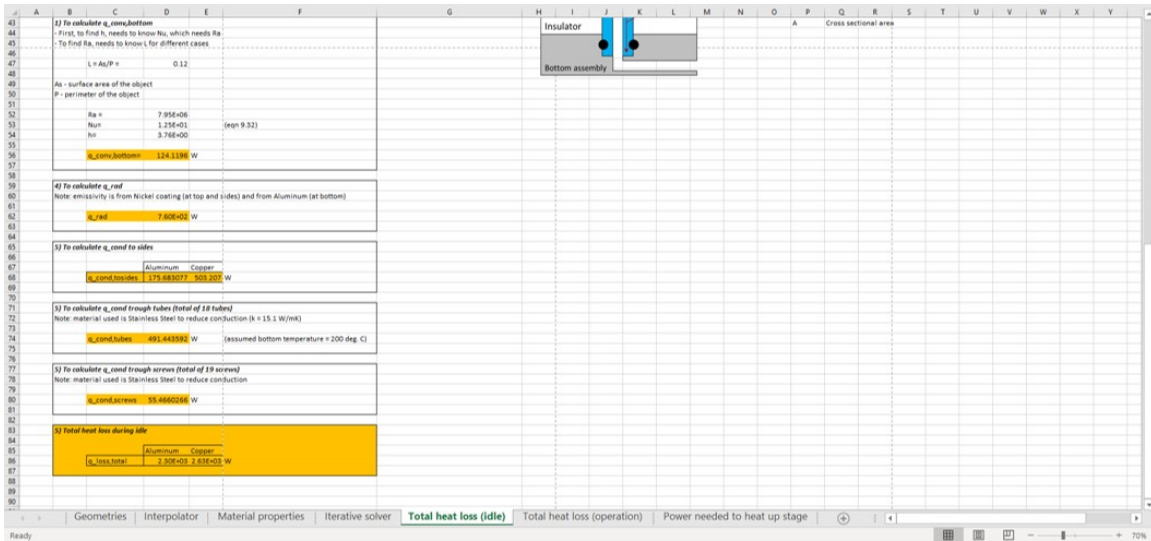


Figure B.6 Sheet 5b: Continuation of Sheet 5a

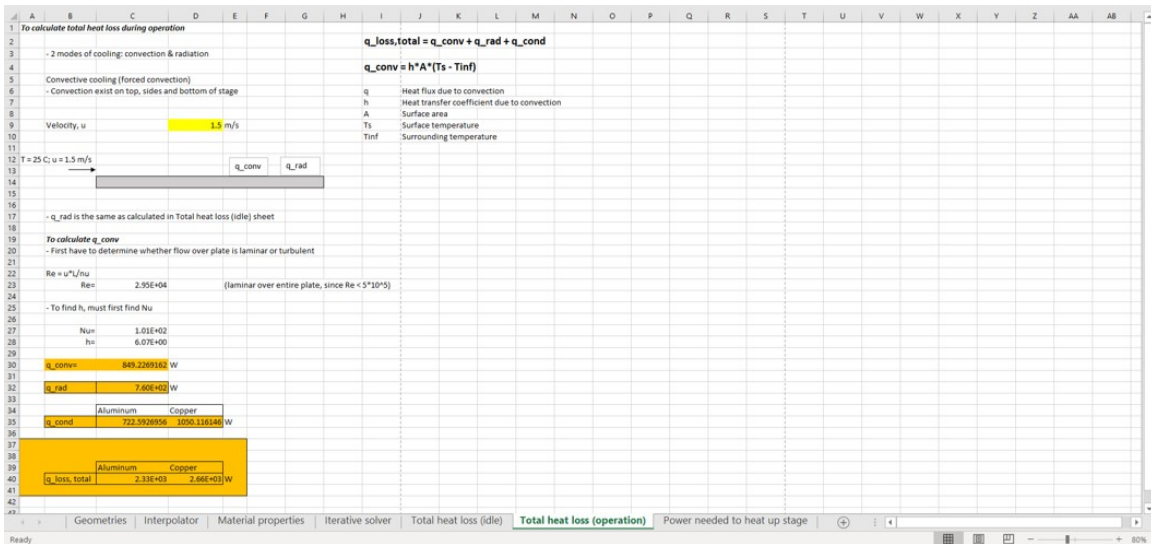


Figure B.7 Sheet 6: Calculation of the total heat loss from the stage top assembly when it is oscillating

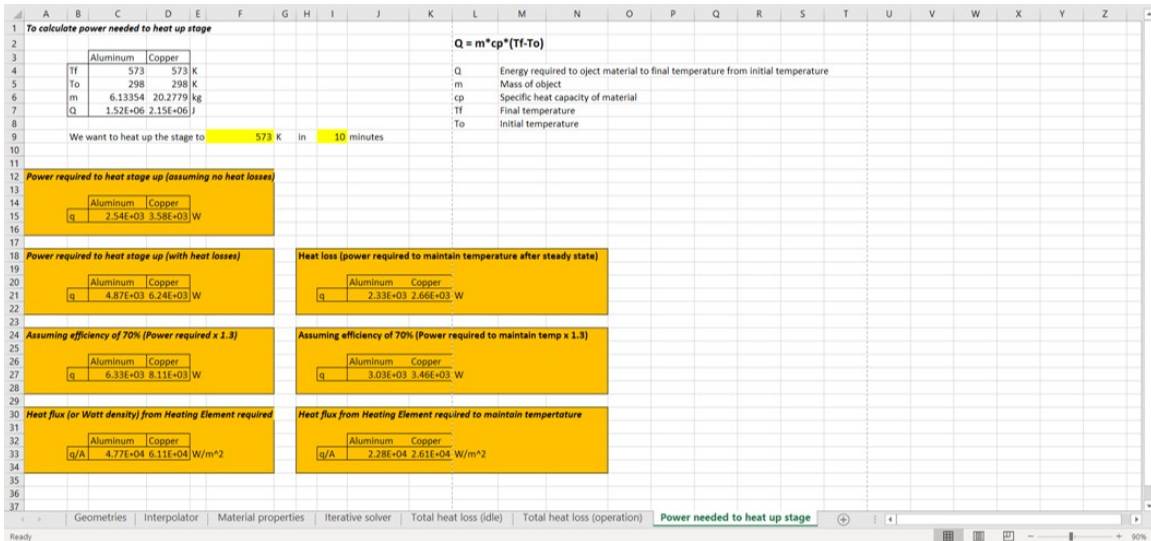


Figure B.8 Sheet 7: Calculation of the total heating power needed to heat stage to and maintain at user defined temperature during idle and operation

B.2 Iterative Solver

The iterative solver is used to estimate the temperature at the sides of the stage top assembly. This calculation is mainly to capture the conduction heat loss from the side ends of the heating element to the sides of the top assembly, as well as the natural convection at the sides of the top assembly during idle. Forced convection is not considered, as it is calculated in a separate sheet named "Total Heat Loss (Operation)". The heating element is heated to 300 °C (or 573 K) in this analysis, and the freestream atmospheric temperature is 25 °C (or 298 K). All of the formulae herein are adapted from or derived based on the formulae found in the book Fundamentals of Heat and Mass Transfer [2].

The assumptions made for this solver are as follows:

- radiation effects are ignored
- top and bottom convection effects are ignored for this analysis

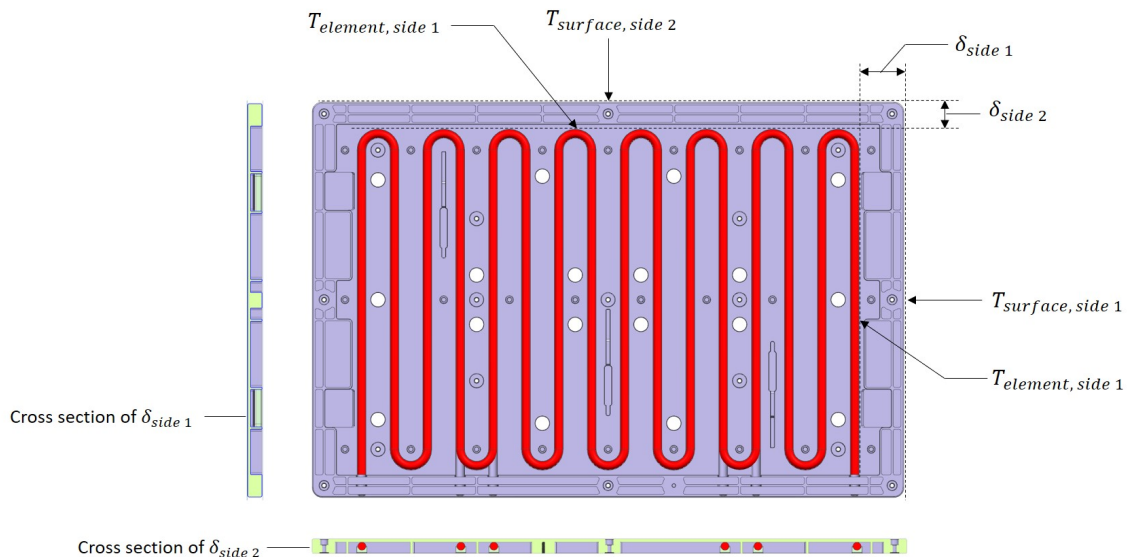


Figure B.9 Cross sections of the top assembly sides as well as heating element and side temperatures

Energy balance equation is used to calculate surface temperature at the sides.

$$\dot{E}_{in, side} = \dot{E}_{out, side} \quad (\text{B.1})$$

$$\dot{E}_{in} = q_{conduction} = k_{aluminum} A_{conduction} \frac{dT}{dx} \quad (\text{B.2})$$

$$\dot{E}_{out} = q_{convection} = h A_{sides} (T_{surface} - T_{\infty}) \quad (\text{B.3})$$

Equating equation A.2 and A.3:

$$k_{aluminum} A_{conduction} \frac{dT}{dx} = h A_{sides} (T_{surface} - T_{\infty}) \quad (\text{B.4})$$

At side 1

$$\delta_{side1} = 0.039 \text{ m}$$

$$A_{conduction} = 0.0019546 \text{ m}^2$$

$$A_{convection} = 0.005715 \text{ m}^2$$

NOTE: The material properties of aluminum and thermophysical properties of air can be found in the "Material properties" sheet.

Substituting the values into Equation A.4

$$140 \times 0.0019546 \times \frac{573 - T_{surface,side1}}{0.039} = h \times 0.005715 \times (T_{surface,side1} - 298) \quad (\text{B.5})$$

To find the convection heat transfer coefficient, h:

$$h = \frac{Nu \times k_{air}}{L} \quad (B.6)$$

$$Nu = 0.68 + \frac{0.670Ra_L^{\frac{1}{4}}}{[1 + [\frac{0.492}{Pr}]^{\frac{9}{16}}]^{\frac{4}{9}}} \quad (B.7)$$

$$Ra_L = \frac{(g \frac{2}{T_{surface,side1} + 298})(T_{surface,side1} - 298)L^3}{\nu\alpha} \quad (B.8)$$

Combining Equation A.5, A.6, A.7:

$$17.54 (573 - T_{surface,side1}) = 0.68 + \frac{0.670Ra_L^{\frac{1}{4}}}{[1 + [\frac{0.492}{Pr}]^{\frac{9}{16}}]^{\frac{4}{9}}} k_{air} (T_{surface,side1} - 298) \quad (B.9)$$

Where Ra_L is given by Equation A.8.

Since the $T_{surface,side1}$ appears on both left and right hand side of Equation A.9, the equation is solved iteratively to determine a converging value of $T_{surface,side1}$.

At side 2

$$\delta_{side2} = 0.021 \text{ m}$$

$$A_{conduction} = 0.0033396 \text{ m}^2$$

$$A_{convection} = 0.0085725 \text{ m}^2$$

Equation A.9 then becomes:

$$37.1 (573 - T_{surface,side2}) = 0.68 + \frac{0.670 Ra_L^{\frac{1}{4}}}{[1 + [\frac{0.492}{Pr}]^{\frac{9}{16}}]^{\frac{4}{9}}} k_{air} (T_{surface,side2} - 298) \quad (\text{B.10})$$